MONASH University

Understanding the Warm Water Volume Precursor of ENSO events

Sonja Neske

Supervisor: Dr Shayne McGregor
Co-supervisor: Dr Dietmar Dommenget

A thesis submitted for the degree of
Doctor of Philosophy
at Monash University in September 2019

School of Earth, Atmosphere and Environment
Faculty of Science
Melbourne, Australia

Copyright notice

Abstract

The El Niño- Southern oscillation (ENSO) is the largest climate variability on interannual time scales on our planet. Its near-global climatic impacts can lead to dramatic socioeconomic consequences. Thus, this thesis aims to enhance our understanding of details of ENSO dynamics and its predictability, both of which remain a major challenge for scientists today. In particular, this thesis examines the equatorial Pacific warm water volume (WWV, the anomalous thermocline depth integrated over the region 120-280°E and 5°N-5°S), a variable shown to precede ENSO sea surface temperatures (SSTs) by 1-3 seasons, and as such, is thought to be important for understanding ENSO predictability and dynamics.

We first use linear shallow water model simulations to decompose WWV changes between 1980-2016 into two components: the (i) adjusted wind response, which is consistent with the ENSO phase change driver of traditional ENSO theories; and (ii) instantaneous wind response, which are the instantaneous WWV changes due to Ekman transports dominated by wind-forced Kelvin waves. While the adjusted contribution dominates the WWV changes during the pre-2000 period, the instantaneous contribution dominates the WWV changes during the post-2000 period. This change in the relative importance of WWV drivers is shown to explain the shortening of the WWV/ENSO SST lead time from 2-3 seasons during the pre-2000 period to only 1 season during the post-2000 period. This leaves us with a post-2000 view of ENSO being driven by sudden wind bursts, rather than a self-sustained oscillation driven by the adjusted response as suggested by traditional ENSO theories.

Second, we reconcile the contrasting post-2000 44% decline of the adjusted WWV and 15% increase of instantaneous WVV. These contrasting WWV responses demonstrate that the generalization of strong anomalous equatorial Pacific wind stress leading to strong adjusted WWV responses cannot be correct. Thus, we categorize the oceanic adjusted responses to strong anomalous equatorial winds into three categories to better understand why and how often the above generalization is not

correct. During the entire 1980-2016 period only 35% of strong anomalous equatorial winds are consistent with this generalization, while the remaining are followed by neutral (56%) or persistent (9%) adjusted responses. The prominent neutral adjusted WWV response is shown to be largely excited by strong equatorial anomalous wind stress forcing with a weak curl and weaker Rossby wave projection than the generalized response.

Finally, we seek to compliment the Chapter 3 analysis by building a regression model of the adjusted WWV from the wind stress curl (an approximation for the Rossby wave signal) in different boxes around the equatorial Pacific. We identify, that 25% of the post-2000 adjusted WWV decline can be contributed to a decline of the STDs of the curls. The remaining 25% and 50% are attributed to changes in frequency and Rossby wave cancellations across the different regions respectively. Hereby, the dominant longitudinal region explaining these changes is found between 200-240°E which is east of the region of strongest winds. This region has shown to only produce WWV during eastern Pacific (EP) ENSO SSTs, thus the decline in adjusted WWV is consistent with the post-2000 declined occurrence of EP ENSO events.

Declaration

I hereby declare that this thesis contains no material which has been accepted for the award of any other degree or diploma at any university or equivalent institution and that, to the best of my knowledge and belief, this thesis contains no material previously published or written by another person, except where due reference is made in the text of the thesis.

This thesis includes 1 original paper published in peer reviewed journals. The core theme of the thesis is the understanding of the warm water volume precursor of El Niño- Southern Oscillation events. The ideas, development and writing up of all the papers in the thesis were the principal responsibility of myself, the student, working within the School of Earth, Atmosphere and Environment under the supervision of Dr Shayne McGregor. In the case of Chapter 2 my contribution to the work involved the following:

Thesis Chapter	Publication Title	Status *(published, in press, accepted or returned for revision)*	Nature and % of student contribution	Co-author name(s) Nature and % of Co-author's contribution	Co-author(s), Monash student Y/N
2	*Understanding the Warm Water Volume precursor of ENSO events and its interdecadal variation*	*published*	*Methodology, analysis, and writing 85 %*	*Shayne McGregor, methodology and writing 15 %*	*No*

The original paper constitutes the majority of Chapter 2. However, minor modifications have been made in order to generate a consistent presentation within the thesis.

Student signature: Sonja Neske **Date:** 09/09/2019

The undersigned hereby certify that the above declaration correctly reflects the nature and extent of the student's and co-authors' contributions to this work.

Main Supervisor signature: **Date:** 09/09/2019

Acknowledgements

This research was funded by the Monash International Postgraduate Research Scholarship (MIPRS), the Monash Graduate Scholarship (MGS), and the Australian Research Council's Centre of Excellence for Climate System Science (ARCCSS).

As with anything else on this planet, this thesis could not have been completed without the support and assistance of so many people which I am very grateful for.

First of all, I would like to express my deepest appreciation to my supervisor *Shayne McGregor*. Thank you so much for your constructive ideas, feedback and enthusiastic encouragement through all the years of my PhD. I am particularly grateful that you would never hesitate to spontaneously meet for helping with any question. Very motivational for me was to see how you always want the best for your students. Many thanks to *Dietmar Dommenget* for providing invaluable feedback and sharing your innovative ideas which clearly improved this thesis and greatly empowered me. Advice provided by my PhD project panel, *Michael Reeder*, *Julie Arblaster* and *Steven Siems*, to keep my progress on schedule was greatly appreciated. My special thanks are extended to my colleague *Mathias Zeller* – you took the time to patiently help me to run the GFDL-MOM025 simulations and lent me your ear to listen to new ideas for this project.

A huge thanks to my amazing office mates *Cassandra Rogers*, *Sarah Perry* and *Stephanie Jacobs* for providing me with such a warm welcome in Australia and for all your support and friendship during the course of the PhD. Thank you to my fellow PhD students and colleagues at Monash *Christian Stassen, David Hoffmann, Chen Li, Julian Quinting, Christian Wengel, Matthias Retsch, Dongxia Yang, Joshua Soderholm, Roseanna McKay, Zoe Gillett, Marianne Richter, Martin Schwindinger, Anung Samsu, Joel Samsu, Yona Nebel-Jacobsen, Wenhui Zhao* and many others for all your support and all the great times we shared. I would also like to thank all the colleagues from our soccer team for providing a sometimes much needed distraction.

Special thanks go to *Johanna Baehr* and her working group at the University of Hamburg for all your suggestions and support for this project during my 2-month visit. I would also like to thank *Nuno Serra* from the University of Hamburg for all your help regarding my Matlab and Latex questions.

My grateful thanks are extended to *Gillian Simpson* for all your patience in teaching me how to write scientific English throughout my Master and PhD course, but most importantly for your wonderful and supportive friendship over this long distance. Also, many thanks to *Daniela Neske* and *Laura Suarez-Gutierrez* for their valuable layout suggestions and spelling corrections.

I am very grateful for all the support and motivation from my *family* and *friends* back home. Thanks for the huge number of letters you have sent (140 in total!), for all your e-mails, for our skype chats and for every warm welcome when I visited home. Knowing I had your strong support was essential for me to study in a country so far away from home. Special thanks go to my mum for supporting me by sending a letter each month.

Finally, my heartfelt thanks go to my partner *Matze*. Thank you so much for all your warm-hearted support throughout my PhD and our stay in Australia. Your love and humor have made me laugh and powerful in any situation and this thesis would not have been possible without you.

"Being at ease with not knowing is crucial for answers to come to you."

Eckhart Tolle

Contents

List of Figures

List of Tables

Chapter 1

Introduction

1.1 The El Niño-Southern Oscillation

Early recognitions of what is known today as the El Niño-Southern Oscillation (ENSO) date as far back as the late nineteenth century when Peruvian fishermen detected an anomalous warming of water along their coast (e.g. Carrillo, 1893, Clarke, 2008). They called this warming "El Niño" (the Child Jesus) because of its appearance around Christmas time. Some decades later Walker (1924) identified a seesaw in sea level pressure (SLP) between the southern tropical western and eastern Pacific which he called the "Southern Oscillation". It took a further 45 years until Bjerknes (1969) discovered the close connection between El Niño and the Southern Oscillation (ENSO) with both being two different aspects of the same phenomenon. Today we know that despite its name, ENSO evolution is not confined to the southern tropics, but it largely develops in a symmetrical manner around the Equator. It is the largest source of climate variability on interannual timescales on our planet and causes severe near-global climatic conditions (see Section 1.3). However, as it will be shown in this chapter, many details of ENSO dynamics and its predictability remain a major challenge for scientists to understand. Therefore, this thesis aims to enhance the understanding of ENSO dynamics and predictability.

1.2 States of ENSO

In its mean state, the equatorial Pacific sea surface temperature (SST) is relatively cool in the east and warm in the west (Fig. 1.1a). This longitudinal SST difference causes a higher SLP in the east compared to the west, which excites the "Walker Circulation" (Bjerknes, 1969, Fig. 1.2). Hereby, easterlies, known as "trade winds", blow at the surface and this air is heated and supplied with moisture as it moves towards the west Pacific, where it rises and creates a region of persistent precipitation. The air then returns aloft to the eastern equatorial Pacific where it sinks and closes the circulation of a vertical equatorial plane. Effects of the Walker Circulation are not limited to the atmosphere as the ocean's thermocline reflects the SLP difference between east and west: the thermocline is shallower in the east where upwelling occurs due to Ekman divergence and deeper in the west (Fig. 1.1b and Fig. 1.2). The upwelling of cool water in the east in turn underpins the east-west SST gradient.

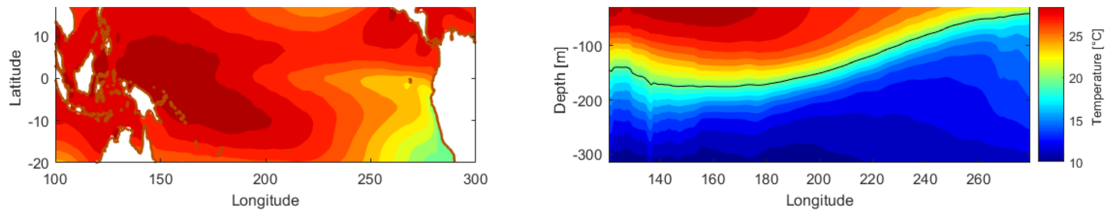

Figure 1.1: (a) Sea surface temperature (SST) [°C] averaged over 1980-2019 using the HadiSST v1.1 data set (Chelton and Risien, 2016). **(b)** Section of potential temperature [°C] averaged over 5°N-5°S and over 1980-2017 using the ORSA4 data set (Balmaseda et al., 2013). Thin black line marks the 20°C isotherme which is an approximation of the thermocline depth.

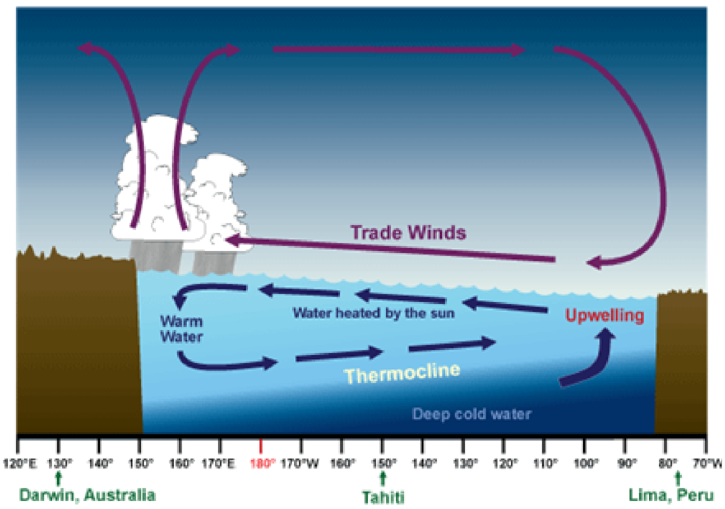

Figure 1.2: Conceptualization of the neutral state of ENSO (source: http://www.weather.gov.sg/wp-content/uploads/2015/03/climate2.png).

In addition to this mean state, Bjerknes (1969) noted a positive feedback (hereafter, Bjerknes feedback) between the strength of the Walker Circulation and eastern Pacific SST. An increase in strength of the Walker circulation implies stronger trade winds which enhance upwelling in the eastern Pacific (Fig. 1.3a). The stronger upwelling of cooler water from lower depths further cools the central/eastern Pacific SST, increasing the contrast between the warm SST in the west and the cool SST in the east (Fig. 1.3c). This strengthening of the zonal SST gradient in turn excites stronger trade winds (Fig. 1.3c). In contrast, if anomalous equatorial westerly winds are present, the Walker Circulation is weakened, which reduces the upwelling of cool water in the east (Fig. 1.3b) leading to anomalous warm SSTs in the central/eastern

Pacific (Fig. 1.3d). Consequently, the weaker zonal SST gradient further weakens the Walker circulation. While the Bjerknes feedback explains the event growth, Bjerknes (1969) could not find an explanation for event ending and new event initialization, with the latter remaining a major challenge to understand today.

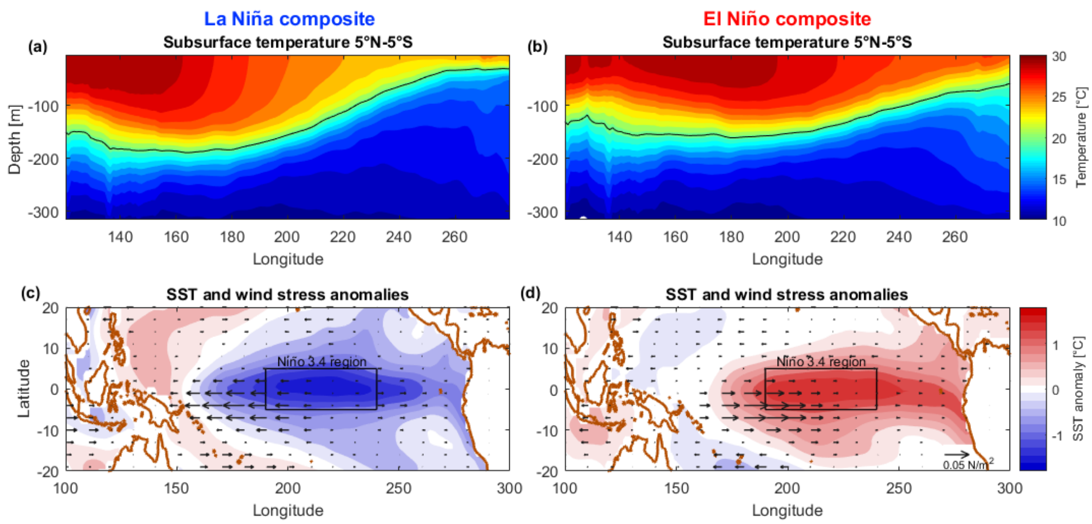

Figure 1.3: Composite potential temperature [°C] (ORSA4 data set, Balmaseda et al., 2013) averaged over 5°N-5°S and over the months December-February (DJF) of **(a)** La Niña and **(b)** El Niño events between 1980-2019 as marked in Fig. 1.4a. Thin black lines mark the 20°C isotherme. Composite SST anomalies [°C] (shading) and wind stress anomalies [N/m^2] (arrows) of DJF during **(c)** La Niña and **(d)** El Niño events. The ERSST v5 (Huang et al., 2018) and ERA-interim (Dee and Uppala, 2009) data sets are used.

Common measures for the ENSO states are: (i) the Southern Oscillation Index (SOI), which describes the standardized SLP difference between Tahiti and Darwin (i.e. an estimate of the strength of the Walker Circulation, gray line, Fig. 1.4a); or (ii) the Niño 3.4 index which measures the SST anomaly averaged over 5°N and 5°S and 170-240°E (black box Fig. 1.3c and d, black line Fig. 1.4a). These two index time series are strongly negatively correlated (correlation=-0.84). Today, the cool state of ENSO with easterly wind anomaly is known as La Niña; and the warm state of ENSO with westerly wind anomaly is known as El Niño. There are a few definitions for an ENSO event, but most commonly an El Niño (La Niña) event is defined when the Niño 3.4 index averaged over three months exceeds (falls below) the 0.5°C (-0.5°C) threshold for at least five consecutive months (https://www.ncdc.noaa.gov/teleconnections/enso/indicators/sst/; dots in Fig. 1.4a).

The average ENSO event starts to evolve in late boreal spring and the events normally peak in boreal winter (Fig. 1.4c and d, Rasmusson and Carpenter, 1982). The anomalously warm or cool state is then obtained until early boreal spring of the following year (Fig. 1.4c and d). ENSO events develop every 2-7 years as can be seen by the strongest power spectral density peaks of the Niño 3.4 time series at these periods (Fig. 1.4b).

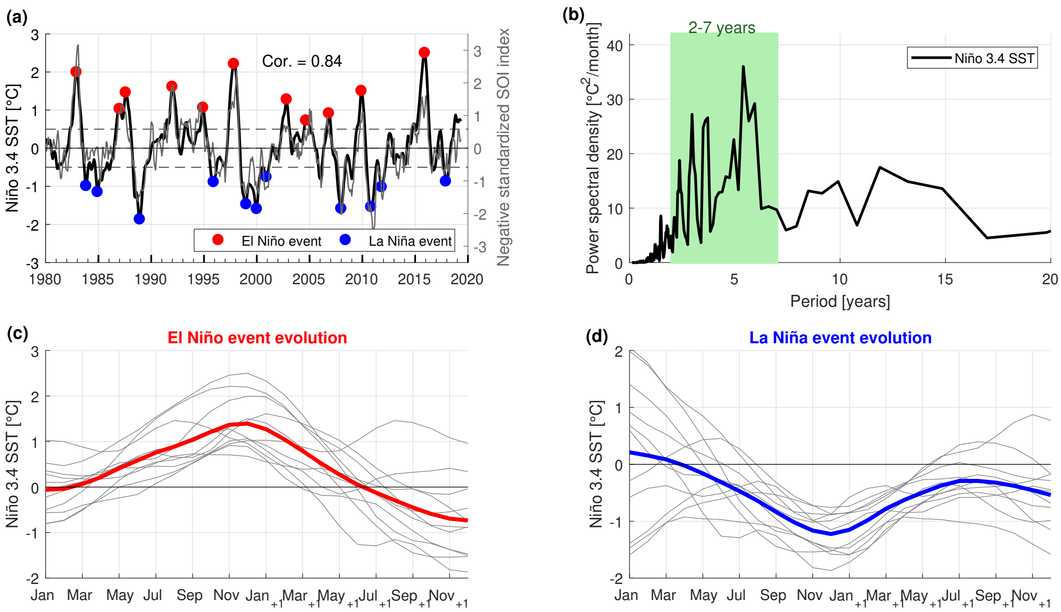

Figure 1.4: **(a)** Monthly mean negative standardized Southern Oscillation Index (SOI, thin gray line) available at https://www.esrl.noaa.gov/psd/gcos_wgsp/Timeseries/SOI/ and Niño 3.4 SST anomaly [°C] (black line) (ERSST v5 anomaly averaged over 170-240°E, see black box in Fig. 1.3c and d). Both time series are smoothed by a 3-month running mean. El Niño (La Niña) events are marked (dots) when the smoothed Niño 3.4 time series exceed (falls below) 0.5°C (-0.5°C, horizontal dashed lines) for at least five consecutive months. **(b)** Power spectral density [°C^2/month] of the smoothed Niño 3.4 SST anomaly (1900-2019) calculated by the Welch's method using a rectangular window with no overlapping. **(c)**/**(d)** Niño 3.4 SSTs [°C] during the El Niño/La Niña year and during the year after the events (as indicated by the month with +1) identified in **(a)**. Thick lines in **(c)** and **(d)** give the average of all event evolutions (thin lines).

1.3 Climatic and socioecological impacts

ENSO's impacts on climate can strongly affect ecosystems and societies (e.g. Glantz et al., 2001, Glantz, 2002, McPhaden et al., 2006). The schematic in Fig. 1.5

summarizes the seasonal effects El Niño (Fig. 1.5a) and La Niña (Fig. 1.5b) events have on temperature and precipitation in the tropics and remote regions. These impacts are averaged over the months December to February when ENSO reaches its maximum (see Fig. 1.4c and d), however, it is noted that ENSO's strongest impacts may not always occur in boreal winter (e.g. Halpert and Ropelewski, 1992, Diaz et al., 2001). This section provides a broad overview and explanation of the climatic impacts shown in Fig. 1.5, and it gives some examples of their socioecological consequences.

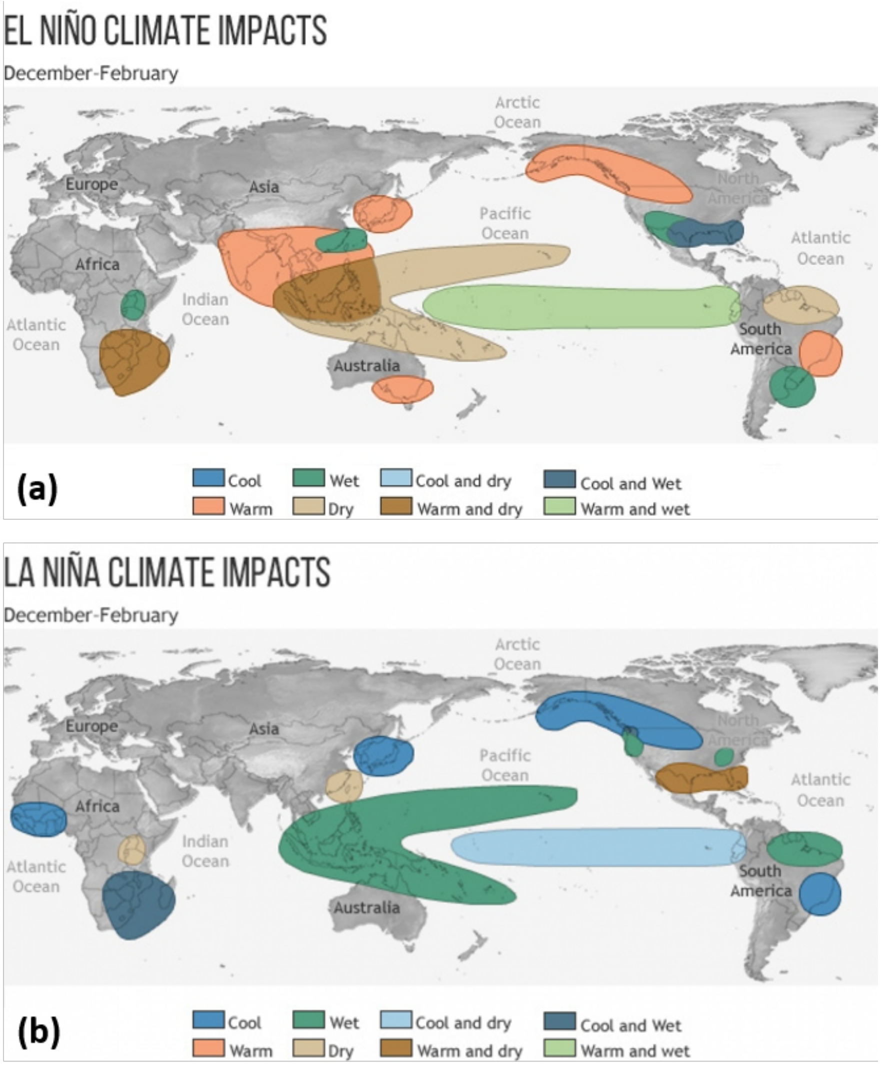

Figure 1.5: Schematic illustration of temperature and precipitation anomalies averaged over the months December-February during **(a)** El Niño and **(b)** La Niña events. Figure adapted from weather.gov.

1.3.1 Impacts of ENSO in the tropical Pacific regions

During El Niño events, the warming of the central/eastern Pacific SST (Fig. 1.3d) induces an eastward movement of the region of persistent precipitation from the western Pacific into the central/eastern Pacific. As a result, coastal areas of the western tropical Pacific become warmer and drier than normal and the eastern Pacific becomes anomalously warm and wet (Fig. 1.5a). Droughts in Indonesia and north east Australia become more common during El Niño conditions (e.g. Vicente-Serrano et al., 2011), with more severe heat waves in north east Australia during El Niño years for example (e.g. Loughran et al., 2017). On the eastern side of the Pacific basin, enhanced rainfall and flooding occurs in the normally arid coastal plains of Peru (e.g. Glantz et al., 2001). Additionally, the suppressed upwelling of nutrients to the euphotic zone (the layer closer to the surface which receives enough light for photosynthesis to occur) in the eastern Pacific negatively impacts fisheries (Glantz et al., 2001, Ordinola, 2002). Moreover, these changes in climatic conditions and marine ecosystem during El Niño events are suspected to cause epidemic diseases (e.g. cholerae and severe diarrhea) in South America (e.g. Gil et al., 2004, Lama et al., 2004).

During La Niña events a stronger Walker Circulation pushes the region of warmest water further westward so that the region of persistent precipitations reaches onto the maritime continent leading to unusually wet conditions in Indonesia and Australia (Fig. 1.5b). On the contrary, the coastal regions around the eastern Pacific become drier and cooler during La Niña years (Fig. 1.5b), which is associated with severe droughts in the tropical coastal areas of South America (Ordinola, 2002). In this case, the enhanced upwelling in the tropical eastern Pacific during La Niña years has a positive impact, as it leads to higher fish yields in Peru (Ordinola, 2002).

1.3.2 Remote impacts of ENSO

ENSO's impacts can reach as far as to much of North and South America, east- and southeast Asia, much of Australia and Africa (Fig. 1.5). The process by which ENSO events influence remote areas is driven by the movement of the regions of persistent precipitation (e.g. Sarachik and Cane, 2010). In regions of precipitation, thermal forcing of the atmosphere occurs due to the latent heat release in the process of cumulus condensation and precipitation. The rising air in these regions eventually diverges which excites planetary waves at the upper levels of the atmosphere. These waves propagate zonally away from the region transporting their anomalous signal to the tropical Indian and Atlantic basins (e.g. Gill, 1980). For example, the Indian Ocean SST is anomalously warm during El Niño events (e.g. Xie et al., 2009), and India's summer monsoon is suppressed (expanded) during El Niño (La Niña) years which leads to devastating droughts (floods) (e.g. Xavier et al., 2007). ENSO's strong signal can even excite other modes of climate variability in the Atlantic and Indian ocean basins (for instance the Indian Ocean Dipole) which can then feedback onto the Pacific (Cai et al., 2019). The planetary waves not only impact the remote tropics, but they also influence the jet stream, bringing air of anomalous temperature and humidity to higher latitudes (e.g. Sarachik and Cane, 2010, Fig. 1.5).

The details of ENSO's teleconnections are far more complex than presented in this subsection, and it is an area of research that remains a challenge for scientists today (e.g. Sarachik and Cane, 2010). Each ENSO event is unique (e.g. Timmermann et al., 2018) with their diverse spatial and temporal evolutions leading to differing regional impacts (e.g. Hoerling and Kumar, 1997, Power et al., 1999, Wang and Hendon, 2007, Capotondi et al., 2015). In Australia for instance, the strength of an El Niño event cannot be simply linearly related to its impacts (Power et al., 2006, Wang and Hendon, 2007, Chung and Power, 2017).

1.4 The two steps to making a reliable ENSO prediction

It is obvious from Section 1.3 that agriculture, water management, energy use, fisheries, risk management, health care and many other sectors in many regions around the globe would strongly benefit from reliable seasonal climatic predictions. The first step towards making a reliable prediction for societies in a specific region is to improve the understanding of the impacts a certain state of ENSO has on that region (Section 1.2). The second step is to improve the accuracy of the prediction of ENSO events themselves and to enhance the lead times of the prediction. The improvement of ENSO prediction is thought to rely at least partially on improvements in our dynamical understanding of ENSO (Section 1.1). This thesis will focus on the latter; enhancing the dynamical understanding of ENSO to help making reliable predictions of ENSO events. Thus, the following sections will provide an overview of our today's dynamical understanding of ENSO.

1.5 ENSO dynamics– traditional ENSO theories

The question of a turnabout from El Niño to La Niña events and vice versa remained over the decades after Bjerknes' (1969) seminal work which explained the positive feedback of ENSO event growth (Section 1.1). In the 1980's and 1990's four main ENSO theories were formulated to explain a negative feedback, and all presented ENSO as a self-sustained oscillation. These theories were: (i) the delayed oscillator (Suarez and Schopf, 1988, Battisti and Hirst, 1989); (ii) the recharge-discharge oscillator (Jin, 1997); (iii) the western Pacific oscillator (Weisberg and Wang, 1997, Wang et al., 1999); and (iv) the advective-reflective oscillator (Picaut et al., 1997). These models rely on ordinary differential Equations to represent the development of eastern Pacific SST anomaly. At the core of each model lies the Bjerknes feedback, but what differs between them is the negative feedback that initiates a change of ENSO phase. This subsection will briefly explain two of these four theories: the delayed oscillator and the recharge-discharge oscillator. The former is being explained as it is implicitly incorporated in the latter, which is often considered as the leading ENSO paradigm. A summary of all four theories and a unified model of them can be found in Wang and Picaut (2004).

1.5.1 The delayed oscillator model

Nearly at the same time Suarez and Schopf (1988) and Battisti and Hirst (1989) proposed a model to explain the delayed demise and phase change of ENSO events (Fig. 1.4c and d). They assumed that the positive Bjerknes feedback of event growth is reversed around 6-9 months after initiation by a delayed negative feedback underpinned by oceanic Rossby waves (RWs). The equation for the delayed oscillator model is the following:

$$\frac{dT}{dt} = \frac{ad}{R}T - \frac{bd}{R}T(t-\eta) - \epsilon T^3; \tag{1.1}$$

where T is the SST anomaly in the equatorial eastern Pacific, t is time, the parameters a, d and b represent constants, the parameters R and ϵ are damping coefficients, and η denotes the delay time. The first term on the right-hand side (RHS) of Equation 1.1 represents the positive Bjerknes feedback of ocean atmospheric coupling. The second term on the RHS of Equation 1.1 gives the negative feedback of wind forced oceanic RWs. This negative feedback can be demonstrated by a simple shallow water model (SWM, see Appendix Chapter 2 Text A2.1 or Neske and McGregor, 2018, for SWM details) simulation forced by a westerly wind anomaly (Fig. 1.6). For example, during El Niño conditions the anomalous westerly winds in the central equatorial Pacific (Bjerknes feedback, Fig. 1.6a) force: (i) downwelling eastward traveling oceanic Kelvin waves (KWs) that further warm eastern Pacific SSTs and enhance the event growth; and (ii) upwelling westward traveling oceanic RWs either side of the equator (RWs, Fig. 1.6b). The delayed effect several months later is due to most of the downwelling KW signal leaving the equatorial region at the eastern boundary, while the upwelling RWs reflect at the western boundary and are converted into eastward traveling upwelling equatorial KWs. These upwelling KWs eventually shallow the thermocline in the eastern Pacific (Fig. 1.6c). This delayed effect cools the eastern Pacific SST and conditions the system for a La Niña event. During a La Niña event the easterly winds then have the opposite effect.

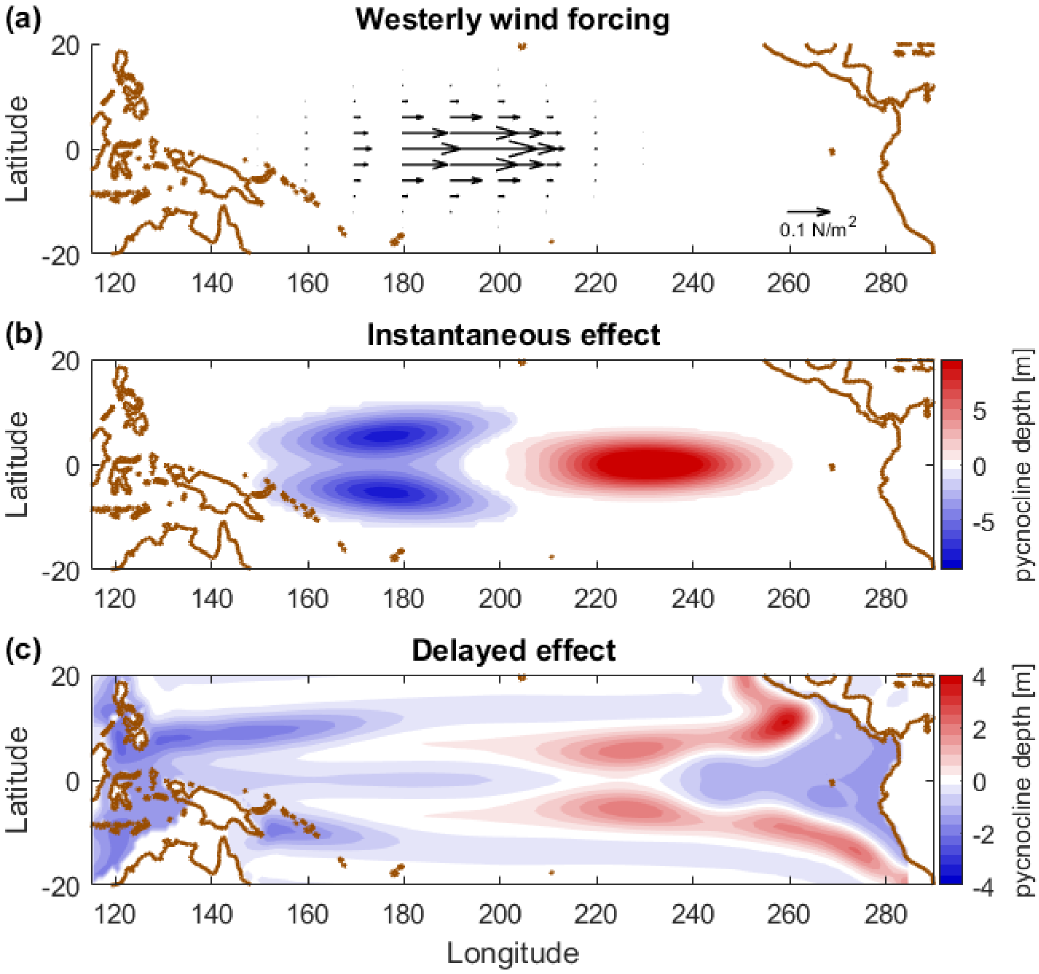

Figure 1.6: Pycnocline outcome of a shallow water model simulation **(b)** and **(c)** forced by westerly wind stress **(a)**. The westerly wind (U) is Gaussian in time (t), longitude (x) and latitude (y): $U(x,y,t) = U_0 exp[-(\frac{x-X_0+t}{L_x})^2]exp[-(\frac{y-Y_0+t}{L_y})^2]exp[-(\frac{t-T_0}{T_e})^2]$, where U_0 is set to 21 m/s, X_0 and Y_0 mark the spatial center (0°Latitude, 180°Longitude), L_x (=1.85·10^6 m) is the longitudinal, and L_y (=0.7·10^6 m) is the latitudinal e-folding scale, T_0(=10 days) gives the day of maximum wind and T_e (=3 days) is the e-folding time scale. U is converted to wind stress using the linear stress law. **(a)** shows the maximum wind stress forcing [N/m^2] at day 10, **(b)** shows the instantaneous effect of the wind forcing (20 days after the maximum forcing) and **(c)** shows the delayed effect (130 days after the maximum forcing).

1.5.2 The recharge-discharge oscillator model

In contrast to the delayed oscillator which emphasizes wave dynamics, Jin (1997) based his recharge-discharge oscillator (RDO) theory on the sea level observations of Wyrtki (1975, 1985): Wyrtki (1975, 1985) shows that the sea level in the western Pacific rises before and during El Niño phases, and then declines as the warming approaches its peak. He hypothesized that an El Niño event ends when this buildup of warm water flows eastward and then poleward along the American coast, and that the next event could not occur until another buildup of warm water had taken place. What Wyrtki (1975, 1985) could not explain was the exact connection between one event and the next. This connection was formulated by Jin (1997) using the following theoretical model:

$$\frac{dT}{dt} = RT + \gamma h; \tag{1.2}$$

$$\frac{dh}{dt} = -\alpha bT - rh; \tag{1.3}$$

where T is the SST anomaly in the equatorial eastern Pacific, h is the anomalous thermocline depth in the equatorial western Pacific, t is time, and the parameters R, γ, α, b and r represent constants. The recharge-discharge oscillator involves a coupling between eastern Pacific SST and the western Pacific thermocline which represents the sea level anomaly and is consistent to the upper ocean heat content (Rebert et al., 1985, Equation 1.2 and Equation 1.3). The oscillation results from the non-equilibrium between the western Pacific thermocline depth anomaly and changes in SST in the eastern Pacific. Thus, in contrast to the delayed oscillator detailed wave propagation process is not explicitly considered, the "*equatorial wave dynamics are collectively viewed as an ocean adjustment process to redistribute mass and heat under changing wind stress forcing*" (Jin, 1997).

The dynamics of the RDO are illustrated in Fig. 1.7: during the warm phase of ENSO anomalous westerlies cause an anomalous tilt of the thermocline in the direction of the winds (Fig. 1.7a). The curl of the anomalous westerly winds is associated with a poleward Sverdrup transport ($V = curl_z\tau/\beta$, with V being the Sverdrup transport, $curl_z\tau$ is the curl of the horizontal wind stress and β is the meridional gradient of the Coriolis force) in each Hemisphere (Fig. 1.7a). The divergence of zonally integrated Sverdrup transport eventually results in a discharge of heat content which shallows the entire equatorial Pacific thermocline (Fig. 1.7b). As a result, upwelling of anomalously cool water in the eastern Pacific cools the eastern Pacific SST leading to a La Niña event (Fig. 1.7c). The anomalous cool SST in the eastern Pacific induces anomalous easterlies and causes a recharge of upper ocean heat content due to a convergence of Sverdrup transport (Fig. 1.7c and d). The recharge then conditions the system to start a new cycle.

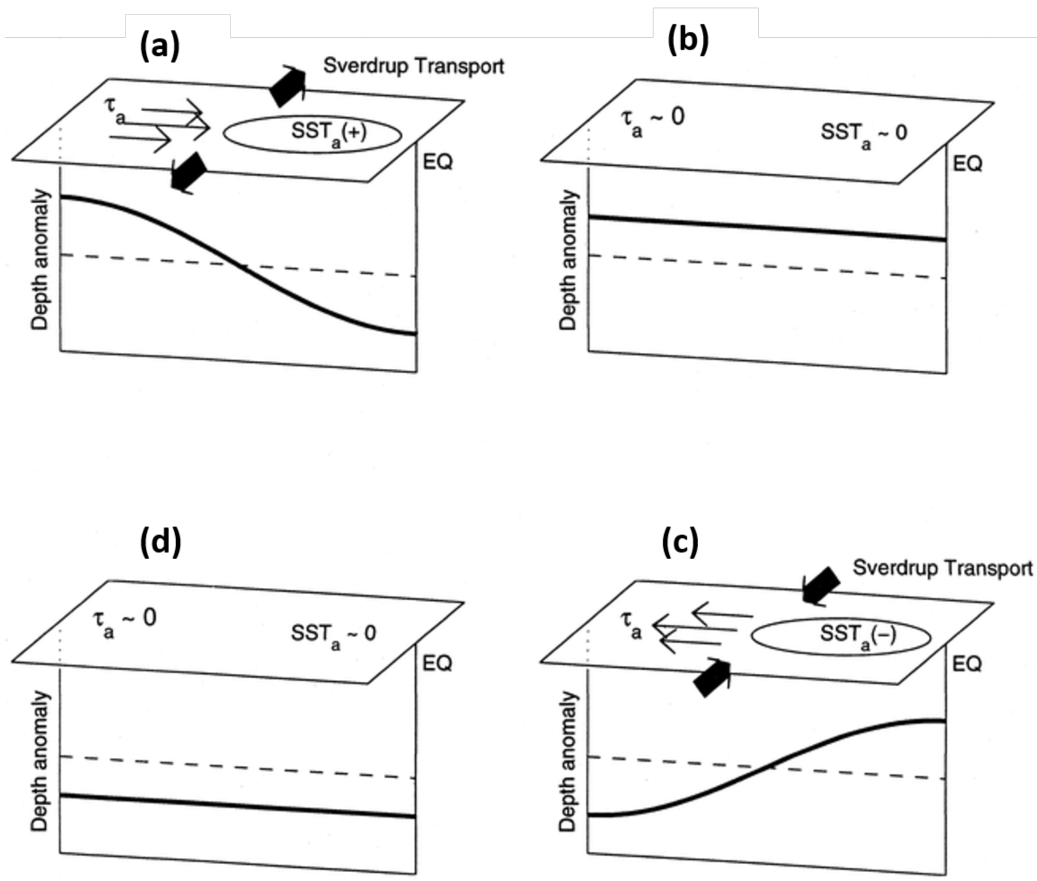

Figure 1.7: Conceptualization of the recharge-discharge oscillator (Jin, 1997) with SST_a being the anomalous sea surface temperature in the eastern equatorial Pacific and τ_a represents the anomalous zonal wind stress in the central equatorial Pacific. The thick black line marks the anomalous thermocline depth. This figure is adapted from Meinen and McPhaden (2000).

Although not explicitly expressed in the RDO theory, the mass adjustment can be considered (as with Sverdrup transport) as being achieved through the propagation of oceanic KWs and RWs similarly to the delayed oscillator. The Sverdrup transport at a certain latitude on a longitudinal band is the sum of the zonally and vertically integrated meridional geostrophic velocity, and the zonally integrated meridional Ekman transport:

$$V = \int_{x=E}^{x=W} \int_{z=0}^{z=h} \frac{g}{f} \frac{d\eta}{dx} dz dx + \int_{x=E}^{x=W} \frac{-\tau^x}{\rho f} dx; \tag{1.4}$$

where V is the Sverdrup transport, E and W describe the eastern and western zonal boundaries, h is the thermocline depth (see Bosc and Delcroix (2008) for a discussion about the integration depth for an estimate of geostrophic transports), g is the Earth acceleration, η is the sea surface height (SSH), τ^x is the zonal wind stress, ρ is the water density, and f is the Coriolis force. The instantaneous effect of a westerly wind is the recharge of equatorial upper ocean heat content due to converging Ekman transports (second term on the RHS of Equation 1.4, Fig. 1.6a and b). This recharge of upper ocean heat content is due to the dominance of wind forced downwelling KWs (Fig. 1.6b). At this stage there is no meridional geostrophic transport (first term on the RHS of Equation 1.4) as the positive and negative SSH gradients on each zonal side of the RWs and KWs cancel each other (Fig. 1.6b). The geostrophic transport begins when the KWs and RWs meet the eastern and western boundary respectively, inducing changes in zonal SSH gradient which cause a discharge of equatorial upper ocean heat content. Thus, the sum of the time integrated Ekman and geostrophic transports (i.e. the Sverdrup transport) will lead to a delayed discharge of upper oceanic heat content (Fig. 1.6c) when the RWs and KWs have met the boundaries which is required to reach the adjusted state.

The benefit of the RDO formulation by not explicitly considering these wave dynamics, is that it provides a variable (i.e. the upper ocean heat content) that is easily observed and accessible for observational ENSO studies.

1.6 The RDO theory under review– our current understanding

The traditional ENSO models are milestones in research, highlighting the most important feedbacks of this phenomenon. During the past 20 years our understanding of ENSO has, however, further evolved demonstrating new layers of complexity (e.g. Timmermann et al., 2018, Santoso et al., 2019) that cannot be accounted for by traditional linear ENSO theory. Improvements in our understanding of ENSO stem from: (i) the observing system built during the 1980's and early 1990's to monitor key variables for ENSO in the equatorial Pacific region (McPhaden et al., 2010); and (ii) the improvement of coupled climate models.

1.6.1 Observational evidence of the RDO theory

Over the past decades, most attention was placed on Jin's (1997) RDO theory whose main concept was confirmed by several observational studies. The equatorial Pacific upper ocean heat content is: (i) re-/ and discharging due to the converging and diverging effects of the sum of meridional Ekman and geostrophic transports (Meinen and McPhaden, 2001, Bosc and Delcroix, 2008); and (ii) leading ENSO SST by 1-3 seasons (Fig. 1.8b and c; Meinen and McPhaden, 2001, McPhaden, 2003, 2012, Horii et al., 2012, Bunge and Clarke, 2014). From these studies, the variable warm water volume (WWV) has been established to describe upper ocean heat content in the equatorial Pacific band. The WWV is the anomalous thermocline depth integrated over the region 120-280°E and 5°N-5°S (black box in Fig. 1.8a), and due to its role as a precursor of ENSO the WWV is thought to be the primary source of predictability for ENSO (e.g. McPhaden et al., 2010). Therefore, examinations of the WWV variable are the core of this thesis.

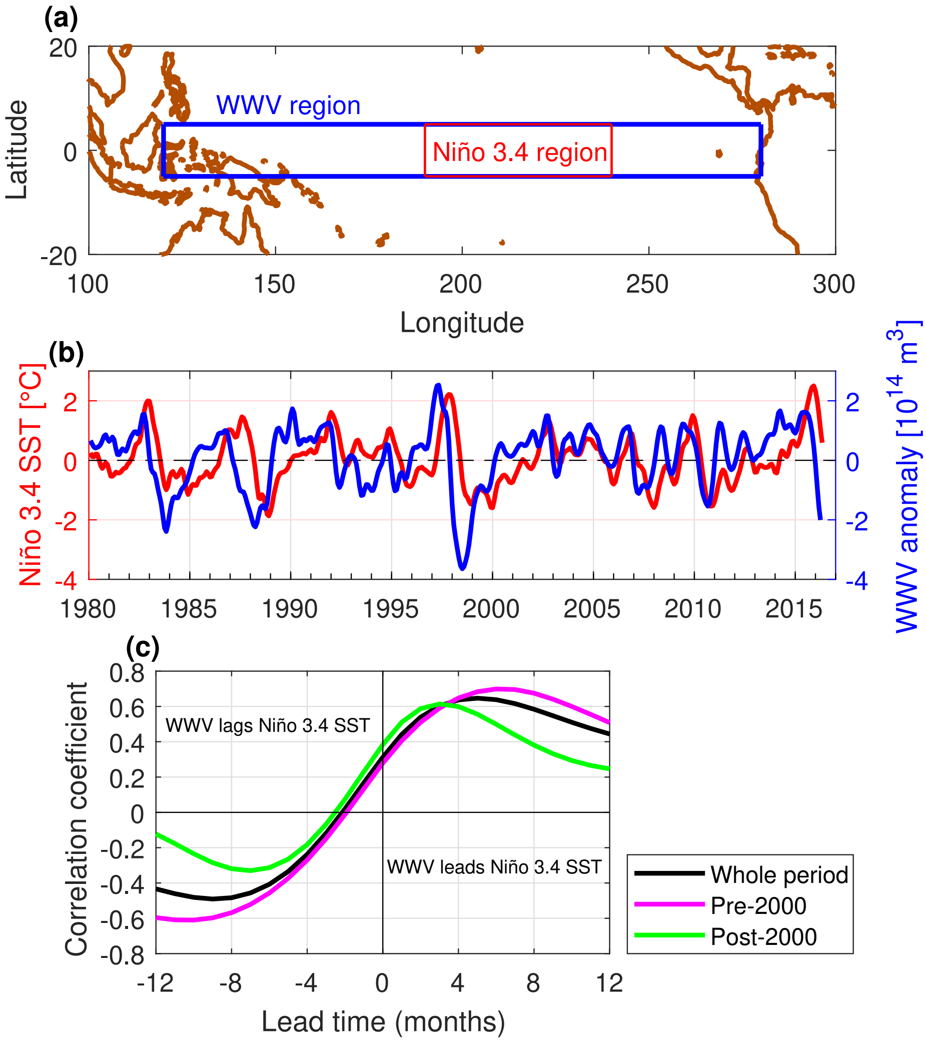

Figure 1.8: **(a)** The locations of the warm water volume (WWV, blue box) and Niño3.4 (red box) regions are presented. **(b)** Niño3.4 SST anomaly [°C] (red line, estimated from ERSST v5 anomaly Huang et al., 2018) and observed WWV anomaly [m^3] (blue line, taken from: https://www.pmel.noaa.gov/tao/wwv/data/). Both time series are smoothed by a 3-months running mean. **(c)** Lead-lag correlation between both time series in **(b)** during: (black line) the whole period; (magenta line) the pre-2000 period; and (green line) the post-2000 period.

1.6.2 Complexity of ENSO dynamics and remaining questions

Despite of the existence of the RDO theory and the observational evidence linking WWV and ENSO SST, certain aspects of ENSO remain unclear. A prime example of our confusion is the predicted El Niño of the winter 2014/15. Despite being widely predicted, this event failed to manifest and developed one year later as one among the three strongest El Niño events during the past four decades (Fig. 1.4a, McPhaden, 2015, Levine and McPhaden, 2016). The 2014/15 El Niño did not manifest despite strong equatorial Pacific westerly wind events (high frequency wind variability which is separated from the ENSO cycle itself and is thought to trigger ENSO events, e.g. Giese and Harrison, 1990, Harrison and Vecchi, 1997) and a strong WWV recharge were evident in boreal winter and spring 2014 (e.g. Hu and Fedorov, 2016, Levine and McPhaden, 2016, McGregor et al., 2016). As this example of the failed El Niño manifestation demonstrates the WWV anomaly is a necessary but not a sufficient precondition for and ENSO event (Kessler, 2002, Philander and Fedorov, 2003, Zavala-Garay et al., 2004).

Moreover, there is an observed decrease in WWV/ENSO SST lead time from around three seasons in the 1980's and 1990's to only one season during the post-2000 period (Fig. 1.8c; McPhaden, 2012, Horii et al., 2012, Bunge and Clarke, 2014). The reason for this shortening in WWV/ENSO SST remains unclear and, it is consistent with a lowering in predictable skill of ENSO for the post-2000 period (e.g. Wang et al., 2010, Barnston et al., 2012, Kumar et al., 2015). Thus, a better understanding of the dynamics causing this shortening in lead time has the potential to deepen our understanding of ENSO predictability itself.

Additionally, there is a clear ENSO asymmetry evident with a certain amount of WWV recharge leads to stronger El Niño SSTs than the same amount of WWV discharge leads to La Niña SSTs (Fig. 1.8b and Fig. 1.9a-c, e.g. Meinen and McPhaden, 2000). The ENSO asymmetry can also be seen in the duration and phase change transition, with El Niño events being of shorter duration and having a stronger tendency to be followed by La Niña events than vice versa (Fig. 1.4c and d, e.g. Kessler, 2002, Larkin and Harrison, 2002, Okumura and Deser, 2010, Guan et al., 2019).

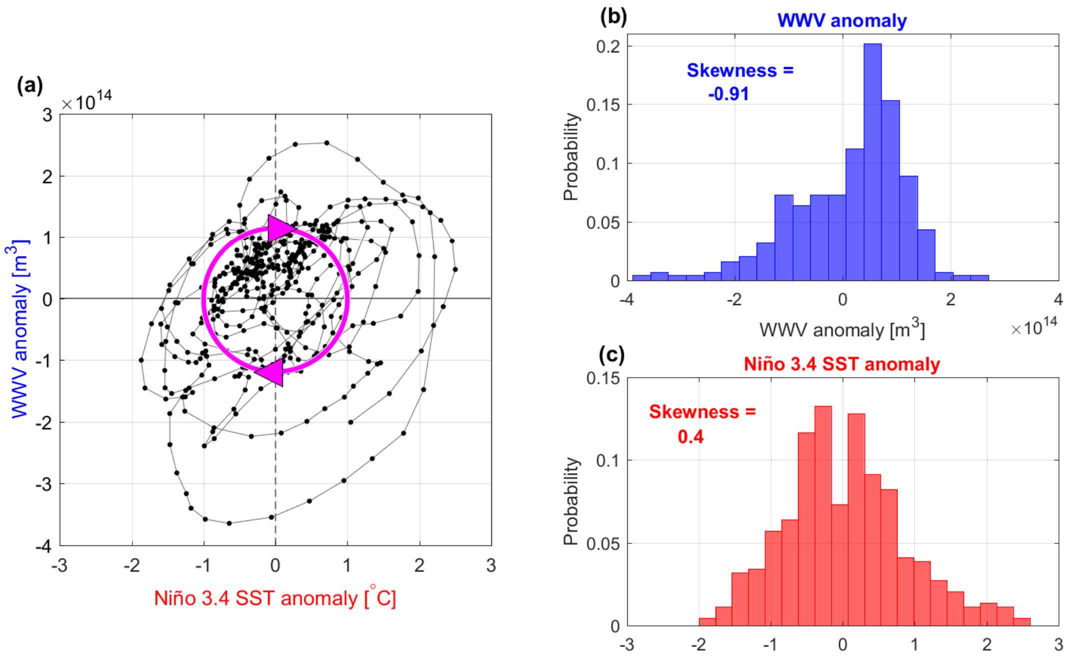

Figure 1.9: **(a)** Phase orbits of both time series shown in Fig. 1.8b with Niño3.4 SST anomaly [°C] being plotted against the x-axis and WWV anomaly [m^3] being plotted against the y-axis. Magenta circle sketches the dynamics of the recharge-discharge oscillator (Jin, 1997). **(b)** and **(c)** show the probability distributions of the WWV anomaly and Niño3.4 SST anomaly respectively.

Moreover, the climate system can rest for up to 2 years in a weakly-recharged weak cool state (Fig. 1.9a, Meinen and McPhaden, 2001, Kessler, 2002, Timmermann et al., 2018). This long "break" of the cycle clearly challenges the view of the WWV anomaly precursor being built by adjusted ocean responses of the winds during a preceding La Niña event. Within around 2 years any memory of the winds in the equatorial ocean is lost and the new buildup of WWV preconditioning the system for an El Niño event cannot be due to the adjusted response of an easterly wind anomaly of a preceding La Niña event.

An explanation for these aspects of ENSO which cannot be explained by traditional ENSO theory is sought in KWs, which are forced by sudden wind events (e.g. see example Fig. 1.6a and b) and which are not considered in the RDO theory. These KWs have been shown to provide important instantaneous (time scale of around 1-3 months) contributions to observed WWV changes determining ENSO event initiation and/or evolution (Weisberg and Wang, 1997, McPhaden and Yu, 1999, Boulanger et al., 2003, Bosc and Delcroix, 2008, McGregor et al., 2016, Izumo et al., 2019). What remains unclear is the relative weighting between this instantaneous WWV contribution and the adjusted WWV contribution considered in traditional theories as well as the consequences this weighting has as on ENSO. Thus, the core of this thesis builds the separation of these two WWV components. In particular, pre- and post-2000 differences are examined to gain more understanding of the post-2000 decline in ENSO prediction skill.

1.7 Thesis Aims and Outline

The aim of this thesis is to gain a better understanding of the drivers of this WWV precursor (i.e. through the instantaneous or adjusted wind responses), as we expect a better understanding of ENSO precursor dynamics to enhance our understanding of ENSO and potentially improve its predictability. Chapters 2, 3 and 4 are structured as individual studies, with each chapter having its own Introduction, Methods, Results, Summary and Conclusion sections. For brevity the references of each of these chapters are collated in a comprehensive reference list at the end of the thesis. Chapter 5 provides summary, conclusions and some future perspectives.

In **Chapter 2** a wind forced oceanic SWM is used to separate the observed WWV changes into instantaneous (short time scale, 1-3 months) and adjusted (long time scale $>$3 months) wind responses. The relative weighting of both responses is examined over the whole study period (1980-2016), and also separately over the pre- and post-2000 periods. For both periods, the lead time of each component to ENSO SST is determined and compared to the lead time of the whole WWV ENSO SST (i.e. Fig. 1.8c). Finally, differences in the relative weighting of both components during re- and discharged periods are investigated to better understand ENSO asymmetry.

The results from Chapter 2 demonstrate a post-2000 decline in the adjusted WWV component while at the same time the equatorial wind stress has not declined. This work is published in *Geophysical Research Letters*.

Chapter 3 aims to reconcile the conflicting changes in instantaneous and adjusted responses by seeking to understand the role of changes in wind stress patterns and their wind stress curl. To do so, the adjusted responses following the 23 strongest equatorial wind periods are categorized according to their strength using SWM simulations. Further, the wind stress pattern of each category is examined and compared. Then the SWM and the global ocean sea ice GFDL-MOM025 models are forced with these winds to understand how the wind pattern has influenced the wave dynamics causing the different adjusted responses. Hereby, pre- and post-2000 differences as well as El Niño and La Niña asymmetries are examined.

Chapter 3 emphasizes the important role of wind stress curl over wind stress in order to understand the details of ENSO dynamics. This work is submitted for publication to the *Journal of Climate*.

Building on the insights of Chapter 3, in **Chapter 4** a stochastic regression model is build to reconstruct the adjusted WWV changes from wind stress curls in different regions around the tropical Pacific region. This study deepens the understanding of Chapter 3 by attributing post-2000 adjusted WWV changes to: (i) STD declines of the wind stress curls in the different specific regions; (ii) changes in the frequencies of the wind stress curl time series; and (iii) the interference of RW signals across different regions. The main results of the regression model are compared to a Rossby wave projection model to make a robust study. And finally, it will be shown for which regions the wind stress curl rather than the wind stress is indispensable for explaining ENSO dynamics.

Chapter 2

Understanding the warm water volume precursor of ENSO events and its interdecadal variation

This chapter is based on the publication:

Neske, S. and McGregor, S. (2018), 'Understanding the warm water volume precursor of ENSO events and its interdecadal variation', *Geophysical Research Letters*, **45**(3), 1577-1585.

Preface

A wind forced ocean model is used to decompose the equatorial Pacific warm water volume (WWV) between 1980-2016 into two components, the (i) adjusted wind response, which is found by letting the model evolve unforced for three months; and (ii) instantaneous wind response, which are the instantaneous WWV changes due to Ekman transports. Our results suggest roughly half of WWV variability is only as predictable as the winds that drive the instantaneous change. Separate examinations of pre- and post-2000 periods reveal: (i) nearly equal importance of instantaneous and adjusted responses for the pre-2000 period; and (ii) dominance of the instantaneous response during the post-2000 period, which is most apparent during the recharged phase. This increasing instantaneous contribution prominence explains the post-2000 reduction in WWV/ENSO sea surface temperature lead times (from 6-9 months pre-2000 down to 3-months post-2000) and is consistent with the reduction in post-2000 ENSO prediction skill.

2.1 Introduction

The El Niño-Southern Oscillation (ENSO) is an ocean-atmosphere climate phenomenon which dominates interannual variability in the equatorial Pacific. Its ocean component consists of anomalous warming (El Niño) and cooling (La Niña) of eastern tropical Pacific sea surface temperatures (SSTs) with an approximate period of 2-7 years. ENSO events have been connected with severe climate events such as droughts, heavy rainfall, storms, floods and/or heat waves in many regions around the globe (Diaz et al., 2001, McPhaden et al., 2006, Sarachik and Cane, 2010). An enhanced understanding and a precise prediction of ENSO states is essential to enable societies to prepare for such climatic events.

Early studies of Bjerknes (1969), Wyrtki (1975, 1985) and Cane and Zebiak (1985) laid the foundation of our current conceptual understanding of ENSO. Jin's (1997) recharge-discharge oscillator (RDO) theory summarized this early work by describing ENSO as a self-sustained cycle: During El Niño (La Niña) events, equatorial westerly (easterly) wind anomalies and eastern tropical Pacific positive (negative) SST anomalies reinforce each other (Bjerknes feedback), at the same time as the oceanic adjustment to these winds acts to discharge (recharge) equatorial upper ocean heat content and leads to a change in the phase of ENSO. The main characteristics of the RDO theory have been confirmed in observational studies, showing that the equatorial Pacific region (120°E-80°W and 5°N-5°S) upper ocean heat content (also commonly known as warm water volume, WWV) leads the ENSO SST by 1-3 seasons (Meinen and McPhaden, 2000, 2001, Bosc and Delcroix, 2008, McPhaden, 2012). The relationship between WWV and ENSO SST also highlights the role of heat content as a precursor of ENSO and as the primary source of predictability for ENSO (e.g. McPhaden et al., 2010). Additional theories, which include the delayed oscillator (Suarez and Schopf, 1988) and the western Pacific oscillator (Weisberg and Wang, 1997), were also proposed to describe dynamics underlying ENSO and representing it as a self-sustained cycle.

In spite of the existence of the RDO theory linking WWV and ENSO some aspects of this relationship remain unclear. Firstly, the post-2000 reduction in WWV vs. ENSO SST lead times, which started with WWV leading SSTs by 6-9 months between 1980-1999, reduced to a 2-3-month lead time during the 2000-2010 period (McPhaden, 2012, Horii et al., 2012, Bunge and Clarke, 2014). This change in lead time has also been accompanied by an apparent reduction in the predictive skill of ENSO in the post-2000 period (e.g. Wang et al., 2010, Barnston et al., 2012, Kumar et al., 2015). Secondly, the Pacific climate system can pause for up to two years (far longer than the ocean dynamic memory of the region) in a weakly-recharged, weak La Niña state, prior to El Niño events (Kessler, 2002). And thirdly, Boulanger et al. (2003) demonstrated that 80% of the Kelvin wave signal at 175°E (1993-2001) is wind induced rather than being the adjusted contribution of the Rossby wave reflection. This raises questions over the cyclicity of ENSO, and raises the possibility of ENSO being a series of events with specific triggers (e.g. Thompson and Battisti, 2001, Fedorov et al., 2015), rather than a self-sustained cycle.

As to what causes the WWV recharge (discharge) prior to an El Niño (La Niña) event if the events are not part of a self-sustained cycle, McGregor et al. (2016) demonstrated that bursts of anomalous winds produce near instantaneous WWV response that is only as predictable as the forcing wind event itself, while the adjusted WWV response, which is referred to by the RDO theory, is predictable months in advance due to the slowly evolving nature of the ocean. What is currently unknown, however, is the weighting of the instantaneous and adjusted WWV response in observed WWV.

In this study, we aim to better understand the role of instantaneous vs. adjusted WWV responses in the observed WWV preceding ENSO events between 1980-2016. A better understanding of the drivers of event preceding WWV will provide valuable information of the dynamics and predictability of ENSO events as well as it has the potential to help explain the 21^{st} century reduction in the WWV/ENSO SST lead times.

2.2 Model and experimental Design

An oceanic 1.5-layer shallow water model (SWM) is forced by daily wind stress anomalies from January 1979 to May 2016 (see Appendix Text A2.1 for full SWM details). Forcing is derived from 6-hourly ECMWF (Dee and Uppala, 2009, ERA-interim) 10 m surface winds, which are first converted to wind stresses before daily averages are calculated and the long-term seasonal cycle and linear trend is removed. The model produces daily pycnocline depth anomalies which approximate the thermocline depth anomalies in the tropical Pacific region well (Rebert et al., 1985), which we compare to observed estimates of WWV (Smith, 1995, available at https://www.pmel.noaa.gov/tao/wwv/data/). It is noted that this observed WWV estimate depends on a mix of temperature profiles from different equipment (Smith, 1995) that change over the study period, raising the open question how the uncertainty of WWV estimates change over time and whether this uncertainty may impact results presented herein. However, the fully forced simulation monthly mean equatorial region (120°E-80°W and 5°N-5°S) WWV (red line, Fig. 2.1a) shows strong agreement with observed estimates of WWV (dashed gray line, Fig. 2.1a). Remaining differences between the simulated and observed WVV, though relatively small, may be due to a number of factors including the approximation of the ocean behaving like a 1.5-layer model (e.g. Rebert et al., 1985, Clarke, 2008), errors in the wind stress forcing (e.g. McGregor et al., 2012a) and errors of in-situ measurements (e.g. Gasparin et al., 2015). It is noted that the removal of the linear wind stress acts to slightly enhance the correspondence with observations as observed WWV does not display any significant trend. This WWV discrepancy is at least partly due to the trend contained in the ERA-interim wind stress being larger than that observed in wind stress by TAO observations (Chiodi and Harrison, 2017).

The dynamical model allows us to decompose the WWV signal into its adjusted and its instantaneous WWV contributions. As illustrated in Fig. 2.1b and detailed below, this is done by conducting hindcast experiments initialized on the first day of each month between January 1980 and May 2016. Each of these hindcasts have a wind stress forced spin up of 1 year, before being left to freely evolve unforced (turquoise line, Fig. 2.1b) for 3 months, while for the control simulation the model is kept forced over these 3 months (black circle, Fig. 2.1b). The output from the control simulation (black line, Fig. 2.1a), was close to observations and the fully forced simulation and it is taken for further analysis due to the consistency in the model spin up.

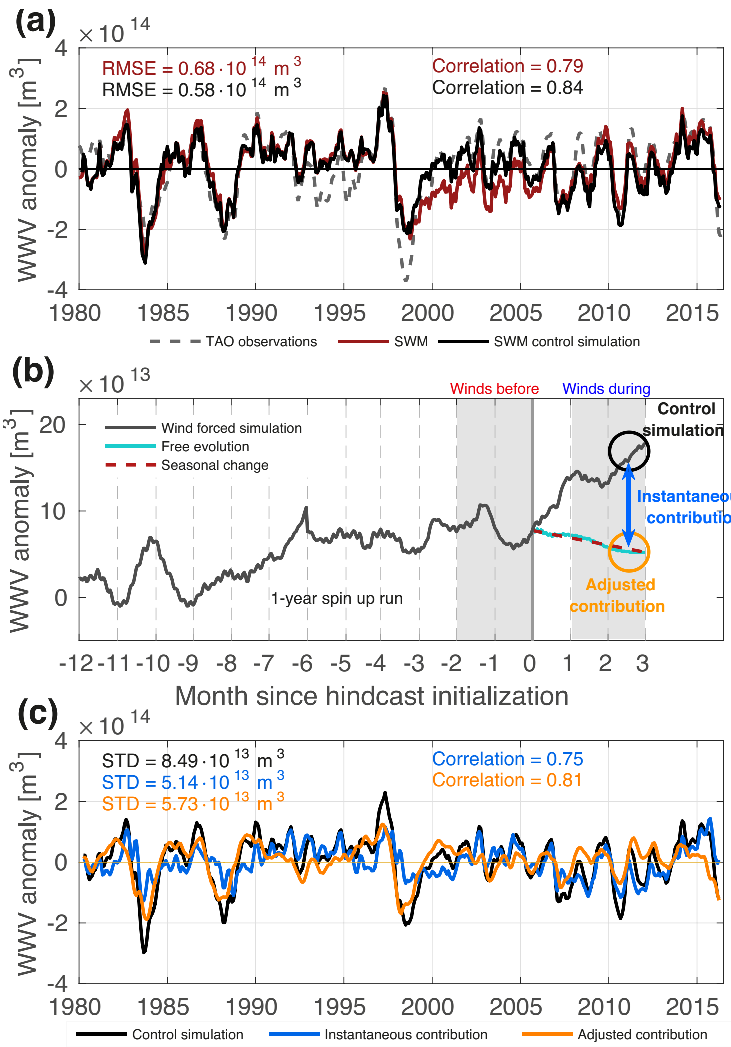

Figure 2.1: **(a)** Monthly mean WWV anomaly [m^3] from observations (gray dashed line), the fully forced simulation (red line) and the control simulation (black line); correlations and RMSEs are calculated between the simulated and observed WWVs. **(b)** Sketched example WWVs from a hindcast run initialized on 07/01/1982 and its decomposition into instantaneous and adjusted WWV contributions. **(c)** Smoothed control simulation WWV [m^3] (black line) and its adjusted (orange line) and instantaneous (blue line) contributions as described in Section 2. Correlations are calculated between the control simulation WWV and each WWV contribution.

Adjusted WWV: As Kelvin waves cross the Pacific basin in 1-2 months, any Kelvin wave initiated by wind events in the equatorial Pacific (prior to the wind stresses being switched off) would have reached the Pacific basins eastern boundary during the third month of free ocean evolution and taken the majority of their associated WWV poleward (McGregor et al., 2016). Consequently, the WWV signal during the third month of free ocean evolution would be due to the effect of Rossby waves, excited by winds 2 or more months ago, reflecting into the WWV region at the western boundary (McGregor et al., 2016). This is what we consider to be an adjusted wind response, and hereafter we refer to the 3-month WWV hindcasts (orange circle, Fig. 2.1b) as the adjusted WWV contribution. This adjusted WWV contribution is largely consistent with the dynamics considered by the RDO theory (Jin, 1997) and the delayed-oscillator theory (Suarez and Schopf, 1988). We also introduce the seasonal change here (dashed red line, Fig. 2.1b), which is the change of the hindcast WWV during the model's free evolution (how the WWV has evolved from the control simulation of a particular period to the 3-month hindcast extending from that period; Fig. 2.1b).

Instantaneous WWV: The instantaneous WWV response builds due to the winds prevailing in the control simulation that are not incorporated in the free evolution of the adjusted WWV contribution during the same period. The instantaneous WWV contribution is therefore obtained by taking the difference between the control WWV and the adjusted WWV contribution (blue arrow, Fig. 2.1b). It is consistent with WWV changes induced by Ekman transports (cor=0.9, Fig. A2.2).

If stated not differently, all correlations are significant at the 95% confidence level based on Ebisuzaki's (1997) method for autocorrelated time series. Temporal smoothing, where discussed, was carried out with a 3-month running mean. All SWM-data needed for calculations in this study are provided in tables S2-S8 in Neske and McGregor (2018).

2.3 Results

In order to understand the drivers of: (i) WWV change during the oceans free evolution to its adjusted WWV state (i.e., its seasonal change, see Fig. 2.1b); and (ii) how the instantaneous WWV contribution is built; the seasonal change and the instantaneous contribution are plotted against the western/central Pacific (150°E-160°W, 5°N-5°S) zonal wind stress anomalies (Fig. 2.2). The western/central Pacific region is selected as the coupling between ocean and atmosphere is largest here (Deser and Wallace, 1990) and wind events in this region have the largest instantaneous and adjusted WWV response (McGregor et al., 2016). The seasonal WWV change is strongly negatively correlated (cor=-0.86, Fig. 2.2a) to the average wind stress two months prior to the free evolution period (i.e., 3-4 months prior to the adjusted month; see "winds before" in Fig. 2.1b), while the instantaneous contribution has a strong positive correlation (cor=0.82, Fig. 2.2b) to the average wind stress during the evolution (i.e., the month prior to and the month of the adjusted contribution, see "winds during", Fig. 2.1b).

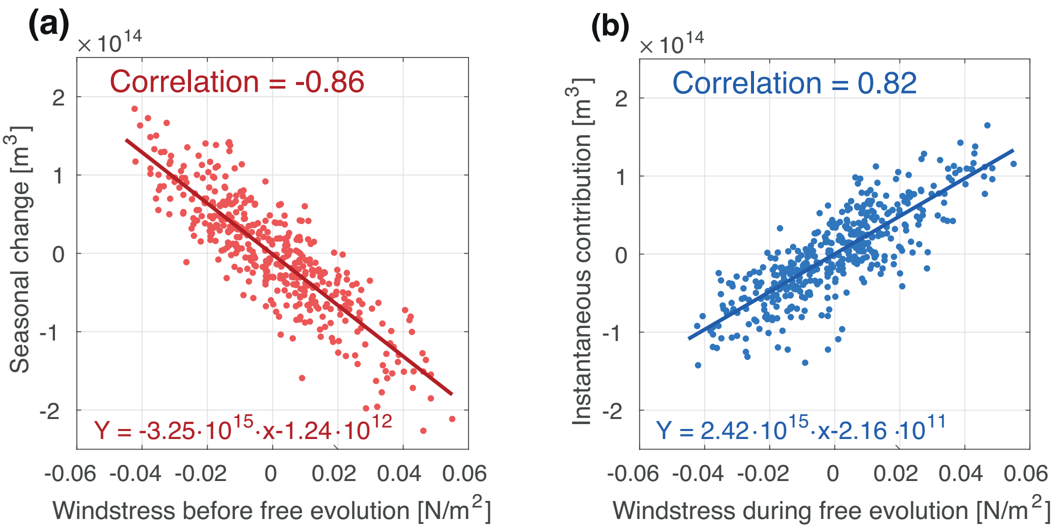

Figure 2.2: **(a)** Seasonal WWV change [m^3] plotted against the western/central Pacific (150°E-160°W, 5°N-5°S) zonal wind stress [N/m^2] averaged over the two months prior to the free evolution ("winds before" in Fig. 2.1b) (1980-2016). **(b)** The instantaneous WWV contribution [m^3] plotted against the western/central Pacific (150°E-160°W, 5°N-5°S) wind stress [N/m^2] averaged over the two last months of the hindcast runs ("winds during" in Fig. 2.1b) (1980-2016).

These findings are consistent with wave theory (e.g. summarized by Clarke, 2008) and the idealized experiments of McGregor et al. (2016), in which an equatorial westerly wind burst leads to: (i) an instantaneous WWV recharge through Ekman transport and the generation of downwelling Kelvin waves in the WWV region; and (ii) an adjusted discharge (negative seasonal change) through the delayed effect of the majority of the Kelvin wave signal leaving the WWV region at the eastern boundary and the western boundary reflection of the associated upwelling Rossby waves into the WWV region after around 1-2 months. As expected, the 3-month hindcast has its highest (lowest) correlation (RMSE) to the control simulation at a 0-month lag, while for higher months hindcasts the highest (lowest) correlation (RMSE) to the control simulation is shifted to longer lag times (Fig. A2.1). This suggests that longer lead time hindcasts are mainly the decayed version of the 3-month hindcast with an additional time lag, which emphasizes the usefulness of taking the 3-month hindcast to split the control WWV into the two parts. These results justify our definition of the adjusted and instantaneous WWV contributions and suggest that the experiment design allows to separate these two components for the first time.

The WWV decomposition shows that the adjusted WWV contribution does a reasonable job producing the control simulation WWV (cor=0.81; Fig. 2.1c). Secondly, it is also clear that approximately half of the control WWV signal does not rely on the adjusted WWV contribution, rather it is changed through the instantaneous WWV contribution (cor=0.75; Fig. 2.1c), which is further supported by the similar standard deviations (STDs) of the adjusted contribution (STD=$5.73 \cdot 10^{13}$ m^3) and the instantaneous contribution (STD=$5.14 \cdot 10^{13}$ m^3). Considering the recharged and discharged periods separately (defined as positive and negative values of the control simulation respectively), a clear asymmetry is identified as the discharged periods are dominated by the adjusted contribution (purple dots in Fig. 2.3a, cor=0.8 and B=0.72), while the recharged periods are dominated by the instantaneous contribution (gray dots in Fig. 2.3d, cor=0.67 and B=0.68).

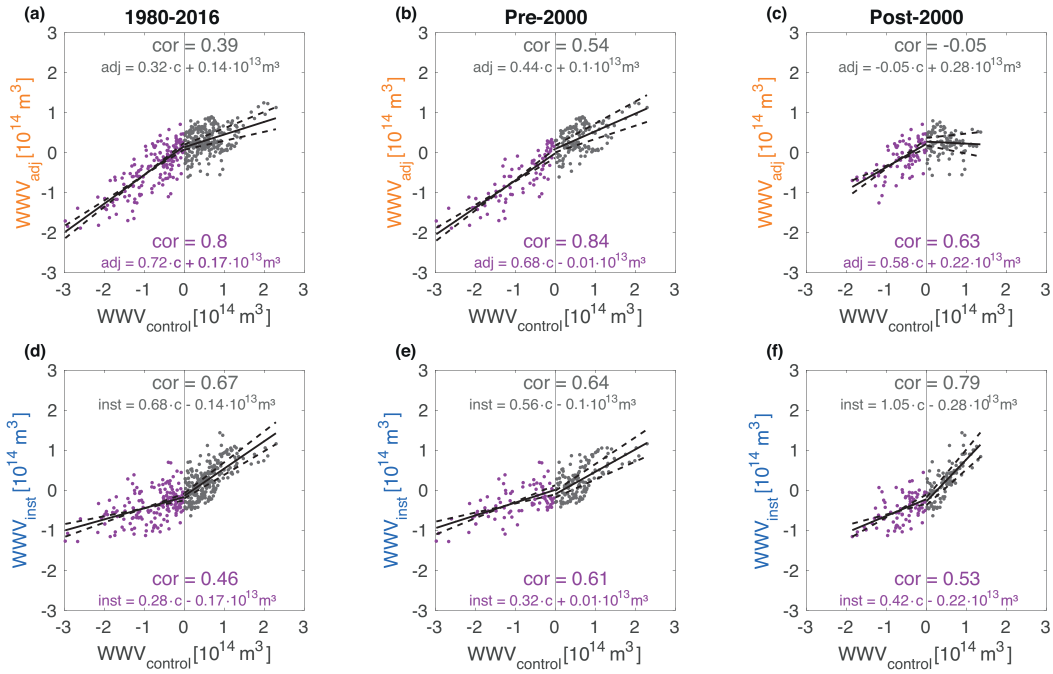

Figure 2.3: Smoothed adjusted WWV contribution plotted against the control simulation WWV for the periods **(a)** 1980-2016, **(b)** 1980-1999 and **(c)** 2000-2016. **(d)**, **(e)** and **(f)** show the same time periods as above plots, but display the instantaneous WWV contribution plotted against the control simulation WWV. Correlations and linear regression equations of the positive (negative) values of the control simulation and their related values of the adjusted and instantaneous contributions are in gray (purple). Dashed lines give the 95% confident interval of the fitted slopes.

2.3.1 Pre- and post-2000 differences

As noted by McPhaden (2012) and Horii et al. (2012), the Pacific Ocean has displayed some distinct changes since the year 2000, so it makes sense to assess these two periods separately. The most obvious of these pre- to post-2000 changes is a 30% reduction in the STD of the control simulation WWV signal which can be seen in Fig. 2.1a and c (black line) (e.g. Hu et al., 2017).

Focusing on the pre-2000 period in Fig. 2.1c, the STD of the instantaneous WWV contribution is $4.79 \cdot 10^{13}\ m^3$ and its correlation to the control WWV is 0.75 (see also Table A2.1). The STD of the adjusted WWV contribution is around 40% larger ($6.88 \cdot 10^{13}\ m^3$) and its correlation to the control WWV (0.88) is around 15% larger. The magnitude of the STDs and correlations highlights that both the instantaneous and the adjusted response are important contributors to the pre-2000 control WWV, however, the adjusted response plays the more prominent role during this period.

On the other hand, the STD of the adjusted WWV contribution during the post-2000 period ($3.86 \cdot 10^{13}$ m^3) is around 44% lower than its pre-2000 value, while its correlation to the control simulation WWV is reduced to 0.6. The STD of the instantaneous WWV contribution during this latter period ($5.49 \cdot 10^{13}$ m^3) is slightly larger (around 14%) than its pre-2000 value, while the post-2000 correlation of this signal to the control simulation WVV is also slightly higher (cor=0.82). Consequently, the reduction of the STD of the control simulation WWV from the pre-2000 period to the post-2000 period can be attributed to the reduction of the adjusted WWV contribution. This also has the added effect of leaving the instantaneous WWV contribution as the dominant WWV contributor during the post-2000 period.

When repeating the hindcast experiments with JRA-55, NCEP-I and NCEP-II wind products (see Text A2.2 for details about the wind products) the results produced are consistent with those of the ERA-interim hindcasts. That is: (i) a post-2000 reduction of adjusted WWV is identified in every experiment (Fig. A2.3a); and (ii) the post-2000 dominance of the instantaneous WWV contribution for the JRA-55 and NCEP-II simulations (Fig. A2.3b). It is noted, however, that the control WWVs produced by the ERA-interim forced simulation (used for this study) produce the most to observed WWV (cor = 0.85, Fig.A2.4a), followed closely by the JRA-55 forced simulation (cor = 0.82, Fig. A2.4b). In contrast, the WWVs of the NCEP-I and NCEP-II forced simulations are less consistent with the observed WWV (cor $\leq$ 0.7, Fig. A2.4c and d).

The largest pre- and post-2000 difference is seen during recharged periods which are significantly correlated to the adjusted contribution during the pre-2000 period (cor=0.54; B=0.44; gray dots, Fig. 2.3b), while the recharged periods are not significantly correlated to the adjusted contribution during the post-2000 period (gray dots, Fig. 2.3c). Thus, suggesting that the post-2000 recharged periods can almost be solely explained by the instantaneous response to westerly winds. This is further supported by the post-2000 increase in regression slope (pre-2000 B=0.56; post-2000 B=1.05) and correlation (pre-2000 cor=0.64; post-2000 cor=0.79) between the instantaneous and control simulation WWVs recharged periods (gray dots, Fig. 2.3e and f).

Pre- and post-2000 differences seen during discharged periods are relatively small in comparison to the recharged periods. The discharged period of the pre-2000 period is strongly correlated to the adjusted response (cor=0.84; B=0.68; Fig. 2.3b purple dots), the correlation reduces to 0.63 (but still significant) and the regression slope to 0.58 (purple dots, Fig. 2.3c). The pre-2000 correlation and regression slope indicate that the discharged period is less strongly influenced by the instantaneous response (cor=0.61; B=0.32; purple dots, Fig. 2.3e), and this remains during the post-2000 period (cor=0.53; B=0.42; purple dots, Fig. 2.3f).

Combined, these results allow us to conclude that the dominance of the instantaneous WWV response over the adjusted WWV response in the post-2000 period is almost purely manifested during the recharged periods.

The consequence of the changes in the balance of the adjusted vs. instantaneous WWV contributions from pre- to post-2000 period is highlighted in their lead/lag correlations with observed ENSO (Niño 3.4, available at http://www.cpc.ncep.noaa.gov/data/indices/) SST (Fig. 2.4). For the pre-2000 period the control simulation WWV leads ENSO SST with a maximum correlation of 0.68 occurring with a 6-month lead time (black line, Fig. 2.4a), while the post-2000 maximum correlation of 0.70 occurs with a 3-month lead time (black line, Fig. 2.4b).

The instantaneous WWV contribution reveals similar ENSO SST peak correlations for the pre- (cor=0.75) and post-2000 (cor=0.8) periods at lead times of 2 months (blue line in Fig. 2.4a and b). The adjusted WWV contribution, however, reveals ENSO SST peak correlations of 0.62 at 9 months for the pre-2000 period (orange line, Fig. 2.4a), while no significant peak is apparent at any lead time in the post-2000 period (orange line, Fig. 2.4b). Thus, the lack of a clear adjusted WWV

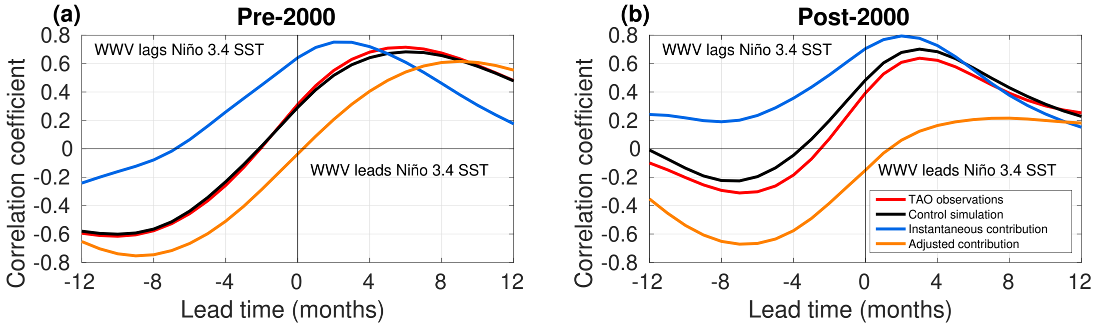

Figure 2.4: **(a)** Cross correlation of monthly mean Niño 3.4 SST and WWV from the (i) observations (red line), (ii) control simulation (black line), (iii) instantaneous contribution (blue line) and (iv) adjusted contribution (orange line) for 1982-1999. **(b)** Same as in **(a)** but for 2000-2016.

contribution correlation during the post-2000 period has acted to: (i) enhance the similarity of the instantaneous WWV and ENSO SST lead correlations with those of the control WWV and ENSO SST; and, (ii) reduce the WWV lead time prior to the event (compare blue and black line in Fig. 2.4b).

Additionally, focusing on the WWV and ENSO SST lagged minimum correlations, clear differences are apparent between the pre- and post-2000 periods. For the pre-2000 period, the control simulation lagged correlation to ENSO SST displays a minimum correlation (cor=-0.6) at -10 months (black line, Fig. 2.4a). This largely resembles the lagged correlations of the adjusted WWV contribution (cor=-0.75 at -9 months lag; orange line, Fig. 2.4a), but is clearly offset towards more positive values due to the addition of the instantaneous contribution. The post-2000 control simulation lagged correlation displays a minimum correlation (cor=-0.23) at -7 months, which is not significant (black line, Fig. 2.4b). Again, the timing of this lagged negative correlation largely resembles the lagged correlations of the adjusted WWV contribution (cor=-0.67 at -7 months lag; orange line, Fig. 2.4b). While this is similar to the pre-2000 period, the instantaneous contribution in the post-2000 period leads to a much larger offset towards positive values, such that the recharge (discharge) of control WWV following a negative (positive) Niño 3.4 SST anomaly is almost non-existent in this post-2000 period.

2.4 Discussion and Conclusion

This paper sought to explain and better understand the mechanisms that underlay the predictability of ENSO by decomposing the equatorial Pacific WWV into its instantaneous and adjusted responses. The adjusted response was defined as the averaged third month outcome of a wind-forced SWM that is left to evolve unforced for three months (after any wind-excited Kelvin wave has reached the eastern boundary); while the instantaneous response was defined as the difference between the wind-forced (control) simulation and the adjusted response at the same time which is consistent with WWV changes due to Ekman transports (Fig. A2.2). Both responses can either recharge or discharge WWV prior to ENSO events, what differs between them is how predictable the oceanic response is (the adjusted response is predictable at least 3 months in advance while the instantaneous is only as predictable as the winds themselves) (Fig. 2.2). This decomposition was carried out in order to (1) get a better understanding of the dynamics and predictability of ENSO events; and (2) provide insight into the mechanisms underlying the post-2000 reduction in the WWV/ENSO SST lead times.

It was clear that during the 1980-2016 period, a little more than half of the control WWV signal relies on the adjusted contribution, while the remaining portion is changed due to the instantaneous contribution (Fig. 2.1c). The existence of this large instantaneous contribution raises serious questions about the dominance of the RDO (Jin, 1997) and delayed-oscillator (Suarez and Schopf, 1988) theories and the notion of ENSO being a self-sustained cycle. These questions are further supported by the fact that the recharge process prior to an El Niño event is dominated by the instantaneous contribution while the discharge process appears to be dominated by the adjusted contribution (Fig. 2.3 and Fig. A2.5). Both of which are consistent with Kessler (2002) who shows that ENSOs oscillatory behavior can pause for a longer time in a weakly recharged weak La Niña state (between 1980-2002) before being reinvigorated for another cycle by recharging, while our study highlights that the reinvigoration is due to the instantaneous WWV response. This suggests that the lead time for accurate forecasts may be longer for La Niña events than for El Niño events. It is important to note, however, that while our results raise questions over the dominance of the oscillatory view of ENSO and provides support for viewing ENSO as event like disturbance (e.g. Thompson and Battisti, 2001, Kessler, 2002), it is clear that both the self-sustained cyclic and event-like views of ENSO are reasonable and what actually happens is a balance of the two.

Changes to the balance of adjusted vs. instantaneous contributions become apparent when analyzing pre- and post-2000 periods separately. For the pre-2000 period we found that both, the adjusted and the instantaneous contributions are important to explain the WWV vs. ENSO SST lead of 6-9 months. The lead/lag correlations of control WWV to ENSO SST throughout this period (Fig. 2.4a) support both: an oscillatory view of ENSO (e.g. Jin, 1997, Suarez and Schopf, 1988), where event precursor WWV changes are due to the adjusted responses of preceding events of the opposite sign; and the event-like view where the event triggering wind instantaneously recharges or discharges WWV (e.g. Thompson and Battisti, 2001).

We also found that the instantaneous WWV contribution is dominant during the post-2000 period, which is consistent with the post-2000 increase of the influence of the tilt-mode in explaining WWV changes (Bunge and Clarke, 2014), and which reduces the oscillatory nature of ENSO as the weaker adjusted post event WWV changes are overpowered by the instantaneous contribution (Fig. 2.4b). Furthermore, the reduced influence of adjusted WWV contributions during this period explains the observed shortening of WWV vs. ENSO SST lead time to 2-3 months (Fig. 2.4, McPhaden, 2012, Horii et al., 2012, Bunge and Clarke, 2014). The post-2000 reduced adjusted WWV contribution and the post-2000 dominance of the instantaneous WWV contribution are also found when repeating these experiments and analysis with the JRA-55 and NCEP-II wind products (see Fig. A2.3). Further, this reduced adjusted WWV contribution influence was most prominently found in the recharge phase, which leaves the instantaneous WWV contribution almost solely responsible for the recharge phase (Fig. 2.3c and f). Thus, our results suggest that during the post-2000 period the instantaneous WWV recharge, associated with westerly wind bursts, is largely responsible for the pre-El Niño event recharge. These are the same events that previous studies highlight to trigger the ENSO events themselves (e.g. Harrison and Vecchi, 1997), which can also help to explain the lowering in predictable skill of ENSO for the post-2000 period (e.g. Wang et al., 2010, Barnston et al., 2012, Kumar et al., 2015).

The two questions raised by this study are: (1) What causes the recharge process being dominated by the instantaneous response and the discharge process being dominated by the adjusted response; and (2) why has the adjusted WWV response changed in the post-2000 period, while the instantaneous WWV response has not, given both responses are forced by the same wind events. This might be due to: (i) changes to the structure of wind events between these two periods (Harrison and Chiodi, 2009), or (ii) the post-2000 westward shift of the Bjerknes feedback region (Bunge and Clarke, 2014, Hu et al., 2017). Additionally, we speculate that off-equatorial winds (between 5°N-15°N and 5°S-15°S), which have a large instantaneous WWV contribution and a much smaller adjusted response (McGregor et al., 2016), play a crucial role in answering this question.

Appendix Chapter 2

Text A2.1

The linear 1.5-layer shallow water model (SWM) used for the experiments in this study is a reduced gravity model of the stratified ocean (see equations below), with a $1° \cdot 1°$ spatial resolution, discretized on an Arakawa C grid, and configured for the global ocean between 51°N and 51°S. A leapfrog time stepping scheme is applied and the model time step is 2 h. The active upper layer (mean depth of H=300 m) is driven by wind stresses and is separated from the lower motionless, infinitely deep layer by a sharp tropical pycnocline, which approximates the thermocline in the tropical Pacific region (Rebert et al., 1985). The SWM follows the linear reduced-gravity form of the shallow water equations:

$$\frac{\partial u}{\partial t} - fv + g' \frac{\partial \eta}{\partial x} = \frac{\tau^x}{\rho H}; \tag{A2.1}$$

$$\frac{\partial v}{\partial t} + fu + g' \frac{\partial \eta}{\partial y} = \frac{\tau^y}{\rho H}; \tag{A2.2}$$

$$g' \frac{\partial \eta}{\partial t} + c_1^2 (\frac{\partial u}{\partial x} + \frac{\partial v}{\partial y}); \tag{A2.3}$$

where u and v are the zonal and meridional velocity anomalies, t is the time, f is the Coriolis parameter, ρ=1000 kg/m^3 is the density of the upper layer, g'=0.03 m/s^2 is the reduced gravity, reflecting the density difference between the upper and the lower layer, η gives the displacement of the pycnocline, c_1 is the first baroclinic mode Kelvin wave speed and τ^x and τ^y are the zonal and meridional components of the wind stress forcing anomalies. The wind stress is calculated using the quadratic stress law: $(\tau^x, \tau^y) = \rho_a C_d (U_{10}, V_{10}) \sqrt{(U_{10}^2 + V_{10}^2)}$, with ρ_a=1.2 kg/m^3 being the air density, $C_d = 1.5 \cdot 10^{-3}$ being a dimensionless drag coefficient and U_{10} and V_{10} being the zonal and meridional winds at 10 m height. To calculate the wind stress, the

6-hourly ECMWF Reanalysis (ERA-Interim Dee and Uppala, 2009) dataset is used, averaged to a daily output and subtracted by the long-term seasonal cycle.

Text A2.2

The comparison of reanalysis wind products usually used for ENSO studies reveals substantial discrepancies in variability and trends (e.g. McGregor et al. 2012a, Chiodi and Harrison, 2017). Thus, we compare the produced adjusted, instantaneous and control WWVs of the ERA-interim wind stress simulations (which are used for this study) and the produced WWVs of simulations of three additional reanalysis wind products (Fig. A2.3 and Fig. A2.4): (i) the Japanese 55-year Reanalysis wind product (JRA-55, Kobayashi et al., 2015), (ii) the NCEP–NCAR Reanalysis-1 wind product (NCEP-I, Kalnay et al., 1996), and (iii) the NCEP–DOE Reanalysis-2 wind product (NCEP-II, Kanamitsu et al., 2002). Consistently to the ERA-interim simulations, u- and v- 10 m wind velocities are available 4 times daily for every additional wind product, and daily wind stress anomalies are calculated according to Text A2.1. What differs among the different wind products is the: (i) assimilation method, (ii) observed data used, and (iii) grid which has a spatial resolution of: 0.75° for the ERA-interim product, 1.25° for the JRA-55 product, and 1.875° for both the NCEP-I and NCEP-II products. It is noted that the discussion about WWVs produced by different wind products is not part of the publication "Neske and McGregor (2018)" which makes up the majority of Chapter 2, but it evolved during the review process of this dissertation.

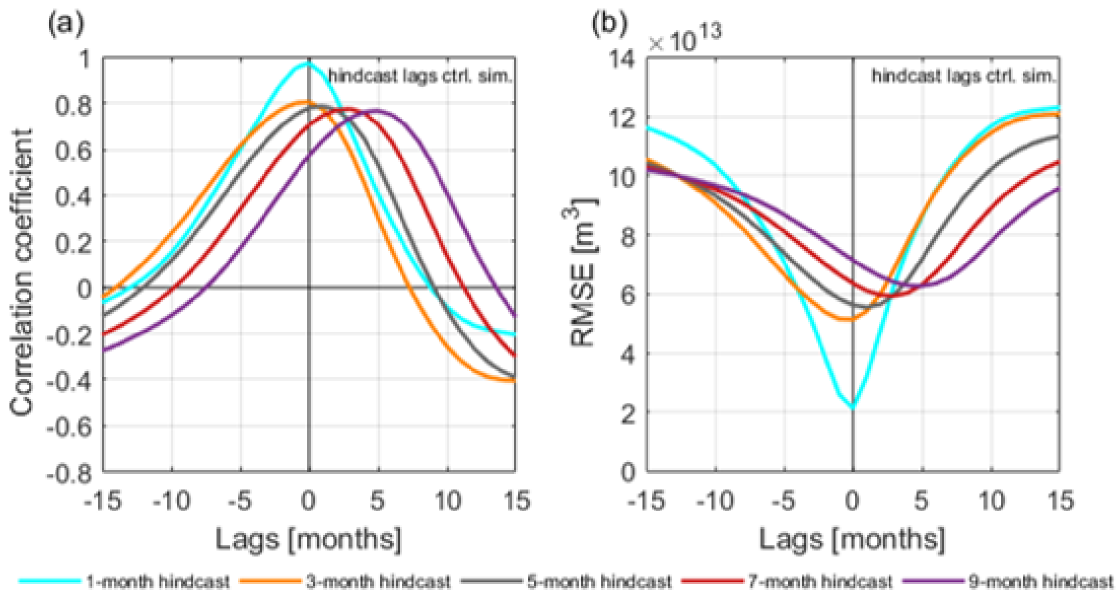

Figure A2.1: **(a)** Cross-correlation of the smoothed (3-month running mean) control simulation WWV and the smoothed 1-,3-,5-,7- and 9-month hindcast WWV between 1980-2016. **(b)** RMSE $[m^3]$ between the smoothed 1-,3-,5-,7- and 9-month hindcast WWV and the smoothed control simulation WWV.

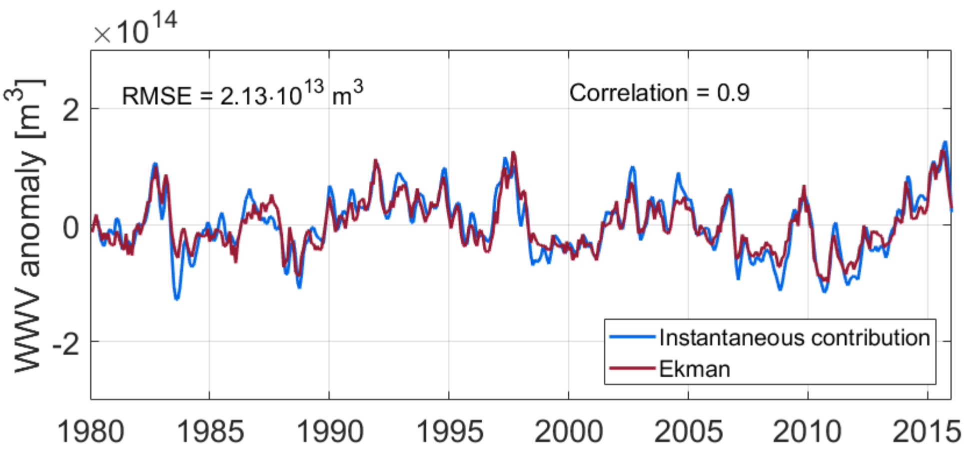

Figure A2.2: Smoothed (3-month running mean) WWV anomaly due to (i) the instantaneous contribution $[m^3]$ (blue line), and (ii) the meridional Ekman transport anomalies entering the WWV box at the meridional boundaries (5°N and 5°S) $[m^3]$ (red line). Ekman transport anomalies were calculated according to $V_{ek} = \frac{-\tau^x}{\rho f}$, with τ^x being the zonal wind stress anomalies (same as the zonal model wind stress forcing), ρ is the upper ocean density taken as constant (1023 kg/m^3) and f is the Coriolis parameter. The meridional transports were integrated over 120°E-80°W at 5°N and over 150°E-80°W at 5°S (to exclude the area over land).

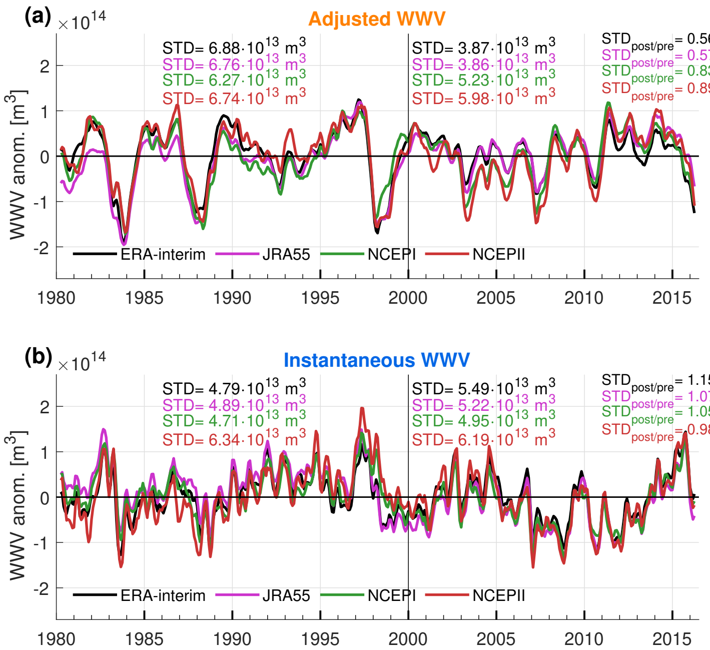

Figure A2.3: Smoothed time series of the **(a)** adjusted and **(b)** instantaneous WWV contributions $[m^3]$ conducted by hindcast experiments as described in Section 2.2 forced by wind stresses derived from ERA-interim (black line), JRA-55 (magenta line), NCEP-I (green line), and NCEP-II (red line) data sets.

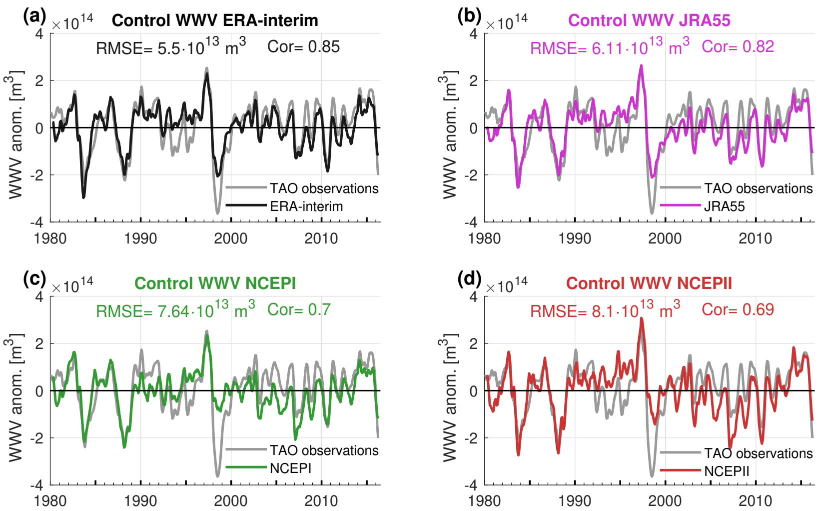

Figure A2.4: Smoothed time series of the control WWV contributions $[m^3]$ obtained by SWM experiments as described in Section 2.2 forced by wind stresses derived from **(a)** ERA-interim, **(b)** JRA-55, **(c)** NCEP-I, and **(d)** NCEP-II data sets.

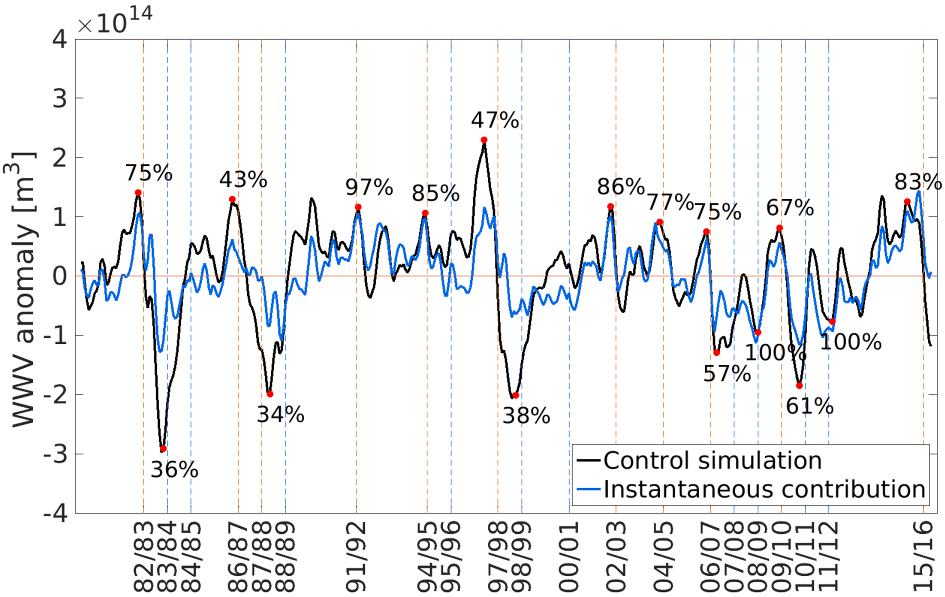

Figure A2.5: Smoothed WWV of the control simulation [m^3] (black line) and instantaneous contribution [m^3] (blue line) between 1980-2016. Percentage values describe the proportion of control simulation WWV peaks/troughs (red dots) preceding ENSO events (averaged for the five months around) which is explained by the instantaneous WWV contribution. The El Niño (La Niña) years are marked by the vertical dashed red (blue) lines. ENSO events are defined following the National Oceanic and Atmospheric Administration (NOAA) thresholds and the closest preceding WWV peaks/troughs for El Niño/La Niña events are considered. When multiple events occur in a row and these events have only one clear WWV peak/trough, only this WWV peak/trough is considered (e.g., the 1986/87 and 1987/88 El Niño, the 1983/84 and 1984/85 La Niña and the 1998/99 and 2000/01 La Niña). The WWV preceding the 1995/96 La Niña does not show a clear discharge in the control simulation so it is also excluded from this analysis.

Table A2.1: Pre-2000 (1980-1999)- and post-2000 (2000-2016) (i) standard deviation (STD) of the smoothed instantaneous and adjusted contributions, and (ii) correlation of the smoothed instantaneous and adjusted contributions to the smoothed control simulation.

	Instantaneous contribution	**Adjusted contribution**
STD pre-2000 [10^{13} m^3]	4.79	6.88
STD post-2000 [10^{13} m^3]	5.49	3.86
Correlation to control simulation pre-2000	0.75	0.88
Correlation to control simulation post-2000	0.82	0.6

Chapter 3

Wind spatial structure underpins ENSO's oceanic warm water volume changes

Preface

This study demonstrates that the generalization that strong anomalous equatorial Pacific westerly (easterly) wind stress during El Niño (La Niña) events display strong adjusted warm water volume (WWV) discharges (recharges) is often incorrect. Using ocean model simulations, we categorize the oceanic adjusted responses to strong anomalous equatorial winds into three categories: (i) transitioning (consistent with the above generalization); (ii) neutral; and (iii) persistent adjusted responses. During the entire 1980-2016 period only 35% of strong anomalous equatorial winds are followed by transitioning adjusted responses, while the remaining are followed by neutral (56%) or persistent (9%) adjusted responses. Moreover, 75% of the winds with transitioning adjusted responses are found during the pre-2000 period in agreement with the previously reported post-2000 decline of WWV lead time to El Niño-Southern Oscillation (ENSO) events. The prominent neutral adjusted WWV response is shown to be largely excited by anomalous wind stress forcing with a weaker curl (consistent with a higher ratio of off-equatorial to equatorial wind events) and weaker Rossby wave projection than the transitioning adjusted response. We also identify a prominent ENSO phase asymmetry where strong anomalous equatorial westerly winds (i.e., El Niño events) are roughly twice as likely to strongly discharge WWV than strong anomalous equatorial easterly winds (i.e., La Niña events) are to strongly recharge WWV. This ENSO phase asymmetry may be added to the list of mechanisms proposed to explain why El Niño events have a stronger tendency to be followed by La Niña events than vice versa.

3.1 Introduction

The tropical Pacific region provides the unique conditions for the largest inter-annual climate fluctuation on our planet: the El Niño Southern-Oscillation (ENSO). ENSO describes a coupled atmospheric-ocean phenomenon occurring every 2 to 7 years. It fluctuates between (i) anomalous warm states of equatorial eastern Pacific sea surface temperature (SST) accompanied by a weakening or a reversal of trade winds (El Niño), and (ii) anomalous cool states of equatorial eastern Pacific SST accompanied by a strengthening of trade winds (La Niña). Around four decades of intense research has tremendously enhanced our understanding of ENSO (e.g. Timmermann et al., 2018), however, we still have difficulties in unscrambling the subtleties of ENSO dynamics, and precisely predicting the ENSO state (e.g. Timmermann et al., 2018, Santoso et al., 2019). Enhancing the predictability of ENSO, which is expected to be partially reliant of enhancing our understanding of its dynamics, is sought after as the events are responsible for severe weather events and climatic conditions that affect societies around the globe (e.g. Williams and Karoly, 1999, Diaz et al., 2001, McPhaden et al., 2006, Sarachik and Cane, 2010, Werner and Holbrook, 2011, Loughran et al., 2017). Furthermore, CMIP5 models indicate a strengthening of these severe climatic events connected to ENSO under future climate change scenarios (Power et al., 2013, Cai et al., 2015, Perry et al., 2017, Power and Delage, 2018).

Traditional conceptual models of ENSO, which were developed in the 1980s-1990s, are milestones in ENSO research that highlight our understanding of this phenomenon by summarizing its important mechanisms and feedbacks (Suarez and Schopf, 1988, Weisberg and Wang, 1997, Picaut et al., 1997, Jin, 1997). A summary of these traditional conceptual models is provided by Wang (2001) and Wang and Picaut (2004). These models are based on several ordinary differential equations that solve for the eastern Pacific's SST and they describe ENSO as a self-sustained oscillation. In each of these models the growth of ENSO events is underpinned by the Bjerknes feedback (Bjerknes, 1969), in which westerly (easterly) wind anomalies are generated due to the eastward extension (westward contraction) of the equatorial warm pool and its related shifts in anomalous deep convection that act to reinforce the original anomalously warm (cool) SSTs. However, each model suggests that different negative feedbacks are responsible for the end of the events, and due to the numerous assumptions and approximations, none of these conceptual models can fully describe ENSO's complexity.

A leading paradigm for ENSO's apparent oscillatory behavior is Jin's (1997) recharge-discharge oscillator (RDO) theory. According to this theory, during El Niño (La Niña) events, the Bjerknes feedback (Bjerknes, 1969) causes equatorial westerly (easterly) wind anomalies and positive (negative) eastern equatorial Pacific SST anomalies to reinforce each other, at the same time as the oceanic adjustment to the westerly (easterly) wind anomalies acts to discharge (recharge) equatorial upper ocean heat content, conditioning the system for a change in phase of ENSO. The main ideas of Jin's (1997) theory have been confirmed by observational studies showing that the warm water volume (WWV, which is the thermocline depth integrated over the region 120-280°E and 5°N-5°S), a variable describing the upper ocean heat content, is leading ENSO SST by 1-3 seasons (Meinen and McPhaden, 2000, 2001, McPhaden, 2012, Bunge and Clarke, 2014). Consequently, the WWV has been manifested as being viewed as a precursor to ENSO events, and is largely thought to underlie its predictability.

Some aspects of ENSO, however, are not be explained by the RDO theory such as: (i) the asymmetry between the magnitude of the WWV recharge preceding El Niño events compared to the magnitude of WWV discharge preceding La Niña events (Meinen and McPhaden, 2000, Clarke and Zhang, 2019); (ii) the asymmetry in duration and phase change transition with El Niño events lasting a shorter period and having a stronger tendency to be followed by La Niña events than vice versa (e.g. Kessler, 2002, Larkin and Harrison, 2002, Okumura and Deser, 2010, Guan et al., 2019, Clarke and Zhang, 2019); (iii) the decrease observed in WWV/ENSO SST lead time from around three seasons in the 1980's and 1990's to only one season during the post-2000 period (McPhaden, 2012, Horii et al., 2012, Bunge and Clarke, 2014); and (iv) the existence of different ENSO types: Central Pacific (CP, with maximum SST anomaly found in the central equatorial Pacific) vs. Eastern Pacific (EP, with maximum SST anomaly found in the eastern equatorial Pacific) ENSO events (e.g. Kao and Yu, 2009, McPhaden et al., 2011, Singh and Delcroix, 2013). Moreover, the RDO theory considers only the adjusted oceanic response, which occurs via Rossby wave (RW) reflection at the western boundary, while wind-forced Kelvin waves (KWs, not considered in the RDO theory) have also been shown to provide important short time scale (around 1-3 months) contributions to observed WWV changes determining ENSO event initiation and/or evolution (Weisberg and Wang, 1997, McPhaden and Yu, 1999, Boulanger et al., 2003, Bosc and Delcroix, 2008, McGregor et al., 2016, Neske and McGregor, 2018, Izumo et al., 2019).

Several studies have attempted to separate the WWV anomaly into its slower RW and faster KW components using various methods (Meinen and McPhaden, 2000, Neske and McGregor, 2018, Planton et al., 2018, Izumo et al., 2019). This partitioning allows more insight into ENSO dynamics, that is not possible when considering the WWV anomaly as a whole. For example, Neske and McGregor (2018) demonstrate that the post-2000 WWV STD (standard deviation) decline is due to a 44% decline of post-2000 RW driven (hereafter, *adjusted*) WWV STD, and in this post-2000 period the reduced adjusted contribution fails to work as a precursor for ENSO. (see Chapter 2). Consequently, Neske and McGregor (2018) show that the dominance of the KW driven (hereafter, *instantaneous*) WWV in the post-2000 period is responsible for the shortening of WWV/ENSO SST lead time reported by McPhaden (2012).

It is currently not understood, however, why the STD of the adjusted component of WWV decreased by around 44% from pre- to post-2000 period, when over the same time period, the STD of the instantaneous component of WWV increased by around 15% (Neske and McGregor, 2018, Chapter 2). Traditional ENSO theories assume that the strength of the anomalous equatorial westerly (easterly) winds was directly related to the strength of the upwelling (downwelling) RWs and its associated following WWV discharge (recharge) (Suarez and Schopf, 1988, Jin, 1997, Wang and Picaut, 2004). Thus, we would expect that the post-2000 strengthening in the instantaneous contribution's STD associated with a strengthening in equatorial winds' STD would lead to a strengthening in the adjusted response STD as well and not to a decline in the adjusted response STD as found by Neske and McGregor (2018) (Chapter 2).

What is not considered in most of the literature, and we propose may be key in explaining the post-2000 adjusted WWV decline, is the possible independence of the wind stress curl from the strength of equatorial wind stress. The wind stress curl around the equatorial region: (i) changes due to the spatial structure and central latitude of the wind events; and (ii) determines the strength and sign of the RWs through Ekman Pumping (e.g. Tomczak and Godfrey, 2013). McGregor et al. (2016) show for instance, that the same amount of instantaneous WWV recharge leads to a lower adjusted response for off-equatorial wind events than for equatorial wind events as both produce a different wind stress curl around the WWV region.

An emphasis on considering wind stress curl for ENSO dynamics was given by Clarke et al. (2007). They theoretically derived WWV changes by wind stress curl at 5° latitude which has a correlation of 0.85 to observed WWV changes between 1993-2001. However, when later developing his conceptual model of ENSO, Clarke et al. (2007) instead utilizes the relationship between wind stress curl derived WWV and Niño3.4 SST (correlation=0.77), rather than wind stress curl itself. Thus, the developed conceptual model leaves out the possibility of strong equatorial wind stresses during ENSO events with weak wind stress curls around the bounds of the WWV region. While this may not be essential for ENSO to operate, it may help to explain both, the relatively subtle pre- to post-2000 changes in the WWV-ENSO SSTA relationship as well as ENSO asymmetries.

This Chapter therefore aims to understand to what extent the spatial structure of strong westerly (easterly) equatorial wind stresses in the 1980-2016 period can influence the adjusted contribution. Given that the adjusted contribution is thought to underpin the ENSO predictability on lead times of around 1 year (Neske and McGregor, 2018, Chapter 2) our analysis further deepens our understanding of possibilities and limits of ENSO predictability.

This Chapter is organized as follows: Section 3.2 provides a description of methods and data. Section 3.3 classifies the adjusted responses following the strongest equatorial wind stresses into 3 different categories. We then analyze (i) the differences of the wind composites according to their category (Section 3.4), and (ii) the WWV impact of the composite winds (Section 3.5). The links between composite average winds and single wind events within the composite are then examined in Section 3.6. Moreover, we examine the relationship between the adjusted responses of the categorized winds and their reliability as an ENSO precursor (Section 3.7). Finally, we summarize and discuss the results (Section 3.8).

3.2 Methods and Data

3.2.1 Wind stress and SST data

Wind stress data

For our analysis, we use daily average anomalous surface wind stresses (1979 to May 2016) of the European Centre of Medium-Range Weather Forecast (ERA-interim) (Dee and Uppala, 2009). The stresses were generated from the 6-hourly 10 m surface winds which were first converted to wind stress using the quadratic stress law, and then averaged to a daily output, prior to the long-term seasonal cycle being removed.

We further define the wind stress time series averaged over the equatorial region, 120-280°E and 5°N-5°S as τ_{xeq}.

SST data

Additionally, we use the spatial ERSST.v5 data set between 1979-2016 (Smith et al., 2008, available at https://www1.ncdc.noaa.gov/pub/data/cmb/ersst/v5/netcdf/).

From this data set the Niño 3.4 SSTA time series is calculated by averaging over 5°N-5°and 170-240°E.

3.2.2 Shallow water model simulations

Here, as in Chapter 2 (Neske and McGregor, 2018), a 1.5-layer shallow water anomaly model (SWM) is utilized to split the WWV into its instantaneous and adjusted contributions. The SWM has a 1° horizontal grid spacing for forcing and output, and it is forced with daily wind stress anomalies. It produces daily pycnocline depth anomalies which are integrated over the WWV region (120-280°E and 5°N-5°S) to obtain WWV anomalies. Further details about the SWM can be found in Appendix Chapter 2 Text A2.1, or Neske and McGregor (2018, their Text S1).

The separation of the adjusted and instantaneous WWV contributions in the SWM is done by conducting hindcast experiments initialized on the first day of each month between January 1980 and March 2016 (as illustrated in Fig. 3.1a). Each of these hindcasts have a wind stress forced spin up of one year, before the SWM is being left to freely evolve unforced (turquoise line, Fig. 3.1a) for three months, while for the control simulation, the model is kept forced over these three months (black circle, Fig. 3.1a). The monthly mean control WWV changes are consistent with those observed (Smith, 1995, available at https://www.pmel.noaa.gov/tao/wwv/data/), as indicated by a correlation of 0.86 and a similar pre- to post-2000 decline in STD (Fig. 3.1b).

Adjusted contribution

The adjusted contribution (Fig. 3.1c) is the WWV anomaly after the SWM has run freely (without wind stress forcing) for 3 months (Fig. 3.1a). It largely consists of RWs reflected at the western boundary into the WWV region and some wind initiated RWs because (i) KWs reach the eastern Pacific boundary within 1-3 months where they take the majority of their signal poleward (McGregor et al., 2016), and

(ii) RW forced in the western/central Pacific where the strongest coupling between atmosphere and ocean is found (Deser and Wallace, 1990) have reached the western boundary within 3 months where they reflect into the WWV region. The adjusted response has a peak correlation of 0.80 to observed western Pacific (120-205°E) WWV anomaly (WWV$_{west}$ taken from: https://www.pmel.noaa.gov/elnino/upper-ocean-heat-content-and-enso) at a 3-month lag (Fig. 3.1d). The 3-month lag and the larger amplitude of WWV$_{west}$ partially arises from the adjusted SWM run using a 3-month long free evolution to mostly separate the reflected RW signal, whereas the WWV$_{west}$ additionally contains the RW and KW signals directly forced in the western WWV region (Izumo et al., 2019).

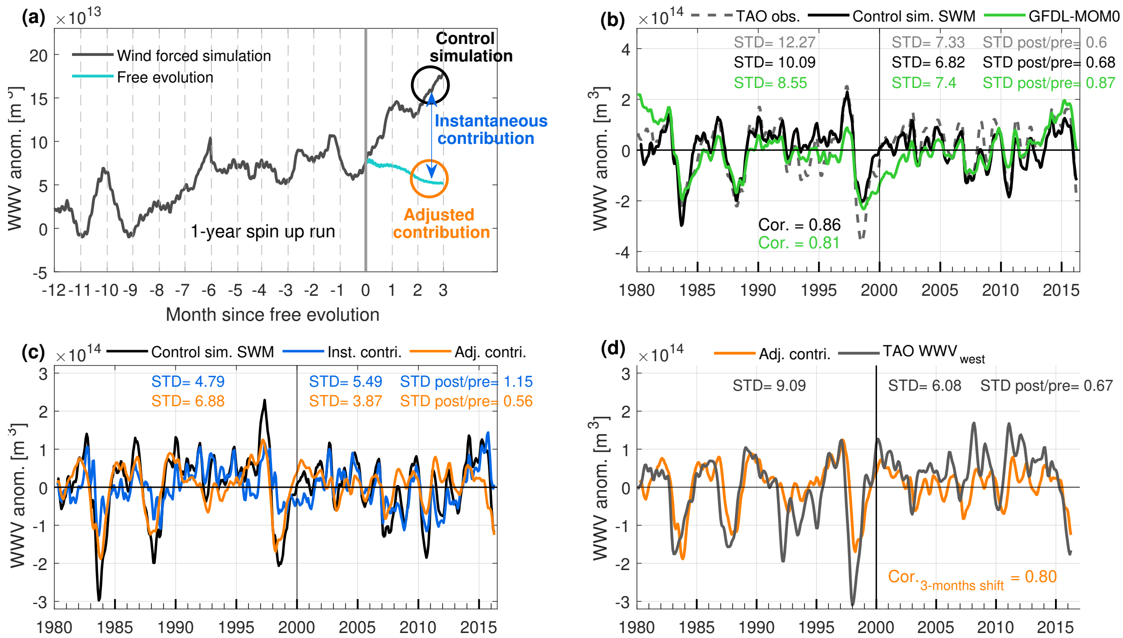

Figure 3.1: **(a)** Sketched example of obtaining (i) the control warm water volume (WWV), and (ii) the control WWV's adjusted and instantaneous contributions. The 1-year spin up run is initialized on 07/01/1982. The figure is taken from Neske and McGregor (2018) (Chapter 2) and slightly modified. **(b)** WWV anomaly of (black line) the SWM control simulation [m^3]; (green line) the GFDL-MOM025 simulation; and (dashed gray line) observations [m^3]. Correlations are calculated between the observed time series and (i) the SWM control simulation outcome (black number); and (ii) the GFDL-MOM025 simulation outcome (green number). Calculations for standard deviations (STDs) and correlations starting 1982. **(c)** SWM control WWV (black line) [m^3] and its instantaneous (blue line) and adjusted (orange line) contributions [m^3]. **(d)** Adjusted contribution (orange line) [m^3] and observed WWV$_{west}$ (gray line) [m^3]. The correlation is calculated when the adjusted contribution is lagging WWV$_{west}$ by 3 months. All pre- and post-2000 STDs in this figure are displayed in [10^{13} m^3].

Instantaneous contribution

The instantaneous contribution is the difference between the control WWV and the adjusted contribution (Fig. 3.1a, c). Therefore, the instantaneous contribution in any month is driven by winds over the 3-month period including the two months prior to and the month during the instantaneous contribution (Fig. 3.1a). It predominantly consists of the wind-forced KW signal in the eastern Pacific, largely dominating the wind-forced RW signal in the western Pacific (Neske and McGregor, 2018). The instantaneous contribution shows strong consistency with WWV changes due to meridional Ekman transport anomalies at 5°N and 5°S (Neske and McGregor, 2018).

Instantaneous east contribution

To understand the different adjusted responses of the strongest equatorial wind stresses, we analyze the wind stress forcing in the two months prior and the month during the strongest instantaneous signal east of 200°E ($WWV_{inst.east}$, Fig. 3.2a). Choosing the $WWV_{inst.east}$ signal rather than the instantaneous signal calculated over the entire WWV region removes the potential compensating WWV impacts of the wind-forced RW signal in the western Pacific, and allows us to focus on the wind stress forced KW WWV signal (see the larger amplitude of the dark blue line compared to the blue line in Fig. 3.2a). Thus, this choice ensures that we are analyzing the strongest wind stress at the equatorial region: The correlation of 0.92 between $WWV_{inst.east}$ and τ_{xeq} is slightly stronger than the correlation of 0.86 between the instantaneous WWV signal and τ_{xeq} (Fig. 3.2a). The $WWV_{inst.east}$ STD demonstrates a small pre- to post-2000 increase of 3% which is consistent with the pre- to post-2000 small increase of the instantaneous WWV STD (15%, Fig. 3.2a).

If not stated differently, all time series are smoothed by a 3-months running mean and correlations between time series are significant according to the method of Ebisuzaki (1997).

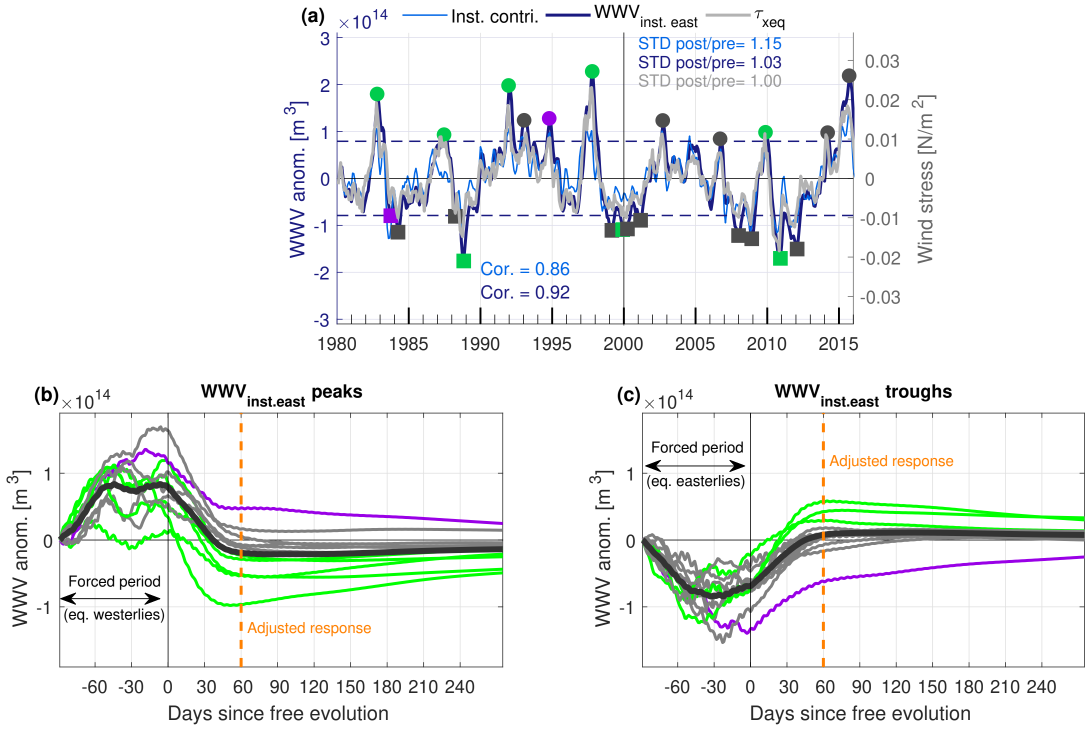

Figure 3.2: **(a)** Instantaneous contribution $[m^3]$ (thin blue line), WWV$_{inst.east}$ $[m^3]$ (Instantaneous contribution calculated east of 200°E) (dark blue line), and τ_{xeq} $[N/m^2]$ (gray line). Colored dots (squares) mark the WWV$_{inst.east}$ peaks/troughs above/below +/-1 STD of WWV$_{inst.east}$ ($0.79 \cdot 10^{14}$ m^3, horizontal dashed line). **(b)**/**(c)** Composite (thick black lines) and single WWV outcomes (gray and colored lines) $[m^3]$ of the SWM forced by westerly/easterly wind stresses over the 3-month periods leading to the WWV$_{inst.east}$ peaks/troughs as identified in **(a)**. Vertical black line marks the end of the forcing period and vertical dashed orange line marks the begin of the adjusted response. Simulations with adjusted responses (averaged over day 60-90) in **(b)**/**(c)** are colored (i) green when falling below/exceeding $-0.2 \cdot 10^{14}/0.2 \cdot 10^{14}$ m^3 (transitioning adjusted responses), (ii) gray when lying between $0.2 \cdot 10^{14}$ and $-0.2 \cdot 10^{14}$ m^3 (neutral adjusted responses), and (iii) purple when exceeding/falling below $0.2 \cdot 10^{14}/-0.2 \cdot 10^{14}$ m^3 (persistent adjusted responses).

3.3 Categorizing adjusted WWV responses

To understand the different adjusted responses following the strongest WWV$_{inst.east}$ signal (strongest equatorial wind stress), we identify 11 peaks (12 troughs) above/below +/-1 STD of the WWV$_{inst.east}$ time series (dots and squares, Fig. 3.2a). We then force the SWM with the 3-months westerly (easterly) wind stress forcing of each identified peak (trough) (i.e. in the two months prior and the month during the peak/trough). After the 3-months forcing period the SWM is left to freely evolve for 9 months (Fig. 3.2b and c). The simulated adjusted WWV responses (averaged over day 60-90 after the start of the free evolution, when the KWs have left the WWV region) is separated into 3 categories depending on their sign and magnitude. These are: (i) transitioning where the westerly (easterly) wind forcing leads to a discharged (recharged) adjusted response that has an absolute magnitude larger than $0.2 \cdot 10^{14}$ m^3 (green lines in Fig. 3.2b and c; the initial KW WWV signal transitions to the opposite sign WWV due to the oceanic dynamic adjustment as expected from traditional theory); (ii) neutral, which has a relatively small adjusted response with an absolute magnitude less than $0.2 \cdot 10^{14}$ m^3 (gray lines, Fig. 3.2b and c); and (iii) persistent, where the westerly (easterly) wind forcing leads to a recharged (discharged) adjusted response above (below) $0.2(-0.2) \cdot 10^{14}$ m^3 (purple lines in Fig. 3.2b and c).

It is clear that only around a third of the simulations (8 out of 23) produce a transitioning adjusted response that is expected from theory (green dots and squares in Fig. 3.2a). Furthermore, the ratio of transitioning responses to those remaining (neutral plus persistent responses) is 5:6 for the westerly wind stress forcing of $\text{WWV}_{inst.east}$ peaks (dots in Fig. 3.2a), while it is only 3:9 for the easterly wind stress forcing of $\text{WWV}_{inst.east}$ troughs (squares in Fig. 3.2a). Consequently, the composite adjusted discharge following the $\text{WWV}_{inst.east}$ peaks (averaged over day 60-90) is around twice as strong as the composite adjusted recharge of the $\text{WWV}_{inst.east}$ troughs forcing (compare thick black lines in Fig. 3.2b and c). This asymmetry suggests that the strongest westerly forcings have a larger potential as a long-term precursor for La Niña events compared to the strongest easterly forcings for El Niño events.

Additionally, during the pre-2000 period four times more transitioning adjusted responses are found, compared to the post-2000 period (green dots and square in Fig. 3.2a). The dominance of neutral (gray dots and squares in Fig. 3.2a) over transitioning responses in the post-2000 period is consistent with the post-2000 reduction of the STD of the adjusted response found by Neske and McGregor (2018) (Fig. 3.1c).

As persistent responses are only found twice during the analysis period, once for the $WWV_{inst.east}$ peaks and once for the troughs (purple lines in Fig. 3.2b and c), we only briefly discuss analysis of these events as it is not possible to assess the statistical significance of the difference. However, as these two persistent responses are very extraordinary cases (the opposite of what is expected from ENSO theory, e.g. Jin, 1997) we keep to present the results of the persistent responses throughout the figures. The following section retains a focus on the characteristics of and differences between the transitioning and neutral simulations.

3.4 Composite winds and their underlying SSTAs

a) Wind stress composites

To better understand the differences between the transitioning and neutral WWV responses, we make composites of the 3-month average zonal winds that have led to $WWV_{inst.east}$ peaks and troughs according to their adjusted responses, i.e, (i) transitioning responses (green composite Fig. 3.3a and b), (ii) neutral responses (gray composite Fig. 3.3c and d), and (iii) persistent responses (purple composite Fig. 3.3e and f) as identified in Section 3.4 (Fig. 3.2b and c).

The transitioning adjusted discharge composite displays strong anomalous equatorial westerly wind stress between around 160-230°E (Fig. 3.3a and g). The anomalous westerly wind stress decreases poleward abruptly at around 5°N and 5°S (Fig. 3.3a and h), inducing strong wind stress curls at the bounds of the WWV region (shading, Fig. 3.3a). The transitioning adjusted recharge composite wind forcing is almost the mirror image (easterly wind stress), with the exception of the winds being shifted westward by around 20°(Fig. 3.3b, g and h).

Comparing the transitioning and neutral zonal wind composites of WWV inst.east peaks, it is clear that the neutral composite (i) has weaker equatorial winds; (ii) displays a smaller zonal extent (Fig. 3.3c and d; compare gray and green lines in Fig.

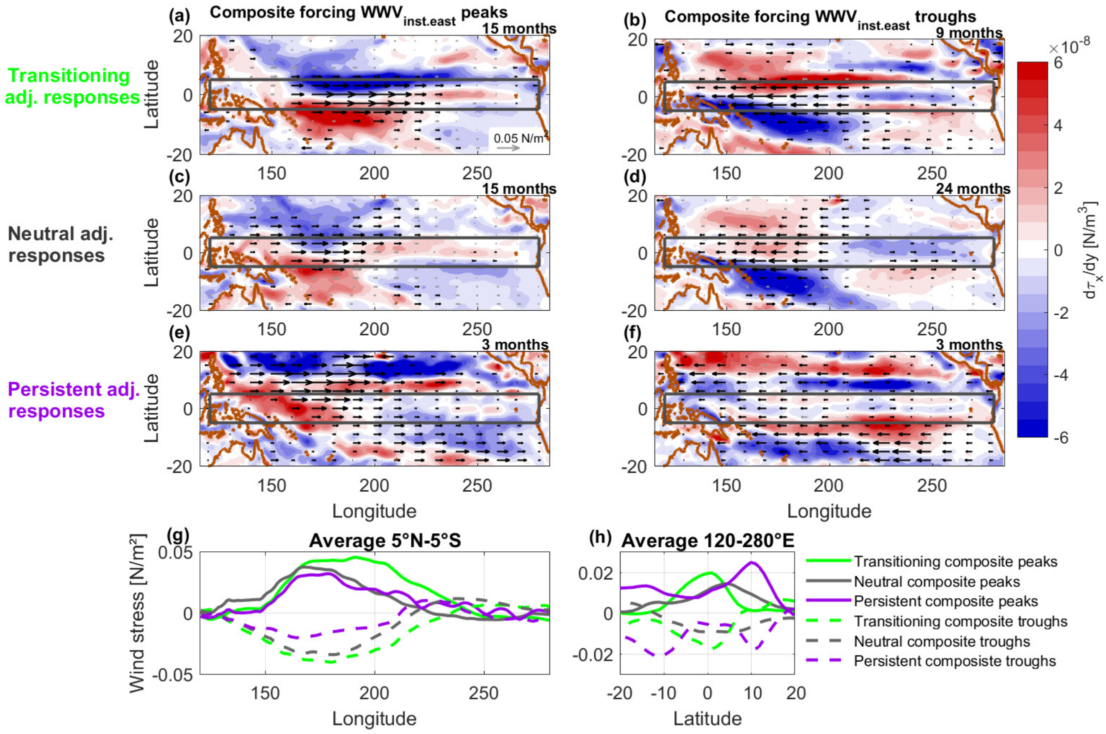

Figure 3.3: Composited zonal wind stress $[N/m^2]$ (arrows) and its curl ($\frac{\partial \tau_x}{\partial y}$) $[N/m^3]$ (shading) of the WWV$_{inst.east}$ peaks/troughs forcing periods with a **(a)**/**(b)** transitioning (green), **(c)**/**(d)** neutral (gray), and **(e)**/**(f)** persistent (purple) adjusted response according to Figure 3.3b and c. The number in the upper right corner gives the amount of months considered for each composite. Black arrows give the significant wind stress found by bootstrapping with 1000 samples at the 95% confidence interval. **(g)**/**(h)** Wind stress $[N/m^2]$ of each composite averaged over 5°N -5°S/ 120°E-280°E.

3.3g); and (iii) is meridionally broader (Fig. 3.3c, d and h). Very similar differences are also seen when comparing the transitioning and neutral zonal wind composites of WWV inst.east troughs. This broader meridional pattern of the neutral zonal wind stress leads to weaker wind stress curls close to the poleward edges of the WWV region than those seen in the transitioning composites (shading, compare Fig. 3.3c with a and Fig. 3.3d with b). Additionally, the neutral composite wind stress curl around the east Pacific WWV region is of opposite sign to the wind stress curl around the western Pacific region (shading Fig. 3.3c and d).

The zonal extent of the persistent WWV$_{inst.east}$ equatorial wind forcing (averaged over 5°N and 5°S) is close to that of the composite neutral WWV$_{inst.east}$ for both peaks and troughs (Fig. 3.3e and f, purple and gray lines in Fig. 3.3g). In contrast to the neutral composite, however, the anomalous wind stresses increase polewards of the WWV region in both hemispheres (purple and gray lines in Fig. 3.3h). This induces strong wind stress curl especially at the North of the WWV region which is of opposite sign from that of the corresponding transitioning wind stress forcing (shading Fig. 3.3e and f).

b) Underlying SSTAs

The $WWV_{inst.east}$ displays a strong linear relationship (correlation of 0.91) to Niño 3.4 SSTA (Fig. 3.4a). Consequently, the strongest peaks (troughs) of the $WWV_{inst.east}$ are found during warm (cold) phases of ENSO (colored dots/squares Fig. 3.4a). The transitioning adjusted responses (green colors Fig. 3.4a) generally display a stronger Niño 3.4 SSTA magnitude compared to the neutral responses (gray colors Fig. 3.4a). Comparing the underlying composite SSTA patterns, averaged over the 3-month period of $WWV_{inst.east}$ peaks and troughs forcing (Fig. 3.4b-g), reveals that the transitioning (neutral and persistent) composites' SSTA pattern display their strongest magnitudes in the eastern (central) Pacific consistent with the SSTA of EP (CP) ENSO events (e.g. McPhaden et al. 2011). This finding is largely consistent when looking at the SSTAs during the forcing periods of each single simulation: For 80/100% of the transitioning $WWV_{inst.east}$ peaks/troughs the Niño 3 SSTA magnitude (averaged over 210-270°E and 5°N-5°S) is larger compared to the Niño 4 SSTA magnitude (averaged over 160-210°E and 5°N-5°S). In contrast, the Niño 3 SSTA magnitude is smaller than the Niño 4 SSTA magnitude for 80/88% of the neutral peaks/troughs simulations.

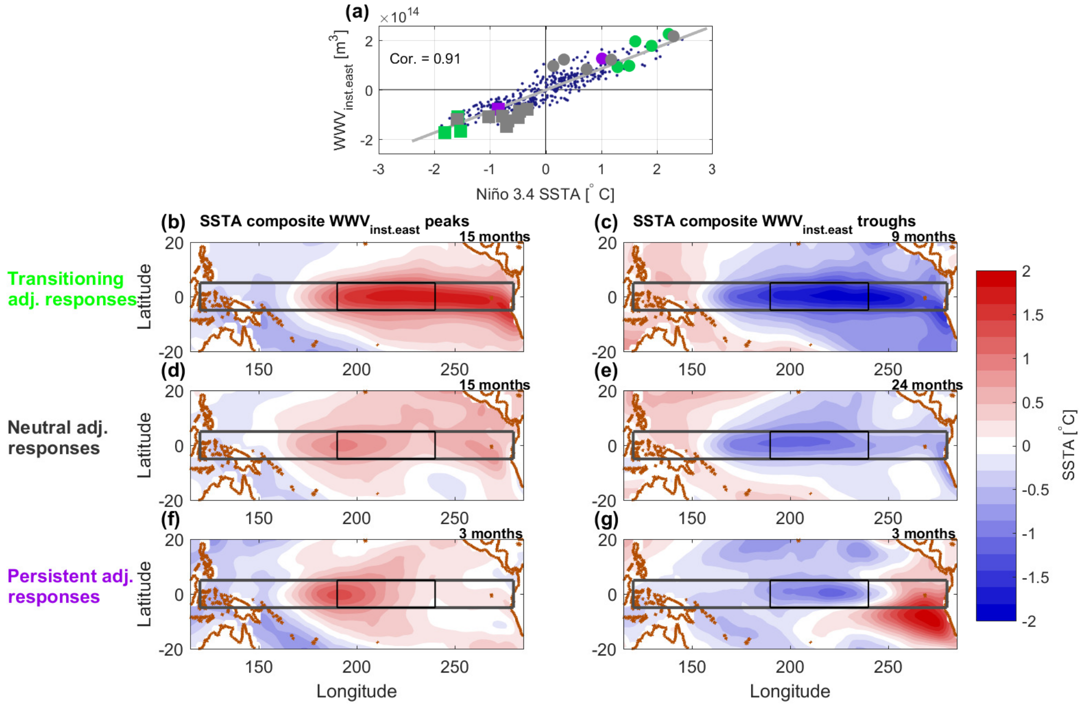

Figure 3.4: **(a)** WWV$_{inst.east}$ [m^3] plotted against Niño 3.4 SST anomaly [°C]. Dots/squares mark the WWV$_{inst.east}$ peaks/ troughs with transitioning (green), neutral (gray), and persistent adjusted responses (purple) according to Figure 3.3b and c. Lower panels: Composite sea surface temperature anomaly [°C] during the 3-month WWV$_{inst.east}$ peaks/troughs forcing periods with a **(a)**/**(b)** transitioning, **(c)**/**(d)** neutral, and **(e)**/**(f)** persistent adjusted response. The number in the upper right corner gives the amount of months considered for each composite. Small black box marks the Niño 3.4 region.

3.5 Understanding the warm water volume response

To get a better understanding of the WWV response of the different categories of adjusted responses, we carry out another set of SWM experiments. In this case one SWM experiment is carried out for each category of adjusted response, and each simulation is forced over 3 months with the composite mean wind field (Fig. 3.3). After this initial forcing period the SWM is allowed to freely evolve (i.e., with no wind forcing) for 9 months. We allowed a 10-day linear increase (decrease) of wind stress forcing starting from (going towards) 0 at the beginning (end) of the 3-month forcing period. The pycnocline outcome is averaged over: (i) the last month of the forcing period (day -30 to 0), which gives the instantaneous response (Fig. 3.5a, d, g and Fig. 3.6a, d, g); (ii) the third month of the free evolution (day 60 to 90), which gives the adjusted response (Fig. 3.5b, e, h and Fig. 3.6b, e, h); and (iii) the eighth month of the free evolution (day 210 to 240), which gives the late adjusted response (Fig. 3.5c, f, i and Fig. 3.6c, f, i).

a) WWV$_{inst.east}$ peaks

The equatorial region westerly wind stresses in all forcing composites (Fig. 3.3a, c, e) excite downwelling KWs and an increase in WWV$_{inst.east}$ magnitude which differs by less than around 20% between the different categories (Fig. 3.5a, d and g). In contrast, the instantaneous discharge calculated west of 200°E is clearly largest for the transitioning composite and is around: (i) 54% smaller for of the neutral composite; and (ii) 75% smaller for the single persistent case (compare Fig. 3.5a with d and g).

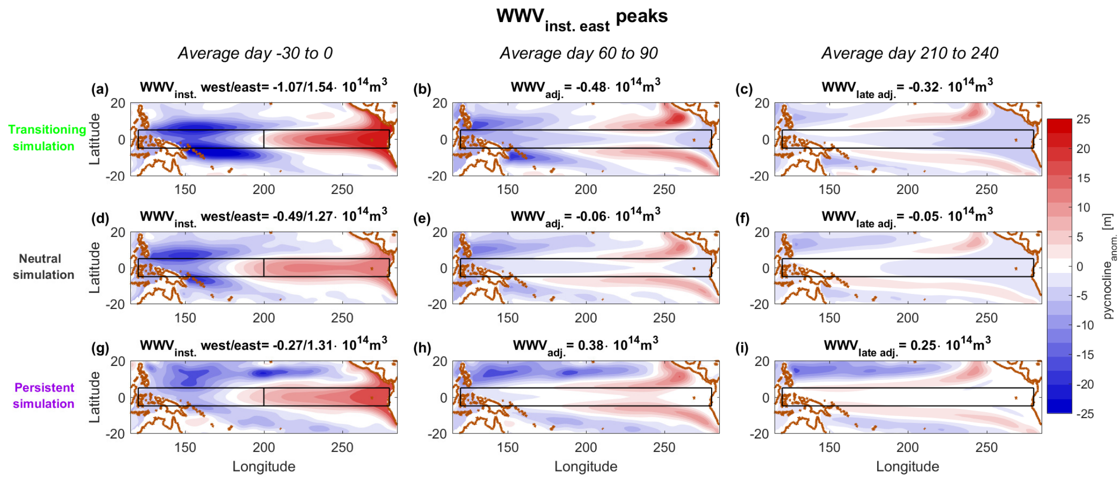

Figure 3.5: Pycnocline anomaly output [m] averaged over days **(a, d, g)** -30 to 0 (instantaneous response), **(b, e, h)** 60 to 90 (adjusted response), and **(c, f, i)** 210 to 240 (late adjusted response) since the free evolution of the WWV$_{inst.east}$ peaks SWM simulations. The SWM simulations are forced over 3 months by the adjusted **(a-c)**, neutral **(d-f)** and persistent **(g-i)** wind stress composite as shown in Fig. 3.3a, c and e.

The differences in instantaneous WWV west of 200°E among the composites is primarily explained by differences in the strength and sign of the wind stress curl in each Hemisphere (Fig. 3.3a, c, e). Note that both negative wind stress curl dominating the Northern Hemisphere and positive wind stress curl dominating the Southern Hemisphere excite upwelling RWs. The differences of the curl patterns of Fig. 3.3 are strongly consistent with those curl patterns divided by the Coriolis parameter f (Fig. A3.1). This is noted as the RW signal is determined by Ekman pumping which divides the wind stress curl by f. Our focus is on the RW signal equatorward of +/-8° as the western boundary reflection efficiency of RWs has shown to be inefficient poleward of +/-8° (Kessler 1991). The transitioning forcing category (Fig. 3.3a) gives the "ideal" case (as expected from theory) with westerly winds accompanied by strong negative (positive) wind stress curl around the WWV regions northern (southern) bounds which excites strong upwelling RWs in both Hemispheres (blue shading, Fig. 3.5a). In comparison, the weaker wind stress curl and the smaller zonal wind extent of the neutral forcing category (Fig. 3.3c) excites comparatively weaker upwelling RWs at a similar distance to the equator (blue shading, Fig. 3.5d). The persistent peak forcing wind stresses display wind stress curls of mixed sign in each Hemisphere (Fig. 3.3e) which leads to an almost neutral (slightly upwelling) RW signal close to the equatorial region.

The transitioning composite simulation clearly shows an adjusted (Fig. 3.5b) and a late adjusted discharge (Fig. 3.5c) when the strong upwelling RWs reflect at the western boundary into the WWV region (blue areas in Fig. 3.5b and c) and the forced downwelling KWs has largely left the WWV region to travel poleward at the eastern boundary (red areas in Fig. 3.5b and c). In comparison, the RW signal of the neutral composite simulation reflecting into the WWV region is much weaker (red area in Fig. 3.5e) and leads to no adjusted or late adjusted discharge (Fig. 3.5e and f). The single persistent case simulation clearly displays an adjusted (Fig. 3.5h) as well as a late adjusted recharge (Fig. 3.5i). This adjusted recharge is due to the almost nonexistent upwelling RW signal not counterbalancing the downwelling KW signal, and that the KW signal maintains a small downwelling presence in the WWV region after reflection into RWs at the eastern boundary (Fig. 3.5h).

b) WWV$_{inst.east}$ troughs

The spatial pattern of the pycnocline in the WWV$_{inst.east}$ trough simulations virtually mirror those of the WWV$_{inst.east}$ peak simulations for instantaneous, adjusted and late adjusted outcomes (compare Fig. 3.5 with Fig. 3.6; spatial correlations between 15°N and 15°S vary between -0.78 and -0.97). A difference is found in the adjusted response of the transitioning simulation, as the trough simulation is around 21% weaker than the peak simulation (Fig. 3.5b and 7b). The stronger adjusted response of the transitioning peak simulation can be explained by the stronger wind stress curl closer confined to the WWV edges where excited RW have a stronger western boundary reflection efficiency (Kessler, 1991) compared to that of the transitioning trough simulation (Fig. 3.3a and b): The upwelling wind stress curl of the transitioning peak simulation is around 22% stronger from 120-280°E and from 2-5° latitude where the first mode RW projection is strongest (e.g. McGregor et al., 2016) than the downwelling wind stress curl of the transitioning trough simulation.

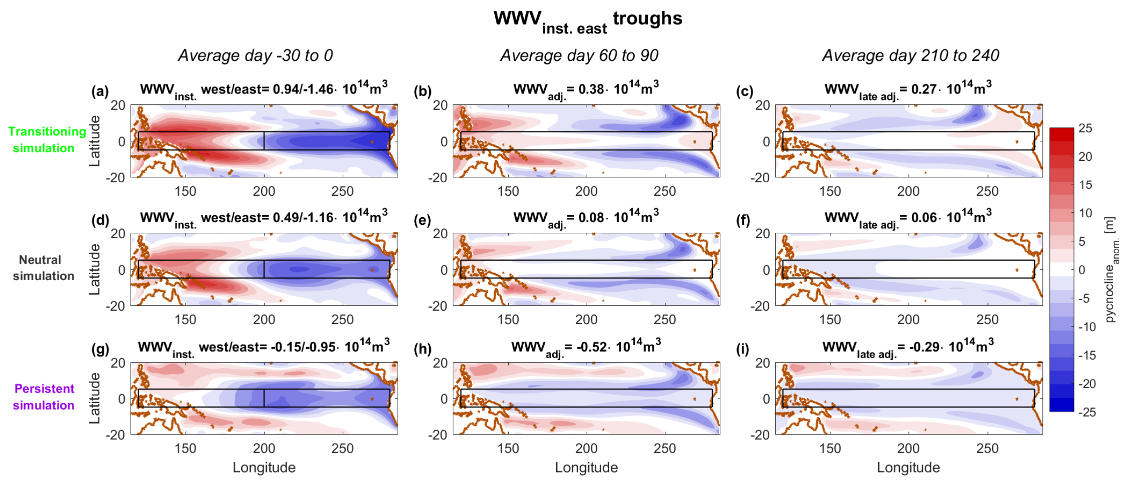

Figure 3.6: Same as Fig. 3.5 but for the WWV$_{inst.east}$ troughs SWM simulations forced with the wind stress composite as shown in Fig. 3.3b, d and f.

The WWV magnitude and pycnocline spatial patterns for both the instantaneous and adjusted responses are largely consistent when conducting the experiments of this Section with the more comprehensive global ocean sea ice model GFDL-MOM025 (Fig. A3.2, for a model description see Zeller et al., 2019). Thus, we conclude that the results presented here are not significantly impacted by the simplicity of the ocean model utilized.

c) Idealized wind stress experiments

We conduct a simple experiment to better understand if the stronger adjusted response of the $\mathrm{WWV}_{inst.east}$ peaks transitioning forcing compared to the neutral forcing is due to: (i) the larger longitudinal wind stress extent of the zonal transitioning forcing (Fig. 3.3a); or (ii) the larger latitudinal extent of zonal wind stress forcing of the neutral forcing (Fig. 3.3c). To this end, we produce wind forcings that have (i) the average longitudinal extent of the transitioning peak simulation and the average latitudinal extent of the neutral peak simulation (Fig. 3.7c, red line Fig. 3.7e and f); and (ii) the average longitudinal extent of the neutral peak simulation and the average latitudinal extent of the transitioning peak simulation (Fig. 3.7d, blue line Fig. 3.7e and f). We also carry out two additional simulations which utilize the average longitudinal and latitudinal extent of the transitioning and neutral simulations for comparison (idealized transitioning and neutral forcings, Fig. 3.7a and b). We firstly note, that the idealized adjusted wind stress curl pattern and its adjusted response is consistent to the non-idealized equivalent (compare Fig. 3.3a with 3.8a, and green solid and dashed lines in Fig. 3.7g). The wind stress curl pattern of the idealized neutral forcing does not display the longitudinal variability of its non-idealized equivalent (compare Fig. 3.3c with 3.8b), however, its adjusted response is also very small but of opposite sign (gray solid and dashed lines in Fig. 3.7g).

The consistency of the idealized and non-idealized forcing WWV changes suggest that this experiment will provide a reasonable base to better understand the relative importance of the wind stress forcing's latitudinal and longitudinal extent. The adjusted response of the longitudinal neutral and latitudinal transitioning forcings shows a clear discharge that is by only 29% weaker than that of the idealized transitioning composite forcing (compare blue and green dashed lines in Fig. 3.7g). In contrast, the differences between the adjusted responses of the transitioning longitudinal and neutral latitudinal forcing and the idealized neutral forcing is negligible (red and gray dashed lines in Fig. 3.7g). These results indicate that the latitudinal extent of the wind stress forcing plays the prominent role in determining the strength of the adjusted response and the longitudinal extent plays a secondary role.

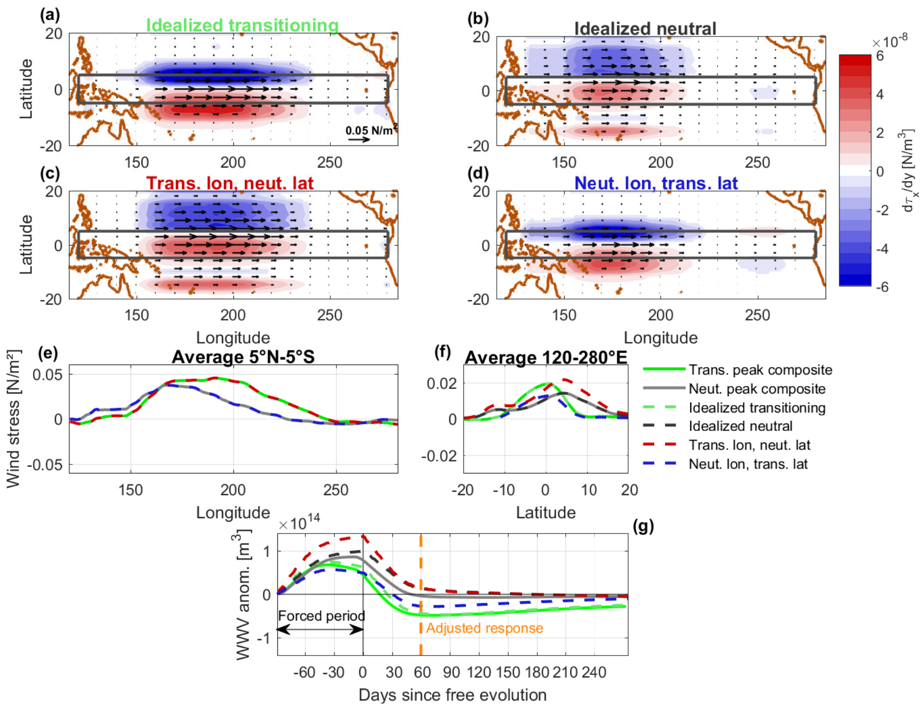

Figure 3.7: Zonal wind stress $[N/m^2]$ (black arrows) and wind stress curl of the zonal wind stress $[N/m^3]$ (shading) of **(a)**/**(b)** idealized transitioning/neutral forcing with the average longitudinal and latitudinal extent of the transitioning/neutral peak composite (Fig. 3.3a and c); and **(c)**/**(d)** produced forcing with the average longitudinal extent of the transitioning/neutral peak composite and the average latitudinal extent of the neutral/transitioning peak composite. **(e)**/**(f)** Wind stress $[N/m^2]$ of each composite (Figure 3.3a,c and this Figure a-d) averaged over 5°N-5°S/ 120°E-280°E. **(g)** WWV outcome $[m^3]$ when constantly forcing the SWM over 3 months with the forcings shown in Figure 3.3a,c and this Figure a-d before the SWM is let to freely evolve. Vertical black line marks the end of the wind stress forcing period and vertical dashed orange line marks the begin of the adjusted response.

A similar result is found when comparing the magnitude of τ_{xeq} with the magnitude of the adjusted response for each transitioning and each neutral simulation: Some of the τ_{xeq} forcings of the neutral simulations have a stronger magnitude compared to the transitioning simulations, however, the adjusted WWV is weaker (Fig. 3.8a). Additionally, the absolute value of the ratio of adjusted WWV and τ_{xeq} is significant larger (applying a two-sided t-test at the 95% confidence interval) for the transitioning simulations compared to the neutral simulations (Fig. 3.8b). Summarizing, this means that when there is a strong wind stress curl around the poleward edges of the WWV region and the zonal wind stress has a large longitudinal extent and a strong magnitude, more RWs are excited leading to a stronger adjusted response (compare blue dashed and green dashed line in Fig. 3.7g). However, when there is a weak wind stress curl around the poleward edges of the WWV region, weak RWs are excited and extending this forcing longitudinally or strengthening the magnitude of τ_{xeq} has little impact on the neutral adjusted response (compare red and gray dashed line in Fig. 3.7g).

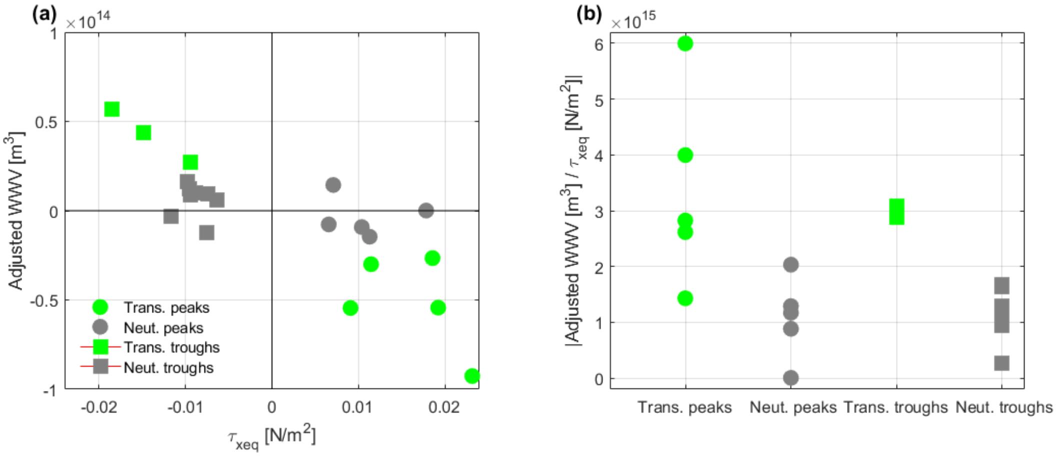

Figure 3.8: **(a)** Adjusted WWV [m^3] of the transitioning (green) and neutral (gray) WWV$_{inst.east}$ peak/trough simulations (dots/squares) (see Fig. 3.2) as function of τ_{xeq} [N/m^2] (zonal wind stress anomaly averaged over the WWV region) averaged over the 3-month forcing period of each peak and trough. **(b)** Absolute value of the ratio of the adjusted WWV [m^3] and τ_{xeq} [N/m^2] of **(a)**.

3.6 Average winds vs. high frequency wind events-looking at the problem from different angles

To better understand the link between the longer-term average composite wind stress (Fig. 3.3) and those of high frequency wind events, we identify the anomalous wind events in 11 different regions around the tropical Pacific (black boxes, Fig. 3.9a and c). A westerly (easterly) wind event (WWE/EWE) is identified when the zonal mean wind stress averaged over a given region and smoothed by a triangle filter in time exceeds (falls below) 0.04 N/m^2 (-0.04 N/m^2) for a period of 3 or more days (consistent with McGregor et al., 2016). We sum the wind events in each region for each 3-month forcing period of all of the previously identified adjusted

WWV categories, (i) transitioning, (ii) neutral, and (iii) persistent; for both the WWV$_{inst.east}$ peaks and troughs (numbers in Fig. 3.9a and c). We further distinguish between equatorial wind events (located in the 4 boxes between 5°N and 5°S, Fig. 3.9a and c) and off-equatorial wind events (located in the 7 boxes between 5°N-15°N and 5°S-15°S, Fig. 3.9a and c).

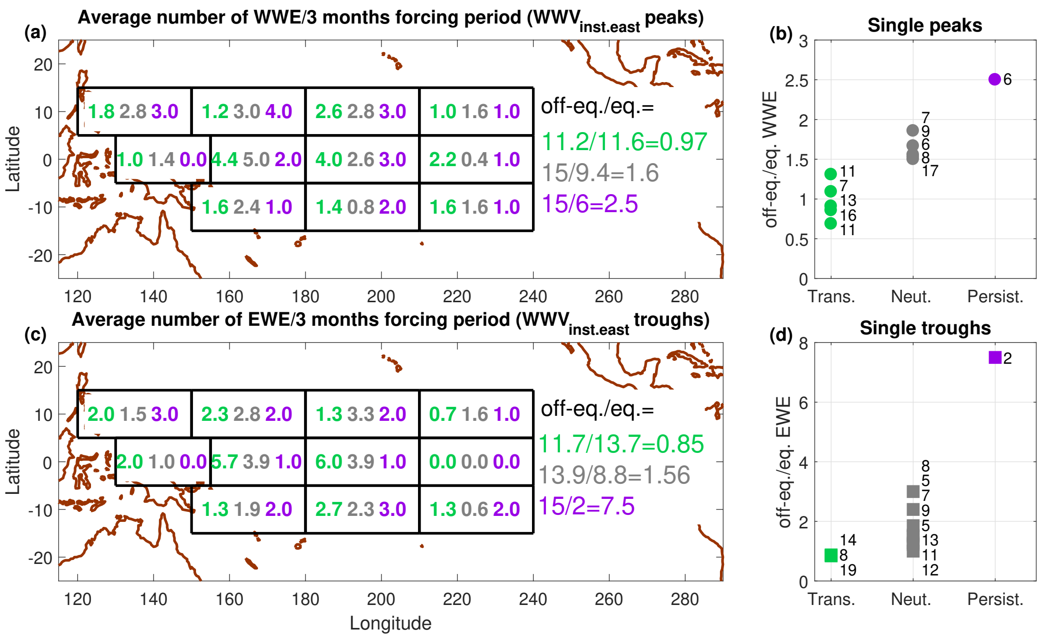

Figure 3.9: **(a)/(c)** Average number of westerly wind events (WWE)/easterly wind events (EWE) during the 3-month forcing periods of the WWV$_{inst.east}$ peaks'/troughs' transitioning (green numbers), neutral (gray numbers) and persistent (purple numbers) simulations (Fig. 3.2b and c) for 11 different regions in the equatorial Pacific as marked by the boxes. **(b)/(d)** Ratio of off-equatorial to equatorial WWE/EWE during the 3-month forcing periods of each single WWV$_{inst.east}$ peak/trough transitioning (green), neutral (gray) and persistent (purple) simulation. Black numbers give the number of equatorial wind events included in each single 3-month forcing period. Note the difference in Y-axis scaling between **(b)** and **(d)**.

The average ratio of off-equatorial to equatorial westerly (easterly) wind events during these 3-month forcing periods is lowest for forcing periods that are categorized as transitioning (0.97 for the peaks and 0.85 for the troughs), and substantially larger for those categorized as neutral (1.6 for the peaks and 1.56 for the troughs) and persistent simulations (2.5 for the peaks and 7.5 for the troughs). On average we see that the transitioning peak (trough) simulations are forced by around 23% (56%) more equatorial WWE (EWE) during the 3-month forcing period compared to the neutral simulations. In contrast, the 3-month forcing periods of the neutral peak (trough) simulations have on average around 34% (19%) more off-equatorial WWE (EWE) than the transitioning peak (trough) simulations. Further to this, looking for hemispheric differences in the changes in the number of off-equatorial wind events we find that the average number of off-equatorial westerly/easterly wind events in the SH are very similar for transitioning (4.6/5.3) and neutral (4.8/4.8) peak/trough simulations. This means that the increase in off-equatorial to equatorial wind events ratio seen during neutral transitioning responses arises due to differences in the number of NH off-equatorial wind events (on average 6.6/6.3 and 10.2/9.1 WWE/EWE for the transitioning and neutral peak/trough simulations respectively). Furthermore, there is little to no change in the total number of EWE (WWE) occurring during the 3-month forcing periods of the $\mathrm{WWV}_{inst.east}$ peaks (troughs) simulations is (not shown here).

When examining the wind events within the individual event forcing periods separately (Fig. 3.2), we see no significant difference in the average number of equatorial wind events of the transitioning simulations compared to the neutral and persistent simulations (black numbers in Fig. 3.9b and d). The same is true for off-equatorial wind events and for the difference in NH and SH off-equatorial wind events. However, the ratio of off-equatorial to equatorial WWE during the peak simulations is significantly different (applying a t-test at the 95% confidence interval) when comparing the transitioning simulations (ranging from 0.67-1.31, green dots in Fig. 3.9b) with the neutral (ranging from 1.5-1.86, gray dots in Fig. 3.9b) and persistent simulations (2.5, purple dot in Fig. 3.9b). The ratio of off-equatorial to equatorial EWE during the 3-month forcing periods of the trough simulations is also clearly smaller for the transitioning simulations (0.84-0.86, green squares Fig. **??**d) when compared with the neutral (1-3, gray squares Fig. 3.9d) and persistent simulations (7.5, purple square Fig. 3.9d). While the difference in the off-equatorial to equatorial EWE ratio between the transitioning and persistent trough simulations is statistically significant at the 95% confidence interval, the difference between the transitioning and neutral trough simulations is statistically significant at the 90% confidence interval. This may be due to the lower number of samples of the transitioning trough simulation (only 3 forcing periods, see Fig. 3.2).

These results demonstrate a clear consistency between the composite winds (Fig. 3.3) and the wind events of each single simulation (Fig. 3.9). The strong wind stress curls equatorward of around +/-8° of the transitioning simulations (Fig. 3.3a and b) can only be produced by a lower off-equatorial to equatorial wind event ratio (green numbers Fig. 3.9) compared to the weaker wind stress curls at the WWV boundaries (Fig. 3.3c and d) of the neutral simulations (gray numbers Fig. 3.9). Moreover, the equatorial westerly (easterly) wind stress of the persistent simulations can only induce positive (negative) wind stress curl in the NH and negative (positive) wind stress curl in the SH (Fig. 3.3e and f) when accompanied by a large amount of off-equatorial WWE (EWE) (purple numbers Fig. 3.9).

3.7 ENSO precursor?

This paper has examined the difference in wind stress patterns leading to differences in oceanic adjusted responses following the strongest equatorial wind stress forcings. We note that the strongest adjusted WWV changes in our simulations (which are up to $0.38/-0.52 \cdot 10^{14}\ m^3$, Fig. 3.5 and 3.6) are much smaller than the extrema of the adjusted time series shown in Fig. 3.1c (orange line). The reason for this disparity is, that the adjusted time series in Fig. 3.1c is received by forcing the SWM by 12 rather than only 3 months before the SWM is left to freely evolve for 3 months (see Fig. 3.1a, Section 3.2). Izumo et al. (2019) show that a constant equatorial westerly wind forcing over a longer time period, leads to a constructive interference of upwelling RWs in the western Pacific for RWs forced by winds at different times and locations (their Fig. 5). Consequently, when a larger up- or downwelling signal is accumulating in the western Pacific we expect a stronger adjusted response.

For this section we aim to understand whether (i) the 3-months forced adjusted signal that we can predict some months in advance is representative of the total WWV; and (ii) we can potentially gain predictive skill for ENSO using the 3-months forced adjusted signal. Thus, we examine if the 3-month forced adjusted response can be related to the 12-month forced adjusted response and if this adjusted response can be linked to the control WWV (see Fig. 3.1a and b and Section 3.2). Furthermore, we analyse whether the transitioning and neutral categories can be linked to ENSO SST.

The STD of the 3-month forced adjusted response contributes 42% (52%) of the STD of the 12-month forced adjusted response during the pre- (post-) 2000 period (Fig. A3.3). They have a correlation of 0.8 and both time series show a clear pre- to post-2000 decline in STD (44% and 31% for the 12-month and 3-month adjusted responses respectively, Fig. A3.3). The strongest 12-month forced adjusted responses are found around 6-10 months after the adjusted WWV$_{inst.east}$ peaks and troughs (Fig. A3.4a and b); and the strongest control WWV is found around 5-12 months after the adjusted WWV$_{inst.east}$ peaks and troughs (Fig. A3.4c and d). The neutral simulations show no clear strongest adjusted response or strongest control WWV (Fig. A3.4). Consequently, in the following we examine the 12-month adjusted response and the control WWV 8 months after the WWV$_{inst.east}$ peaks/troughs. For simplicity we refer to the 12-months forced adjusted contribution as the "adjusted contribution" in the following of this Section.

a) WWV$_{inst.east}$ peaks

The average adjusted discharge of the transitioning peak simulations 8 months after the WWV$_{inst.east}$ peaks ($-1 \cdot 10^{14}$ m^3, green dots Fig. 3.10a) is around 3.6 times larger than that of the neutral peak simulations 8 months after the WWV$_{inst.east}$ peaks ($-0.28 \cdot 10^{14}$ m^3, gray dots Fig. 3.10a). Note that one neutral peak is missing in this analysis as it was at the end of the time series (see Fig. 3.2a). The average instantaneous response 8 months after the adjusted WWV$_{inst.east}$ peaks is also a clear discharge ($-0.63 \cdot 10^{14}$ m^3, green dots Fig. 3.10b). This suggests that the adjusted discharge after the adjusted WWV$_{inst.east}$ peaks is strong enough to cool the Niño 3.4 region SSTs around 7 months after the WWV$_{inst.east}$ peaks (Fig. 3.11a). This change in the sign of Niño 3.4 anomalies then transitions the system towards easterly winds, which explains the strong instantaneous discharge 8 months after the adjusted $WWV_{inst.east}$ peaks. This change in equatorial zonal wind anomaly direction is also consistent with the studies of McGregor et al. (2012b, 2013) that show an after-event southward movement of westerly winds leading predominantly to equatorial region easterlies. Both, instantaneous and adjusted responses of the average transitioning peak simulation combine to strongly discharge the WWV region (on average $-1.63 \cdot 10^{14}$ m^3, see control WWV of the green dots in Fig. 3.10 a and c). This leads on average to La Niña-like SSTs 12 months after the $WWV_{inst.east}$ peaks (Niño 3.4 SST= -1.1 °C, green dots Fig. 3.10e; green lines Fig. 3.11a). In contrast, the instantaneous recharge ($0.22 \cdot 10^{14}$ m^3, gray dots Fig. 3.10c) 8 months after the neutral $WWV_{inst.east}$ peaks destructively interferes with the adjusted discharge, leading to an average negligible control WWV anomaly ($-0.06 \cdot 10^{14}$ m^3, see control WWV of the gray dots in Fig. 3.10a and c). As a result, the neutral peak simulations lead on average to no clear ENSO SST signal 12 months after the $WWV_{inst.east}$ peaks (Niño 3.4 SST= -0.04 °C, gray dots Fig. 3.10e: gray lines Fig. 3.11 a).

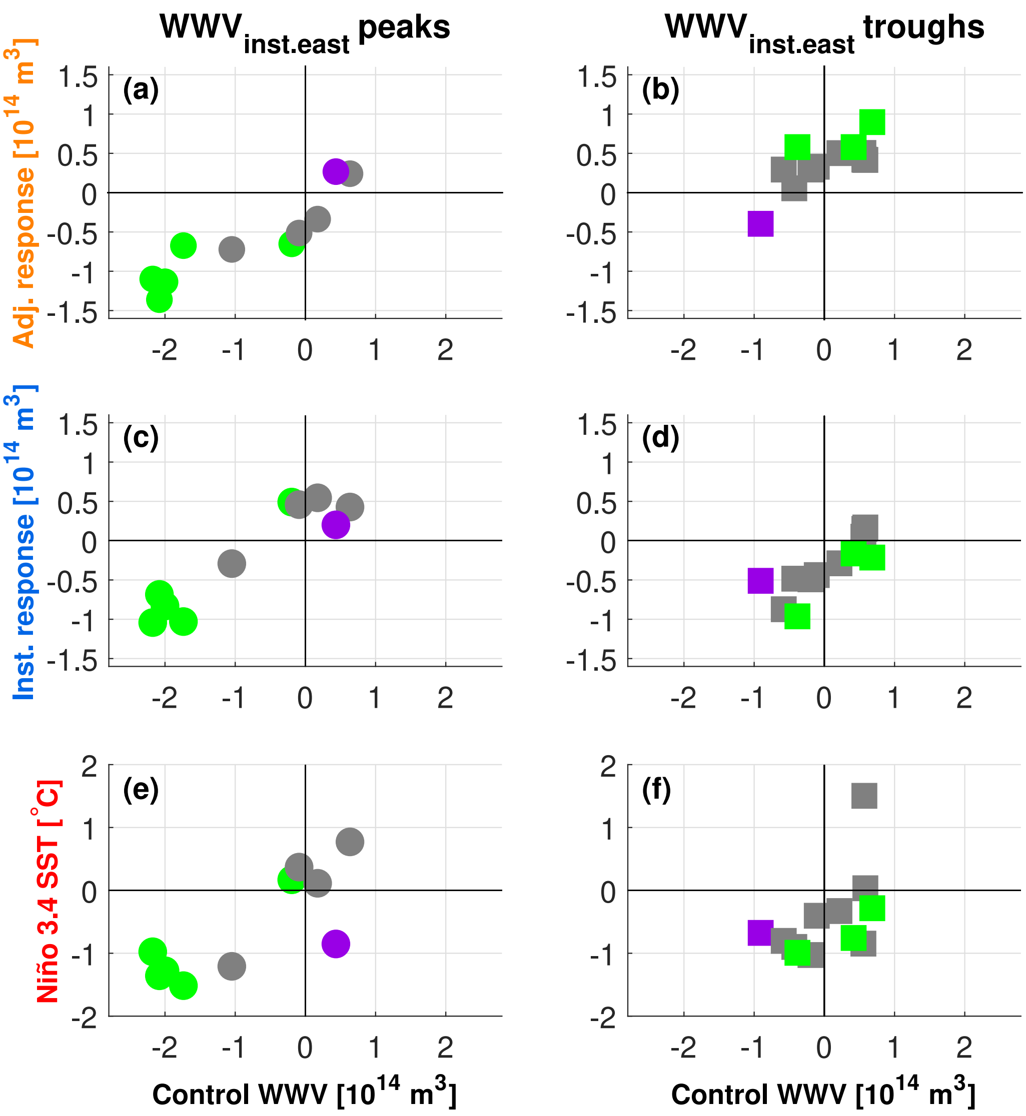

Figure 3.10: Adjusted **(a)**/**(b)** and instantaneous responses **(c)**/**(d)** [10^{14} m^3] (y-axis), and control WWV [10^{14} m^3] (x-axis) 8 months after the WWV$_{inst.east}$ peaks/ troughs. **(e)**/**(f)** Niño 3.4 SST anomaly [°C] 12 months after the WWV$_{inst.east}$ peaks/troughs. Green, gray and purple dots and squares refer to the transitioning, neutral and persistent simulations respectively.

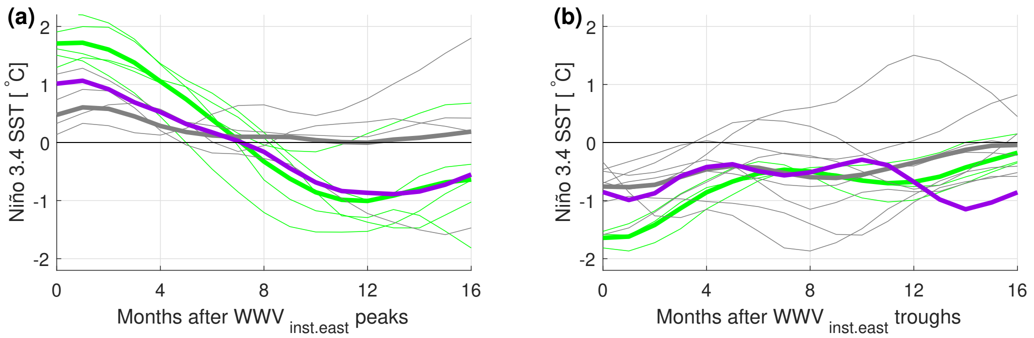

Figure 3.11: (a)/(b) Niño 3.4 SST [°C] after each transitioning (green lines), neutral (gray lines) and persistent (purple lines) $\mathrm{WWV}_{inst.east}$ peaks/troughs. Thick green/gray/purple lines give the averaged of the thin green/gray/purple lines.

b) $\mathbf{WWV}_{inst.east}$ troughs

The average adjusted recharge of the transitioning trough simulations 8 months after the $\mathrm{WWV}_{inst.east}$ troughs ($0.69 \cdot 10^{14}\ m^3$, green squares, Fig. 3.10b) is around 31% smaller than the average adjusted discharge of the transitioning peak simulations (green dots Fig. 3.10a). While adjusted and instantaneous responses of the transitioning peak simulations act together to discharge the WWV 8 months after the $\mathrm{WWV}_{inst.east}$ peaks, there is a destructive interference between the instantaneous response 8 months after the transitioning troughs (on average $-0.45 \cdot 10^{14}\ m^3$, green squares Fig. 3.10d) and the adjusted recharge (green squares in Fig. 3.10b and d). It follows that, the average control WWV recharge 8 months after the equatorial easterly forcing of the adjusted $\mathrm{WWV}_{inst.east}$ troughs ($0.24 \cdot 10^{14}\ m^3$) has a magnitude that is approximately 15% of the size of the average control WWV discharge found 8 months after the equatorial westerly forcing of the adjusted $\mathrm{WWV}_{inst.east}$ peaks. This suggests that the adjusted recharge of the adjusted trough simulations 8 months after the $\mathrm{WWV}_{inst.east}$ troughs is not strong enough to change the system towards warmer SSTs (Fig. 3.10b) and westerly winds, to instantaneously recharge the WWV. Consistently, the southward shift of easterly winds is not as prominent after La Niña events as it is the southward shift of westerly winds after El Niño events (McGregor et al., 2013). The system does not overcome its cool state (green lines, Fig. 3.11b), and hence, 12 months after the transitioning $\mathrm{WWV}_{inst.east}$ troughs the Niño 3.4 SST is on average -0.76 °C. The adjusted response 8 months after the neutral WWV$_{inst.east}$ troughs has a similar low recharge ($0.35 \cdot 10^{14} m^3$, gray squares Fig. 3.10b) compared to the neutral peaks discharge; and similar to the neutral WWV$_{inst.east}$ peaks the instantaneous response 8 months after the gray WWV$_{inst.east}$ troughs has a different sign to the adjusted response ($-0.28 \cdot 10^{14}\ m^3$, gray squares Fig. 3.10d). Consequently, the control WWV almost cancels out (on average $-0.07 \cdot 10^{14}\ m^3$, gray squares Fig. 3.10b and d) and leaves the system on average to not clearly follow any ENSO state 12 months after the WWV$_{inst.east}$ troughs forcing (Niño 3.4 SST= -0.36 °C, gray squares Fig. 3.10f, gray lines Fig. 3.11b).

3.8 Summary and Discussion

This study uses shallow water model (SWM) simulations to categorize the adjusted WWV responses following the strongest equatorial Pacific westerly/easterly wind stress between 1980 and 2016. As in Chapter 2 (Neske and McGregor, 2018), the adjusted WWV component is the WWV changes that are driven by Rossby waves (RWs) and their reflection into the WWV region at the western boundary (McGregor et al., 2016). The importance of understanding the adjusted response arises as it is the slowly evolving component of WWV changes that is responsible for the longer lead time relationship to ENSO SSTs (Neske and McGregor, 2018). Three categories of adjusted responses were then defined and utilized, these were: (i) transitioning adjusted responses (e.g. equatorial westerly wind stress is followed by an adjusted discharge); (ii) neutral adjusted responses (e.g. equatorial wind stress is followed by little to no adjusted recharge or discharge); and (iii) persistent adjusted responses (e.g. equatorial westerly wind stress followed by an adjusted WWV recharge). Traditional conceptual models (e.g. Suarez and Schopf, 1988, Jin, 1997, Wang, 2001) lead us to expect that strong equatorial westerly (easterly) winds during warm (cold) phases of ENSO initiate strong RWs which eventually lead to strong transitioning adjusted discharges (recharges), conditioning the system for a change in ENSO phase. Recent findings, however, show that the STD of the instantaneous WWV (predominantly consisting of the wind-forced Kelvin waves (KWs), correlation to equatorial wind stress=0.86, Fig. 2a) increased by 15% from pre-to post-2000 period, while the STD of the adjusted WWV decreased by 44% at the same time (Neske and McGregor, 2018). Thus, our study seeks to better understand what is driving the recent WWV changes as they are clearly at odds with traditional theories that link equatorial wind stress to the adjusted response.

a) Categorized adjusted WWV responses and their pre- and post-2000 importance

We analyzed the 3-month forcing periods of anomalous equatorial wind stress that has led to the strongest $WWV_{inst.east}$ (instantaneous WWV response east of 200°E, correlation to equatorial wind stress=0.92) peaks and troughs (Fig. 3.2a). These simulations show that only 35% of these strong anomalous equatorial wind stresses are followed by the transitioning adjusted responses that would be expected from ENSO theory (green simulations, Fig. 3.2). The remaining identified strong anomalous equatorial wind stresses are followed by a neutral adjusted response (56%; gray simulations, Fig. 3.2) or by a persistent adjusted response (9%; purple simulations, Fig. 3.2). Moreover, during the pre-2000 period 50% (6/12) of the strongest equatorial winds are followed by transitioning adjusted responses, and this reduces to only 18 % (2/11) for the post-2000 period. As such, the post-2000 period is dominated by the neutral adjusted responses that have little to no adjusted re- and discharge of WWV (Fig. 3.2). Consequently, this finding is consistent with the post-2000 decline in adjusted WWV STD reported by Neske and McGregor (2018) (Chapter 2).

b) Dynamical differences between (i) transitioning, and (ii) neutral adjusted responses

The dynamical differences between transitioning and neutral responses are linked to the differences in wind stress patterns. The average neutral wind stresses are shown to have a latitudinally broader and longitudinally narrower extent than the average transitioning wind stress forcing (Fig. 3.3). We then used a series of idealized wind forced SWM experiments to further show that the negligible adjusted WWV response of the neutral simulations is primarily caused by the different latitudinal structure, which includes zonal wind stresses that are latitudinally broader and have a northward displacement of the maximum zonal wind stresses. This latitudinal difference creates a weaker wind stress curl equatorward of around +/-8° latitude, which diminishes the Ekman pumping and leads to a weaker RW signal when compared to the adjusted transitioning simulations (Fig. 3.5-3.8). The latitudinal differences between the average forcing of the transitioning and neutral simulations can be explained by looking at wind events, as each identified neutral forcing period displays a significant higher ratio of off-equatorial to equatorial wind events than seen in each single transitioning forcing period (Fig. 3.9).

We further show that the differences in: (i) WWV magnitude; and (ii) pycnocline spatial patterns among the transitioning, neutral and persistent simulations of the SWM are largely consistent when repeating these simulations with the more comprehensive global ocean sea ice model GFDL-MOM025 (Fig. A3.2). Consequently, we conclude that the results presented in this study are not significantly impacted by the simplicity of the ocean model utilized.

The underlying average SSTA patterns during the transitioning (neutral) forcing periods are similar to EP (CP)-like ENSO SSTAs (Fig. 3.4) with patterns similar as shown for instance by McPhaden et al. (2011). Consistent with our finding of strong discharge (neutral) adjusted responses forced during EP- (CP-) like El Niño SSTAs, Singh and Delcroix (2013) find an overall poleward mass transport during EP El Niños but not during CP El Niños. While our study links the neutral adjusted response to weak RWs, Singh and Delcroix (2013) link the absence of mass transports during CP El Niños to a compensating effect of a poleward (equatorward) transport in the western (eastern) Pacific.

c) ENSO asymmetry

Recent research has demonstrated that the boreal WWV_{west} (WWV_{west} was shown to be closely linked to the adjusted response, Fig. 3.1d and WWV_{west}/the adjusted response has been shown by Izumo et al. (2019)/Neske and McGregor (2018) to include the long-term lead time to ENSO SSTA) discharge is a better predictor for La Niña events than the boreal WWVwest recharge is for El Niño events (Planton et al., 2018). Planton et al. (2018) partially linked this asymmetry in predictability to the asymmetry in WWV_{west} that shows stronger discharges 13 months before a La Niña event compared to recharges 13 months before an El Niño event. Similarly, Neske and McGregor (2018) show stronger magnitudes of the adjusted discharge compared to the adjusted recharge. Planton et al. (2018) linked this difference in re- and discharge magnitudes to stronger westerly equatorial wind stress during El Niño phases compared to easterly wind stress during La Niña phases which can be linked to: (i) stronger (weaker) positive (negative) SSTAs during El Niño (La Niña) events; and (ii) non-linearities with a given positive SSTA during El Niño leads to stronger equatorial westerly wind anomalies than negative SSTA would lead to equatorial easterly wind anomalies (e.g. Frauen and Dommenget, 2010, Dommenget et al., 2013, DiNezio and Deser, 2014). Further to this, we demonstrate a wind stress curl difference between the forcing periods during El Niños compared to those during La Niñas which adds to the adjusted re- and discharge asymmetry: 45% of the strongest 3-month equatorial westerly forcing periods have a strong wind stress curl that leads to a strong adjusted discharge (green simulations, Fig. 3.2a), while this is the case for only 25% of the strongest 3-month equatorial easterly forcing periods and their associated adjusted recharge (green simulations, Fig. 3.1b). Consistently, the delayed thermocline feedback that is from the traditional ENSO view thought to transition the ENSO phase (Suarez and Schopf, 1988, Battisti and Hirst, 1989, Jin, 1997) is stronger (weaker) during El Niño (La Niña) events (Guan et al., 2019).

Additionally, in agreement with our result, Neske and McGregor (2018) (Chapter 2) show that the discharged (recharged) phase of WWV is dominated by the adjusted (instantaneous) contribution; and we explain this difference by the fact that the stronger wind stress curl patterns are more (less) often found during equatorial westerly (easterly) wind periods. Thus, the westerly (easterly) wind stress of the

$WWV_{inst.east}$ peaks (troughs) is leading more frequently to a transitioning (neutral) adjusted response, and as a consequence the discharge process is dominated by the adjusted response while the recharge process is largely due to the instantaneous response.

Our findings of the wind stress curl strength asymmetry together with the mentioned findings of previous studies serve as an explanation for the asymmetry in phase change with El Niños having a stronger tendency to be followed by La Niñas than vice versa (e.g. Kessler, 2002, Larkin and Harrison, 2002) by explaining the asymmetry of re- and discharged WWV phases. We note that beside re- and discharge asymmetry other mechanisms are at work adding to the asymmetry in phase change transition: For instance (i) the non-linearities between subsurface temperature gradient and thermocline depth (DiNezio and Deser, 2014); or (ii) the stronger (weaker) westward (eastward) currents during El Niño (La Niña) conditions induced by wind stress non-linearities (Clarke and Zhang, 2019).

d) ENSO precursor

We finally aimed to understand the role of the transitioning vs. neutral adjusted responses as ENSO precursors. On average, the neutral simulations are followed by a negligible control WWV (control WWV is the sum of adjusted and instantaneous responses, Fig. 3.1c) 8 months after the strongest equatorial wind stresses. As such, the neutral simulations appear to provide little potential for longer term SST predictability (Fig. 3.10 and 3.11).

On the other hand, the average of the transitioning westerly adjusted discharges is followed by a clear control WWV discharge 8 months after the strongest equatorial westerly wind forcing. This strong WWV discharge is due to strong contributions from both the adjusted and instantaneous WWV components. Further to this, the westerly adjusted discharges are on average followed by La Niña-like SSTs 12 months after the wind forcing (Fig. 3.10 and 3.11). In contrast, the average transitioning adjusted recharge 8 months after the forcing is 31% smaller than the discharge that followed the westerly adjusted discharges. This weaker adjusted recharge is accompanied by an instantaneous response of opposite sign that almost totally cancels out the adjusted WWV recharge. Consequently, the system persists in cool eastern/central Pacific SST anomalies (Fig. 3.10 and 3.11).

This differences in ESNO precursor between equatorial westerlies and easterlies with strong wind stress curls suggests that the transitioning adjusted discharge following the equatorial westerlies is strong enough to cool the eastern Pacific SST via the thermocline feedback; and this cool SST anomaly excites easterlies and an associated instantaneous discharge that constructively interferes with the adjusted discharge. Both of which leave the system to a state which favors the development of a La Niña event. We note, however, that this is contradictory to the study of Izumo et al. (2019) which indicates that the forced RWs that have reflected into KWs play hardly any role in the eastern Pacific.

In contrast, the transitioning adjusted recharge following the equatorial easterlies is not strong enough to warm the eastern Pacific SST, and the cool SST still excites easterlies which lead to the instantaneous discharge compensating the adjusted recharge and not favoring an El Niño event.

Consistently with our study, Guan et al. (2019) show that the thermocline feedback during the decaying phases of La Niña events is more than twice as strong as those during the decaying phases of El Niño events, which means that the easterlies persists over a longer time during La Niñas than the westerlies during El Niños and this hinders the decaying of La Niñas. Moreover, McGregor et al. (2013) find a clear southward shift of westerly wind events after El Niño events leaving easterlies to dominate the equatorial system and this southward shift could not be found for the easterlies after La Niña events. The connection between strong adjusted responses and a southward shift, however, is not clear at this stage. All these findings give an explanation for the asymmetry in duration and phase change transition with El Niño events lasting a shorter period and having a stronger tendency to be followed by La Niña events than vice versa (e.g. Kessler, 2002, Larkin and Harrison, 2002, Okumura and Deser, 2010, Guan et al., 2019), as well as they explain why La Niñas are better predictable than El Niños (Luo et al., 2008, DiNezio et al., 2017).

e) Final remarks

To sum up, our work emphasizes the importance of wind stress curl (determined by the ratio of off-equatorial wind events to equatorial wind events) for understanding recent changes in the drivers of WWV variability and the asymmetry of ENSO. The pre- to post-2000 differences in wind stress curl and the wind stress curl asymmetry presented in this paper are in line with the: (i) post-2000 failure of the adjusted WWV contribution being a long-term ENSO SST precursor ($>$ 9 months); and (ii) larger (smaller) adjusted discharge (recharge) magnitudes (as both shown by Neske and McGregor, 2018). All these findings give an explanation for the asymmetry in duration and phase change transition with El Niño events having a stronger tendency to be followed by La Niña events than vice versa (e.g. Kessler, 2002, Larkin and Harrison, 2002, Okumura and Deser, 2010, Guan et al., 2019), as well as they indicate why La Niña events tend to be predictable at longer lead times than El Niño events (Luo et al., 2008, Dommenget et al., 2013, DiNezio et al., 2017).

Future work aims to (i) quantify the amount of strong adjusted responses that are preceded by weak equatorial wind stresses compared to strong equatorial wind stresses; (ii) identify the relative importance of wind stress curls in different regions around the equatorial and off-equatorial Pacific during pre- and post-2000 period; and (iii) understand the importance of RW cancellations excited in different regions around the equatorial Pacific for explaining pre- and post-2000 differences.

Appendix Chapter 3

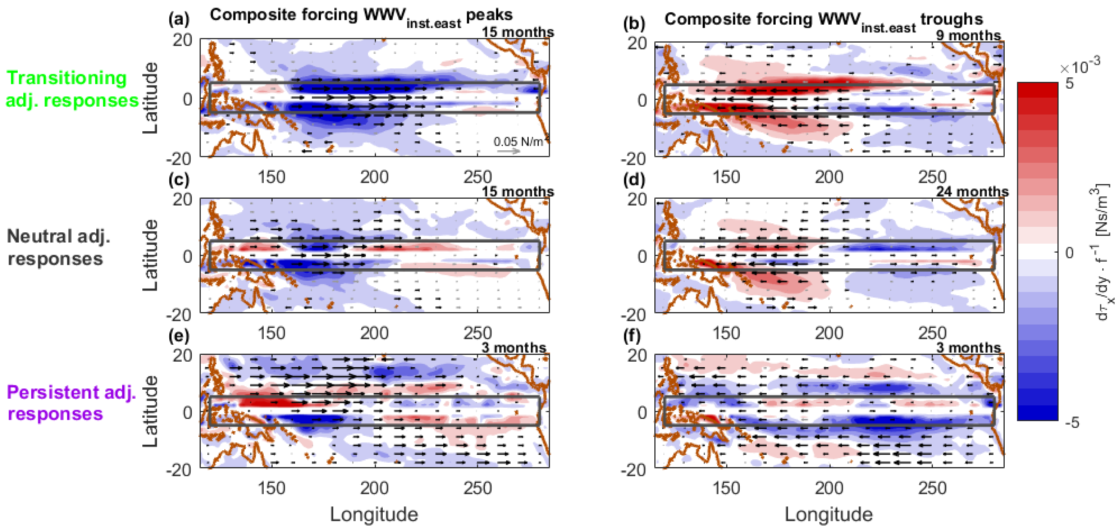

Figure A3.1: Same as Fig. 3.3a-f but the wind stress curl is divided by the Coriolis parameter f $[Ns/m^3]$. The values of located at the equator are set to zero.

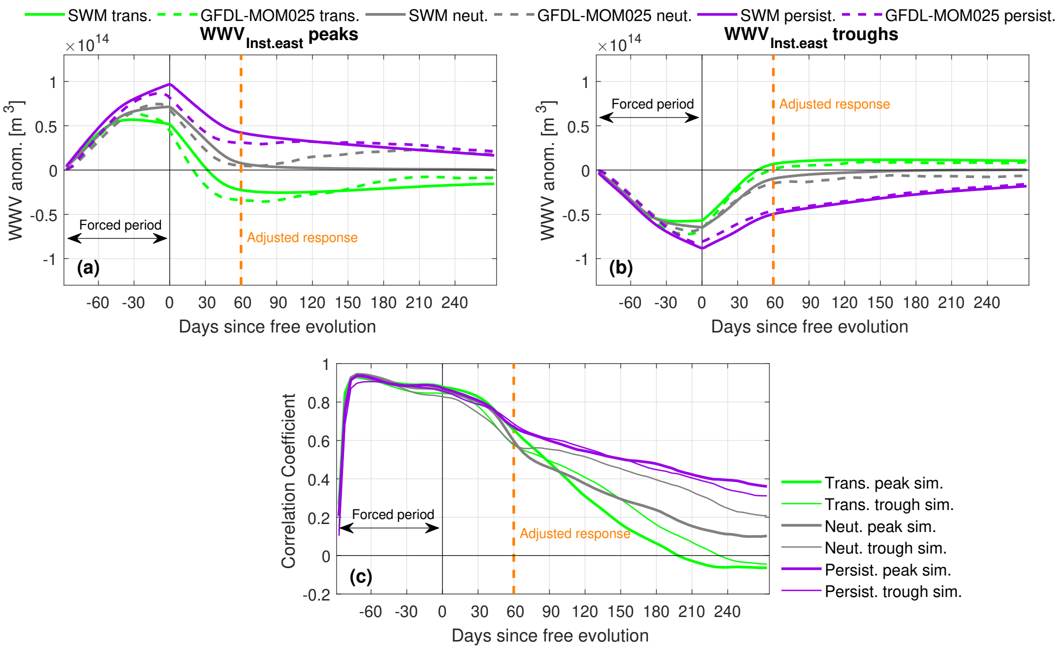

Figure A3.2: **(a)**/**(b)** WWV outcomes $[m^3]$ of the SWM (solid lines) and of the GFDL-MOM025 (dashed lines) forced constantly over the 3-month period by the transitioning (green lines), neutral (gray lines) and persistent (purple lines) composite forcings of the WWV$_{inst.east}$ peaks/troughs (Fig. 3.3). The GFDL-MOM025 runs are forced with wind velocities rather than wind stress as the model takes into account the surface current strength to calculates its own wind stress. For a consistency in forcing these wind stresses are taken to force the SWM for the outcomes of this figure. To calculate the WWV for the GFDL-MOM025 simulations the anomalous 1026 kg/cm^3 isopycnal (approximating the thermocline) depth is calculated by subtracting the 1026 kg/cm^3 isopycnal depth of the solely climatology forced simulation. This is done for five initializations and the average of all five anomalous 1026 kg/cm^3 isopycnals is calculated. **(c)** Spatial correlations between the composite WWV$_{inst.east}$ peak/trough SWM and GFDL-MOM025 transitioning (green thick/thin line), neutral (gray thick/thin line), and persistent (purple thick/thin line) simulations. Spatial correlations are calculated between 15°N and 15°S after the GFDL-MOM025 outcome was linearly interpolated to the SWM grid.

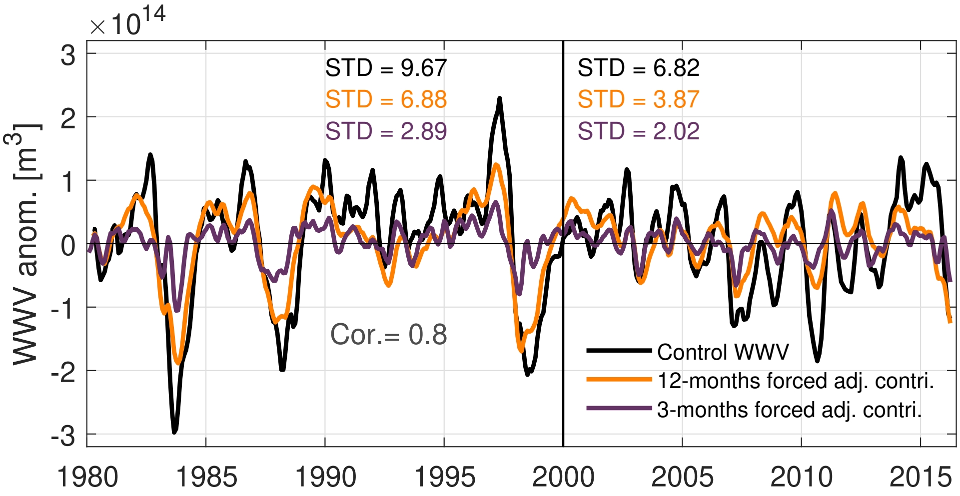

Figure A3.3: Monthly mean WWV outcome [m^3] of the control simulation (black line) and when forcing the SWM over (i) 12 months (orange line, same as in Fig. 3.1c and d), and (ii) 3 months (purple line) before it is left to freely evolve and the average of the third month of the free evolution is taken for each month (adjusted response).The correlation is calculated between the 12-month and 3-month adjusted responses. Pre- and post-2000 STDs are displayed in [10^{13} m^3].

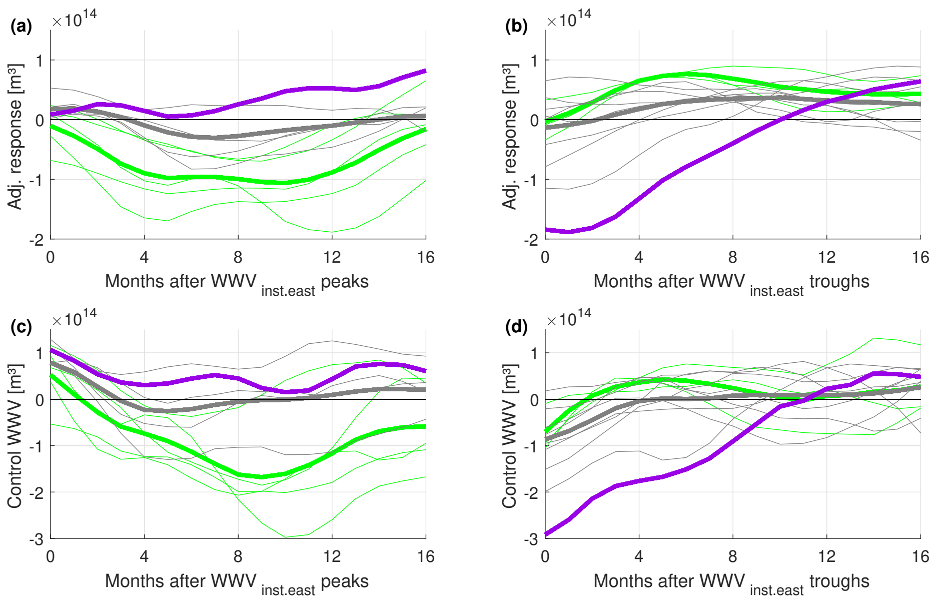

Figure A3.4: Adjusted response [m^3] **(a)**/**(b)** and Control WWV [m^3] **(c)**/**(d)** after the adjusted (green lines), neutral (gray lines) and persistent (purple lines) WWV$_{inst.east}$ peaks/troughs. Thick green/gray/purple lines give the averaged of the thin green/gray/purple lines.

Chapter 4

Drivers of ENSO's post-2000 WWV changes

Preface

This study identifies the drivers which explain the post-2000 decline in adjusted warm water volume (WWV) standard deviation (STD) found by shallow water model simulations. It is important to understand this decline as the adjusted WWV provides long lead times (>6 months) to the El Niño-Southern Oscillation (ENSO) sea surface temperatures (SSTs); and its post-2000 STD decline underpinned: (i) a shortening of the whole WWV/ENSO SST lead time; and (ii) a reduced precursor skill for ENSO SSTs. For this purpose, we built a regression model to obtain the adjusted WWV time series from wind stress curl in multiple boxes across the tropical Pacific. In this model the wind stress curl in each box approximates the Rossby wave signal in that given area. The adjusted WWV of the regression model is highly consistent with the adjusted WWV of the SWM (cor=0.94). We show that the curl STD declines in all regions in the post-2000 period (consistent with Chapter 3); and that this reduction explains around 25% of the total adjusted WWV decline. Furthermore, around 25% of the decline is explained by an increase in frequency in the post-2000 curl time series. The remaining 50% of the adjusted WWV post-2000 decline is explained by cancellations of the Rossby wave signals excited in the different boxes. It is shown that the dominant contribution for explaining the post-2000 adjusted WWV (when considering the curl STD decline, frequency increase and latitudinal cancellation), does not come from the signal of the region of strongest winds in the central Pacific. Rather, this dominant contribution comes from the signal of the region east of it (200-240°E). This region has shown to only produce WWV during eastern Pacific (EP) ENSO SSTs, thus the decline in adjusted WWV is consistent with the post-2000 declined occurrence of EP ENSO events.

4.1 Introduction

The El Niño-Southern Oscillation (ENSO) is the largest source of climate variability on interannual time scales on our planet. It fluctuates between anomalous warm (El Niño) and cool (La Niña) states of the tropical eastern Pacific sea surface temperature (SST) causing distinct changes to the coupled atmosphere. Through atmospheric teleconnections, ENSO's climatic impacts can reach nearly the whole globe (e.g. Trenberth et al., 1998), and these impacts can lead to devastating socioecological consequences (e.g. Glantz et al., 2001, McPhaden et al., 2006). Around 40 decades of intense research have tremendously enhanced our understanding of ENSO, however, the research also reveals the high complexity of ENSO with many details of this phenomenon not being understood to date (e.g. Timmermann et al., 2018, Santoso et al., 2019). As such, it is of high priority to deepen our understanding of ENSO's dynamics, with the ultimate goal of improving its predictability.

After Jin's (1997) recharge-discharge oscillator theory, the Pacific warm water volume (WWV, the volume of water above the thermocline integrated over 120-280°E and 5°N-5°S) is viewed as a precursor for ENSO SST. A recharge (discharge) of WWV leads El Niño (La Niña) events by 1-3 seasons (e.g. Meinen and McPhaden, 2000, McPhaden, 2012, Bunge and Clarke, 2014), which demonstrates that the WWV is a fundamental ingredient of ENSO and its accurate prediction. The WWV is particularly valued over other precursors, as it overcomes the spring predictability persistence barrier of ENSO SST (McPhaden, 2003, 2012, Clarke and Zhang, 2019). Thus, improving our understanding of the WWV is thought to be key for improving understanding of ENSO itself.

In an attempt to better understand the WWV, it has often been divided into its slower Rossby wave and faster Kelvin wave components using various methods. These methods divide the WWV into: (i) Ekman and geostrophic transports (Meinen and McPhaden, 2001, Meinen, 2005, Bosc and Delcroix, 2008); (ii) adjusted wind responses ($>$3 months) and instantaneous wind responses ($<=$3 months) (Neske and McGregor, 2018, Chapter 2 and 3); or into (iii) WWV_{west} (WWV west of

205°E) and WWV_{east} (WWV east of 205°E; Meinen and McPhaden, 2000, Planton et al., 2018, Izumo et al., 2019). Separating the WWV into these two components has been essential in gaining further insight into ENSO's complexity, not possible when considering the WWV as a whole. Neske and McGregor (2018) for example could explain the decline in WWV/ENSO SST lead time from around 3 seasons during the 1980-1999 period to only 1 season during the recent two decades (McPhaden, 2012, Horii et al., 2012, Bunge and Clarke, 2014, Zhang et al., 2019) due to a 44% decline of the Rossby waves driven adjusted WWV response. As such, only the adjusted WWV or similarly the WWV_{west} (Chapter 3) shows precursor skill for ENSO SST at lead times longer than around 2 seasons (Neske and McGregor, 2018, Izumo et al., 2019). Additionally, the adjusted WWV or the WWV_{west} has been shown to be a better predictor for La Niña events than for El Niño events (Chapter 3, Planton et al., 2018).

While all of these studies are valuable for understanding details of ENSO dynamics, none of them directly relate the WWV changes to the wind forcing. For instance, geostrophic velocities are estimates with Sea Level Anomalies (SLAs, which are highly consistent to thermocline depth anomalies, Rebert et al., 1985) that are typically modulated by wave dynamics rather than being related to the wind forcing (e.g. Bosc and Delcroix, 2008). In further detail, the SLAs created by Rossby and Kelvin waves are zonally nearly symmetrical when being forced. Consequently, the meridional geostrophic transports into or out of the WWV region, depending on the zonal gradient of the SLAs, only appear when the waves meet the eastern and western boundaries inducing a strong zonal SLA gradient of one sign. However, the details of where and how the waves are forced is very difficult to recover, as propagation time to the boundary depends on the latitude and longitude of generation.

Traditional ENSO theories (e.g. Suarez and Schopf, 1988, Jin, 1997) link the wind forcing to the WWV changes as follows: The equatorial westerly (easterly) wind stress during El Niño (La Niña) events excites upwelling (downwelling) Rossby waves causing an adjusted discharge (recharge) which conditions the system for an La Niña (El Niño) event. Our previous study (Chapter 3), however, shows that strongest equatorial wind stress cannot always be linked to strong Rossby waves as assumed from these traditional ENSO theories. In particular, the majority of the strongest equatorial winds during warm and cold ENSO phases in the post-2000 period have a weak wind stress curl around the tropical central/western Pacific that results in weak Rossby waves and a negligible induced adjusted WWV response (Chapter 3). This result highlights the importance of considering the wind stress curl, rather than the wind stress, to understand the adjusted WWV. Additionally, the study of Clarke et al. (2007) emphasizes the role of wind stress curl for ENSO dynamics, and they developed with a theoretical derivation of the WWV changes from wind stress curls at 5°N and 5°S (cor=0.85) for the period 1993-2001.

The aim of the present study is to construct a regression model to derive adjusted WWV changes from wind stress curl from 1980-2016. We then intend to use this regression model to examine how the wind stress curl has changed in different regions around the tropical Pacific, and how these changes relate to the post-2000 adjusted WWV decline. Additionally, we examine how: (i) the frequency of the wind stress curl time series; and (ii) the interplay between regions add to the post-2000 adjusted WWV decline. Furthering our understanding of the adjusted WWV formation is key because it is thought that the adjusted WWV needs to overcome a certain threshold as a necessary condition in order to initiate a new ENSO phase (Chapter 3), and being as such a reliable ENSO precursor on lead time >6 months Neske and McGregor (2018).

This study is organized as follows: Section 4.2 describes the methods and data, and is followed by Section 4.3 explaining the adjusted WWV regression model. Section 4.4 then uses the regression model to develop our understanding of the pre- to post-2000 changes of the WWV precursor, while the main results are validated by a Rossby wave projection model. We examine the consistency between equatorial wind stress and its curl in the different regions around the tropical Pacific in Section 4.5. Finally, this study ends with summary and conclusions (Section 4.6).

4.2 Methods and Data

4.2.1 Wind stress data

We use daily average anomalous surface wind stresses (1980 to May 2016) of the European Centre of Medium-Range Weather Forecast (ERA-interim Dee and Uppala, 2009). The anomalous stresses were obtained from the 6-hourly 10 m surface winds which were first converted to wind stress (using the quadratic stress law) and then averaged to a daily output, prior to the long-term seasonal cycle being removed. We then force our regression model (Section 4.3) by the monthly mean curl of the anomalous zonal wind stress ($\frac{\partial \tau_x}{\partial y}$, where τ_x is the zonal wind stress).

4.2.2 The WWV's adjusted and instantaneous contributions

To understand the regression model of the adjusted WWV contribution, we briefly explain how the WWV was originally divided into adjusted and instantaneous wind responses. We follow the method of Neske and McGregor (2018) who used a 1.5-layer shallow water model forced by anomalous ERA-interim wind stress (see Neske and McGregor (2018) or Appendix Chapter 2 Text A1.1 for details about the model).

Adjusted contribution
To obtain the adjusted WWV responses we conduct hindcast experiments initialized on the first day of each month between January 1980 and March 2016 (as illustrated in Fig. 4.1a). For each of these hindcasts, the model is forced during a one year spin up period with anomalous wind stresses, after which time the SWM is left to freely evolve (no forcing, turquoise line, Fig. 4.1a). The adjusted contribution (Fig. 4.1b) is then the third month average of the free evolution (Fig. 4.1a). This adjusted contribution is largely consistent with WWV changes due to Rossby waves (Neske and McGregor, 2018) as wind stress forced Kelvin waves reach the eastern Pacific boundary within 1-3 months where they take the majority of their signal poleward (McGregor et al., 2016).

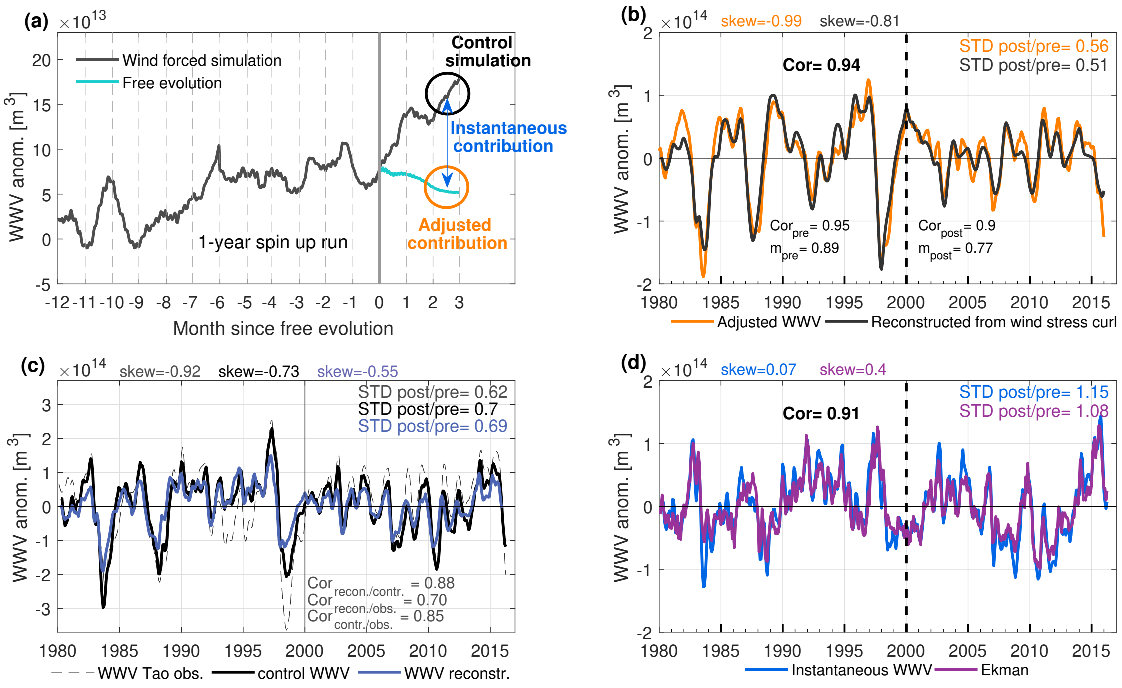

Figure 4.1: **(a)** Sketched example of obtaining (i) the control warm water volume (WWV), and (ii) the control WWV's adjusted and instantaneous contributions. The 1-year spin up run is initialized on 07/01/1982. **(b)** Adjusted contribution (orange line) [m^3] and the modeled adjusted contribution of the regression model (gray line) [m^3]. STD is the standard deviation, skew stands for skewness, cor gives the correlation and m gives the regression coefficient between both time series. **(c)** WWV anomaly of (black line) the SWM control simulation [m^3]; (blue line) the sum of the regressed adjusted contribution in **(b)** and the Ekman WWV in **(d)** [m^3]; and (dashed gray line) observations [m^3]. **(d)** Instantaneous contribution (blue line) [m^3], and the monthly mean meridional Ekman transport anomalies entering the WWV box at the meridional boundaries (5°N and 5°S, purple line) [m^3]. Figures **(a)** and **(d)** are adapted from Neske and McGregor (2018).

Control WWV

The control simulation has the same one year spin up as above, but after this period the model continues to be forced for the three months that are unforced for the adjusted contribution (black circle, Fig. 4.1a). The monthly mean control WWV changes are highly correlated (cor= 0.86) with observations (Smith, 1995, available at https://www.pmel.noaa.gov/tao/wwv/data/), and both modelled and observed WWV show a similar pre- to post-2000 STD decline (Fig. 4.1c).

Instantaneous contribution

The instantaneous contribution is calculated as the difference between the control and the adjusted WWV (Fig. 4.1a). Thus, it predominantly consists of the wind forced KW signal in the eastern Pacific and is highly consistent with WWV changes due to Ekman transports (Fig. 4.1d). Ekman transport anomalies (V_{Ekman} are calculated according to $V_{Ekman} = \frac{-\tau_x}{\rho f}$, where τ_x is the zonal wind stress anomalies (from ERA-interim winds), ρ is the upper ocean density taken as constant (1023 kg/m^3) and f is the Coriolis parameter. WWV changes were calculated by integrating the meridional transports over 120°E-80°W at 5°N, and over 150°E-80°W at 5°S (to exclude the area over land).

4.2.3 Rossby wave projection model

To examine the robustness of the regression model results, the main outcomes of the regression model are also compared to the outcome of a Rossby wave projection model (we use the same linear ocean model as McGregor et al. (2016)). As with the SWM, the Rossby wave projection model has an active upper layer which is separated from the motionless lower layer by an interface representing the thermocline depth. The model domain ranges from 40°N to 40 °S, and 140°E to 280°E with a 0.25° grid spacing. The dynamics of the upper layer follow the linear shallow water equations on an equatorial β plane (i.e. $f = \beta y$, with f being the Coriolis parameter, and y being the meridional distance). The non-dimensionalized equations under the low frequency, large-zonal scale approximation are:

$$\frac{\partial u}{\partial t} - yv + \frac{\partial \eta}{\partial x} = X; \tag{4.1}$$

$$yu + \frac{\partial \eta}{\partial y} = 0; \tag{4.2}$$

$$\frac{\partial \eta}{\partial t} + \frac{\partial \eta}{\partial x} + \frac{\partial \eta}{\partial y} = 0; \tag{4.3}$$

where u and v are the zonal and meridional velocities respectively, η is the model thermocline depth, t is time, and x and y are zonal and meridional distances respectively. The non-dimensionalisation is obtained by using: $u' = uc$, $v' = vc(\frac{c}{\beta})^{0.5}$, $x' = xL$, $y' = y(\frac{c}{\beta})^{0.5}$, $t' = (L/c)$, $\eta' = H\eta$, and $X' = \tau^x(\rho H)^{-1}$ meaning that the zonal wind stress forcing (τ^x) is applied as body force. Here, L is the basin zonal width (≈15540 km), c is the gravity wave speed (2.8m/s), H is the upper mean depth (300 m) and ρ is the density (1000 kg/m^3). The non-dimensionalised equations can be solved with the following solution (e.g. see Clarke, 2008):

$$\eta(x,t) = q_0(x,t)\psi_0 + \sum_{n=1}^{\infty} q_n(x,t)\left[\frac{\psi_{n+1}}{\sqrt{(n+1)}} + \frac{\psi_{n-1}}{\sqrt{(n)}}\right]; \tag{4.4}$$

$$u(x,t) = q_0(x,t)\psi_0 + \sum_{n=1}^{\infty} q_n(x,t)\left[\frac{\psi_{n+1}}{\sqrt{(n+1)}} - \frac{\psi_{n-1}}{\sqrt{(n)}}\right]; \tag{4.5}$$

$$v(x,t) = \sum_{n=0}^{\infty} v_n(x,t)\psi_n; \tag{4.6}$$

where ψ_n stands for the Hermite functions which describe the meridional structure of the response:

$$\psi_n = \frac{e^{\frac{-y^2}{2}} H_n(y)}{\sqrt{2^n n! \sqrt{\pi}}}; \tag{4.7}$$

with H_n being the Hermite Polynomial of order n (e.g. see Clarke, 2008 for H_n).

The variable q_0 is the amplitude of the forced Kelvin wave, and q_n is the amplitude of the nth meridional mode forced Rossby wave. The solutions for the Kelvin and Rossby waves amplitudes are provided below and explained in more detail in McGregor et al. (2016).

$$\frac{\partial q_0}{\partial t} + \frac{\partial q_0}{\partial x} = \frac{1}{2}\int_{-\infty}^{\infty} X\psi_0 dy \tag{4.8}$$

$$(2n+1)\frac{\partial q_n}{\partial t} - \frac{\partial q_n}{\partial x} = \frac{1}{2}\int_{-\infty}^{\infty} \sqrt{n+1}nX\psi_{n+1} - \sqrt{n}(n+1)\psi_{n-1}dy \tag{4.9}$$

With the Rossby wave amplitude set to unity, it can be seen that the first 6 meridional modes are sufficient when considering thermocline changes between 10°N and 10°S (Fig. 4.2).

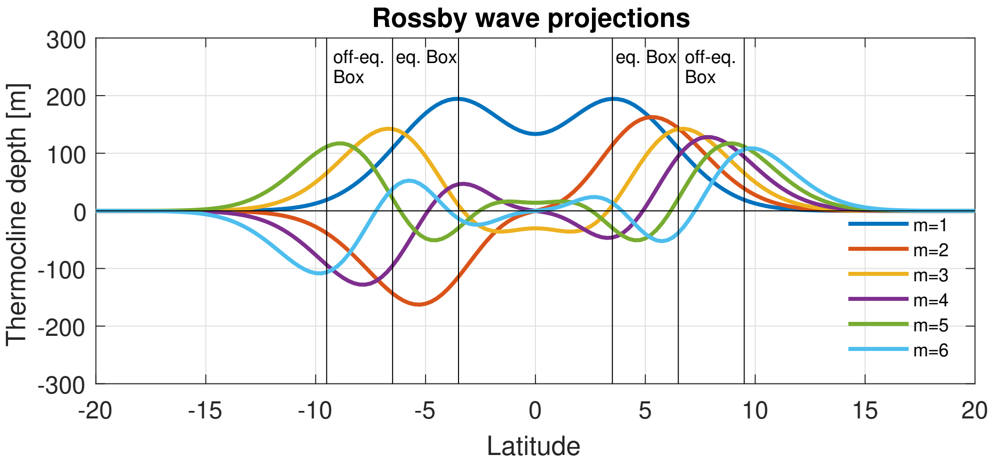

Figure 4.2: First 6 meridional Rossby wave modes when the amplitude is set to unity. Vertical black lines mark the latitudinal boundaries of the equatorial and off-equatorial boxes of the regression model in Fig. 4.3a.

4.2.4 Spectral analysis

To understand the influence of the frequency of the wind stress curls on the adjusted WWV decline, we calculate a power density spectrum with the Welch's method using a rectangular window with no overlap.

If not stated otherwise, all time series have been smoothed by a 3-month running average.

4.3 Adjusted WWV regression model

As shown in Chapter 3, it is the curl of the zonal wind stress rather than the wind stress itself which is crucial in determining the strength and sign of the forced Rossby waves. Thus, to reconstruct the adjusted WWV, we estimate the Rossby wave signal using the curl of the zonal wind stress in three different longitudinal regions that span the tropical Pacific (Fig. 4.3a). These regions are: (i) Region 1 located between 160-200°E; (ii) Region 2 located between 200-240°E; and (iii) Region 3 located between 240-280°E. While regions 1 and 2 are separated into two equatorial (3.5-6.5°N and 3.5-6.5°S) and two off-equatorial boxes (6.5-9.5°N and 6.5-9.5°S), the model exists of only one equatorial box in Region 3 (3.5-6.5°S) (Fig. 4.3a).

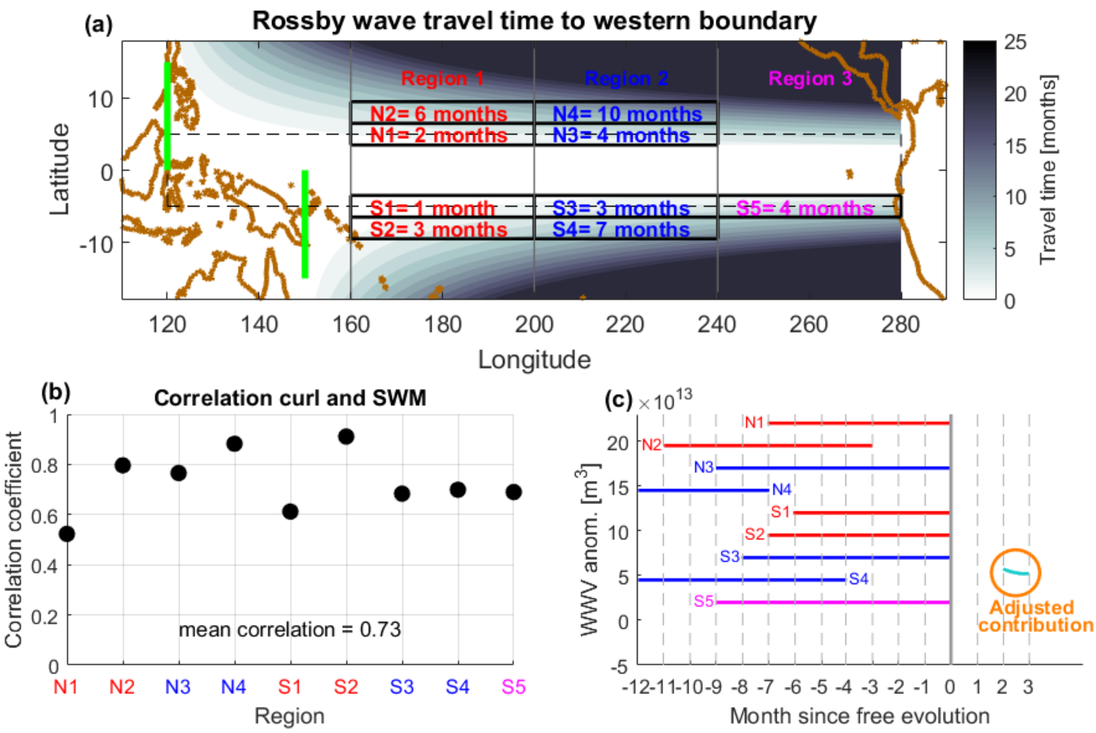

Figure 4.3: **(a)** Overview of the Rossby wave travel time [months] of the equatorial and off-equatorial boxes of the regression model in three longitudinal Regions to the western boundaries (vertical green lines). **(b)** Correlation between the wind stress curl and the direct SWM thermocline output of the different boxes shown in **(a)**. **(c)** Integration times of the curls of the different boxes used for the regression model (Equation 4.10) to obtain the adjusted contribution three months later [m^3].

Regions were selected based on the results of Chapter 3, where the composite of the strongest equatorial winds with a strong adjusted response showed maximum wind stress curls between 3.5-6.5° latitude in Region 1 and Region 2 (Chapter 3, Fig. 3.4).In contrast, the composite of the strongest equatorial winds with a weak adjusted response shows weaker (approximately zero) wind stress curl in the equatorial and off-equatorial areas of Region 1 (Region 2) (Chapter 3, Fig. 3.4). The equatorial box of Region 3 is added to improve consistency between the SWM adjusted response and the outcome of the regression model.

To validate the use of the curl in a given box as a proxy for the thermocline depth changes induced by the forced Rossby wave signal in that box, we calculate the direct SWM thermocline response to wind forcing in each region. This time series of the direct SWM thermocline response is obtained by forcing the SWM with the monthly mean wind stress anomalies over one day for each month from 1980-2016. The correlation between the direct SWM thermocline depth and the wind stress curl time series of each box is on average 0.73 (Fig. 4.3b). For the equatorial boxes we have extended the regions for the curls for the regression model by 2° equatorwards (i.e. between 1.5-6.5°N and 1.5-6.5°S) as this results in a higher consistency between the direct thermocline depth of the SWM and the curl. This higher consistency can be explained by the fact, that winds of near-equatorial latitudes can have Rossby wave projections influencing higher latitudes (see Rossby wave mode 1 in Fig. 4.2). We note, that the average correlation between wind stress curl and the direct SWM thermocline depth is higher for the off-equatorial boxes (cor=0.82) as the direct SWM thermocline depth time series also includes the forced Kelvin wave signal influencing the Rossby wave signal of the equatorial boxes. However, this result is in general agreement with findings from Chapter 3, showing that the wind stress curl is a good proxy for the Rossby wave signal in a given box.

The monthly mean adjusted WWV is then estimated as follows:

$$
\begin{aligned}
WWV_{adj}(t+3) = (&\int_{t=-7}^{t=0} curl_{N1}dt + 0.28 \cdot \int_{t=-11}^{t=-3} curl_{N2}dt + \int_{t=-9}^{t=0} curl_{N3}dt \\
&+ 0.28 \cdot \int_{t=-12}^{t=-7} curl_{N4}dt + \int_{t=-6}^{t=0} curl_{S1}dt + 0.28 \cdot \int_{t=-7}^{t=0} curl_{S2}dt \\
&+ \int_{t=-8}^{t=0} curl_{S3}dt + 0.28 \cdot \int_{t=-12}^{t=-4} curl_{S4}dt + \int_{t=-9}^{t=0} curl_{S5}dt) \cdot m_{regr.};
\end{aligned}
\tag{4.10}
$$

where "m_{regr}" is a regression coefficient, and "curl" is the monthly mean wind stress curl averaged over each single box (N1-N4 and S1-S5, note that this curl is extended by 2° equatorwards for the equatorial boxes) estimating the Rossby wave signal. The integration times of the curls in Equation 4.10 are determined by the average Rossby wave travel time to the western boundaries of each box (Fig. 4.3a and c, see Appendix Chapter 4, Text A4.1 for details about the travel time calculations). The western boundaries are defined at 120°E and 150°E for the northern and southern Hemispheres respectively (green lines, 4.3a).

As the adjusted response at month=3 is forced by the winds prevailed more than 3 months ago (Fig. 4.1a), the integration time for the equatorial boxes ends at month 0 (t=0) (Fig. 4.3c). For the equatorial boxes with a 4-month travel time to the western boundary (box N3 and S5), the integration time actually must end at month -1 so that the Rossby wave signal is accounted for the adjusted response 4 months later (i.e. at month 3, Fig 4.3c) after being reflected into the WWV region. However, the Rossby waves already influence the WWV signal although not yet being reflected (Fig. A4.1) and thus, the integration time for box N3 and S5 in this regression model also ends at month 0 (Fig. 4.3c, Equation 4.10). Each curl of the equatorial boxes is then integrated for 8 months after meeting the western boundary to give the optimal fit between the regressed and SWM adjusted contributions. For instance, the curl of box N1 meets the western boundary after 2 months, so that after three months of free evolution it is integrated for further 7 months (Fig. 4.3c).

For the off-equatorial boxes the integration time ends when the Rossby waves have met the western boundaries and reflect into the WWV region. For instance, the integration time for box N4 ends at month -7 and therefore, the 10-month Rossby wave travel time to the western boundary is accounted for the adjusted response at month 3 (Fig. 4.3c). As with the equatorial boxes, each off-equatorial box is then integrated over a length of 8 months after meeting the western boundaries (but maximal to month -12 as the adjusted signal is forced by a 1-year spin up run, see Fig. 4.1a, and Fig. 4.3c). Further, the weak Rossby wave reflection efficiency of the off-equatorial boxes (which is around 28% lower than that of the equatorial boxes, see Kessler (1991)) is considered in the regression model by multiplying each integrated curl of the off-equatorial boxes by 0.28 (see Equation 4.10).

4.3.1 Validation of the reconstructed adjusted WWV signal

The reconstructed adjusted WWV signal is highly consistent with the SWM adjusted WWV as shown by a correlation of 0.94 between both time series, and a similar pre-to post-2000 STD decline of 0.51/0.56 for the regressed/SWM adjusted response (Fig. 4.1b). Moreover, the correlation (regression coefficient) between the reconstructed and the SWM adjusted WWV are 0.95 (0.89) and 0.9 (0.77) for pre- and post-2000 period respectively. Additionally, both time series have a similarly strong negative skewness of -0.81/-0.99 for the regressed/SWM adjusted WWV. Thus, this validation shows that it is possible to use this regression model to further understand the post-2000 adjusted WWV decline.

Adding additional boxes to Region 3 or to the west of Region 1 does not enhance the consistency between the regressed and SWM adjusted WWV (not shown here). Similarly, adding boxes to higher latitudes does not improve the regression model, which can be explained by the low Rossby wave reflection efficiency at latitudes higher than around 8° (Kessler, 1991). We note that we chose an integration time for the Rossby wave signal in each box of 8 months after meeting the western boundary because this gives the optimal fit to the SWM adjusted contribution, however, shortening the integration time for instance to 5 months, still results in a high correlation of 0.89 between the regressed and the SWM adjusted WWV.

We note, that adding the following physics to the regression model does not enhance the consistency between the regressed and SWM adjusted contributions (not shown here): (i) a damping rate due to dissipation of the Rossby waves along their course of travel; or (ii) the strengthening of the Rossby wave signal from equatorial boxes due to western boundary reflection; and (iii) and a damping rate of the reflected Kelvin wave signal due to eastern boundary reflection of all boxes during the 8 months of integration (for (ii) and (iii) see for instance McGregor et al., 2016, their Fig. 6). The reason why considering these physics does not improve the outcome of the regression model might lie in the experimental design of how the adjusted WWV is obtained from the SWM: The wind forced KWs can influence the adjusted contribution even after they have met the eastern boundary (Fig. A4.1), and this influence might dominate a damping rate.

4.4 Understanding the details of the WWV precursor

When adding the instantaneous WWV estimated from Ekman (i.e. estimated from wind stress, Fig. 4.1d, Subsection 4.2.2) to the adjusted WWV estimated with the wind stress curl regression model, we find that the sum is highly correlated to the SWM control (cor=0.88) and observed WWV (cor=0.7, Fig. 4.1c). The reconstructed whole WWV also displays a moderate negative skewness (-0.55) which is around 25%/41% weaker than the negative skewness of the control (-0.73)/observed WWV (-0.92). The 41% weaker skewness of the reconstructed WWV compared to the observed WWV may at least partially be due to: (i) errors in the used wind stress product (e.g. McGregor et al., 2012a); and (ii) the observed WWV containing the signal of higher baroclinic modes. However, the ratio of post- to pre-2000 STD decline of the whole reconstructed WWV signal (0.69) is highly consistent with those of the control (0.7) and observed WWVs (0.62, Fig. 4.1c).

As the instantaneous contribution shows no post-2000 STD decline, and additionally has no negative skewness (Fig. 4.1d), it is clear that the post-2000 STD decline of the control WWV and its strong negative skewness stem solely from the characteristics of the adjusted contribution. Thus, in the following we examine the reasons for these adjusted WWV characteristics (Fig. 4.1b) using our regression model in order to understand the whole WWV precursor characteristic (Fig. 4.1c).

4.4.1 The influence of wind stress curl STD and frequency changes on the adjusted response

Consistent with the results of Chapter 3, we find that the wind stress curl STD has declined from the pre- to the post-2000 period in every box around the tropical Pacific (Fig. 4.4a, black dots, Fig. 4.4b). The ratios of post-2000 to pre-2000 STD of the different boxes range from 0.74-0.97 and the strongest wind stress curl STD declines can be found in the Southern Hemisphere (SH, box S3-S5, Fig. 4.4a and b). If the correlation of all these wind stress curl time series approached 1, the pre- to post-2000 STD decline of the sum of all these curl time series would be the sum of all curl time series' post-2000 STDs divided by the sum of all curl time series' pre-2000 STDs, which is 0.88 (Fig. 4.4b, curl time series of off-equatorial boxes are considered by 28%, see Equation 4.10). Thus, the decline in STD of the curls explains around 24.5% of the total decline of the regressed adjusted response (ratio=0.51, Fig. 4.1b).

After integrating each wind stress curl time series according to the regression model (Equation 4.10), the ratio ranges from 0.52-0.97 (orange dots, Fig. 4.4b). Considering again a correlation that approaches 1, the sums of these integrated curl time series' post- and pre-2000 STDs has a ratio of 0.75 (Fig. 4.4). Thus, the integration of the wind stress curl time series explains a further 26.5% of the total regressed adjusted WWV STD decline (Fig. 1b). This decline in ratio from 0.88 to 0.75 after integrating over a time period of around 8 months (Fig. 4.3c, Equation 4.10) can be explained by the strong average power spectral density peak during the post-2000 period found for the wind stress curl time series at a period of 7 month (Fig. 4.4c).

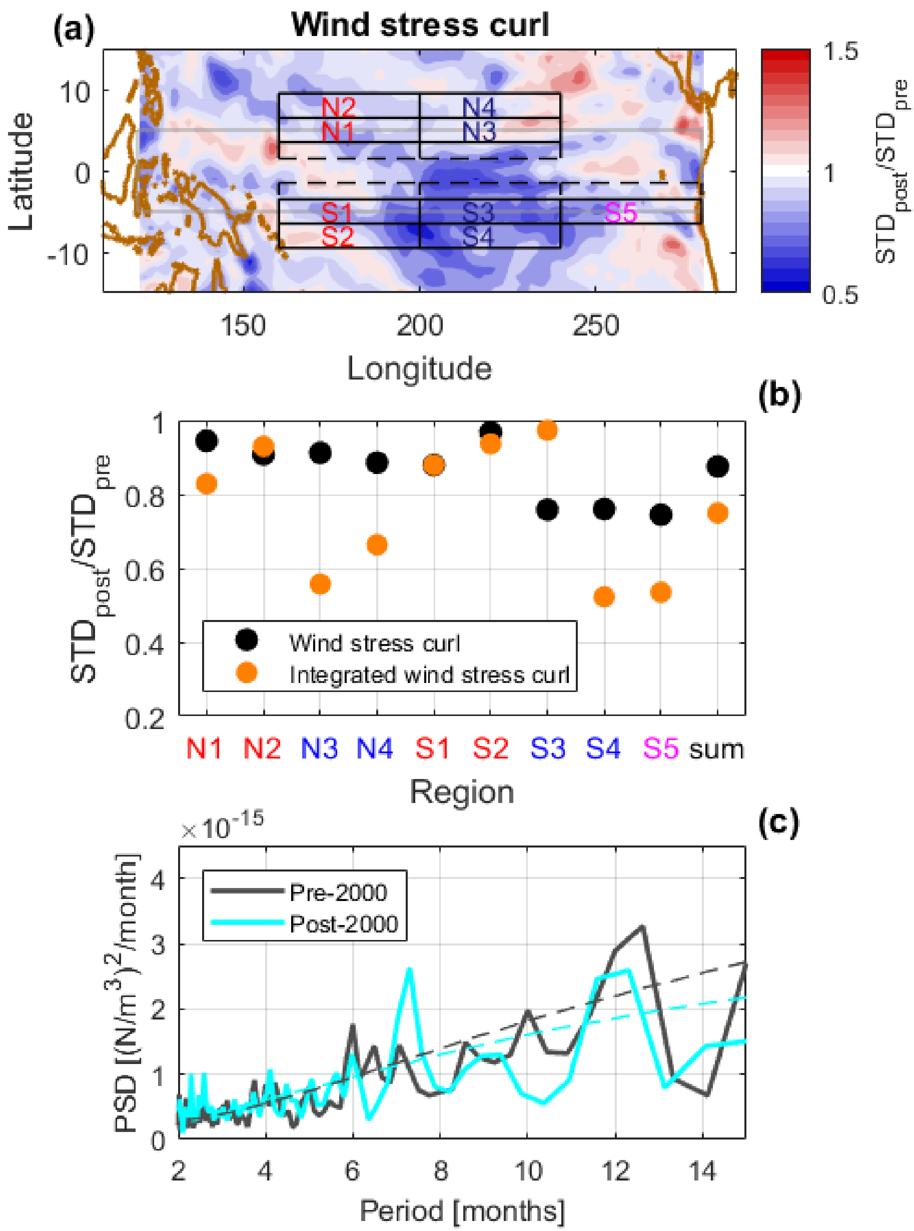

Figure 4.4: (a) Spatial pattern of the ratio of post- to pre-2000 wind stress curl standard deviation (STD). **(b)** The ratio of post- to pre-2000 wind stress curl STD of the different boxes in **(a)** before (black dots) and after integration (orange dots) according to the regression model (Equation 4.10, Fig. 4.3c). The "sum" on the x-axis gives the ratio of the sum of post-2000 STDs of all wind stress curl time series divided by the sum of pre-2000 STDs of all wind stress curl time series (curl time series of off-equatorial boxes are considered by 28%, see Equation 4.10). **(c)** Average of the power spectral densities $[(\frac{N}{m^3})^2 \cdot months^{-1}]$ of the wind stress curl time series of the boxes shown in **(a)** during the pre- (gray line) and post-2000 period (turquoise line). Dashed gray (turquoise) line marks the red noise 95% confidence limit of the gray (turquoise) spectrum.

In summary more than half (51%) of the post-2000 STD decline of the adjusted response is explained by: (i) the decline of the STD of the wind stress curl in each box (explaining 24.5% of the decline, Fig. 4.4a and b and Fig. 4.5); and (ii) by the higher frequency of the post-2000 average box wind stress curl time series (explaining 26.5% of the decline, Fig. 4.4c and Fig. 4.5). As these declines were obtained assuming a correlation of all wind stress curl time series that approaches 1, the remaining 49% of the post-2000 adjusted WWV decline results from the interplay of the forced Rossby waves of the different boxes (Fig. 4.3a) which need to have the tendency to positively interfere (cancel each other) during the pre- (post-) 2000 period as examined in the next section.

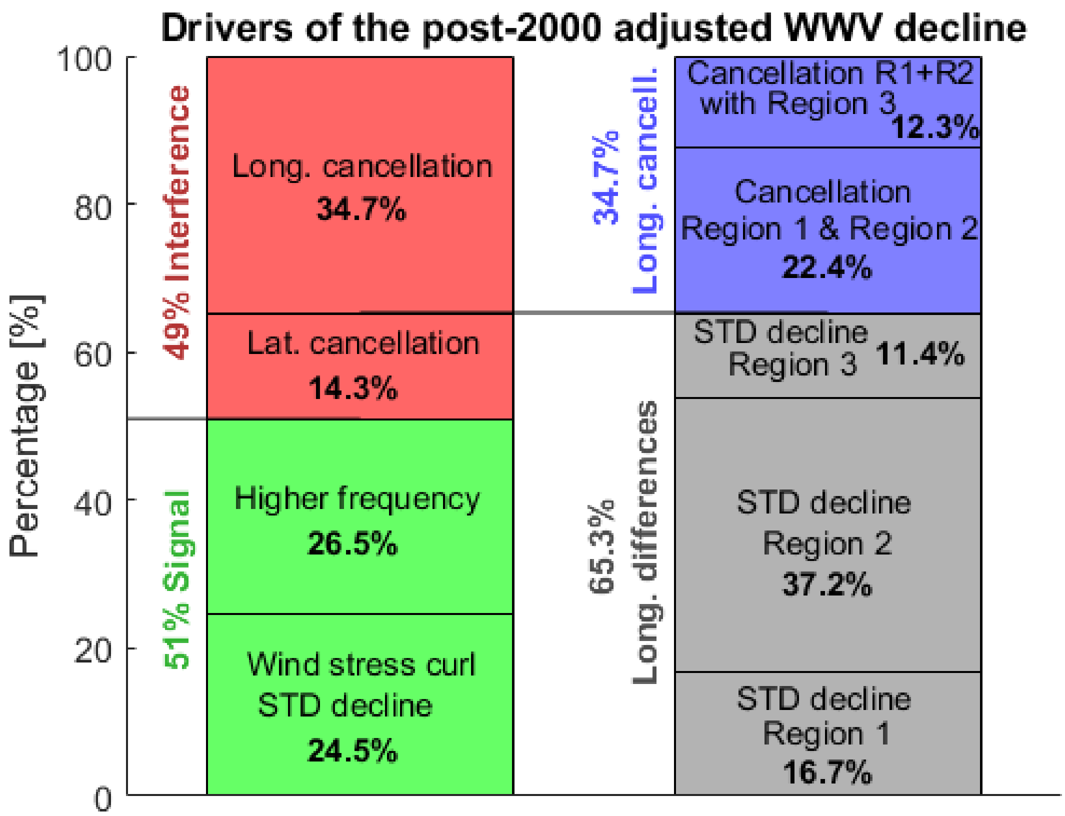

Figure 4.5: Summary of the drivers explaining the post-2000 regressed adjusted WWV STD decline of 49% (see Fig. 4.1b). On the left-hand side the drivers are divided into the post-2000 changes in: (i) the signal's characteristics (STD decline and frequency increase, green color, Section 4.4.1); and (ii) latitudinal and longitudinal signals cancellations (red color, Section 4.4.2). On the right-hand side, the signal's characteristic along with the latitudinal cancellation are summarized to divide the drivers into post-2000 changes in: (i) STD of each longitudinal Region (gray color); and (ii) signals interferences among the longitudinal regions.

4.4.2 Regional interferences

This subsection aims to understand the contribution of the WWV decline explained by: (i) latitudinal and longitudinal interferences; and (ii) different longitudinal regions. Thus, the regressed signals of the 4 boxes in Region 1 (160-200°E) and Region 2 (200-240°E) are summed, and the regressed signal of box S5 is contributed to Region 3 (240-280°E) (Fig. 4.6a-c). It is clear that the summed and regressed signal in Region 1 has a 2/8.3 times stronger STD when compared to the STDs of the summed and regressed signals of Region 2/Region 3 (Fig. 4.6a-c).

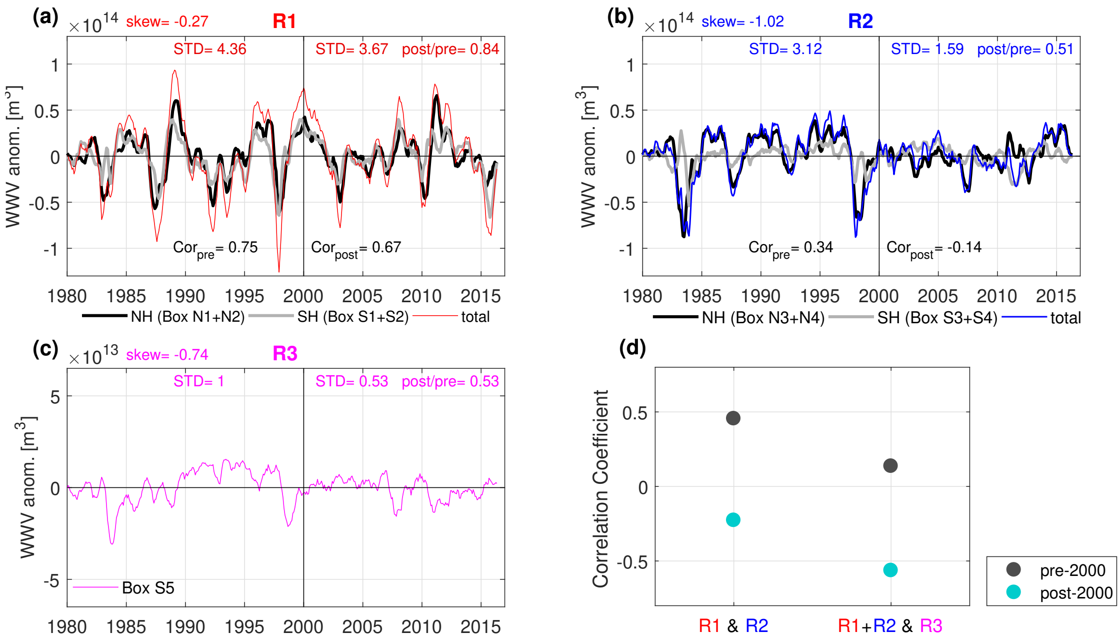

Figure 4.6: **(a)** Sum of the regression model's warm water volume (WWV) anomaly signal $[m^3]$ of Northern Hemisphere (NH) boxes N1 and N2 (black line), and Southern Hemisphere (SH) boxes S1 and S2 (gray line) in Region 1 (R1). The thin red line gives the sum of the regression model's WWV anomaly signal of all boxes in R1 (sum of the black and gray line). **(b)** same as **(a)** but for the box N3 and N4 (black line), and S3 and S4 (gray line), where the thin blue line gives the sum the regression model's WWV anomaly signal of all boxes in Region 2 (R2, sum of black and gray line). **(c)** The regression model's WWV anomaly signal of box S5 (Region 3). Note, that the y-axis scale here is a half of that in **(a)** and **(b)**. Skew stands for skewness and STD is the standard deviation in $10^{13}m^3$. **(d)** Correlation between the regression model's WWV anomaly signal of the Region 1 and Region 2 and of the sum of Region 1 and Region 2 to Region 3 for pre- (gray dots) and post-2000 period (turquoise dots).

a) Latitudinal cancellations

When assuming again a correlation that approaches 1 of the signals of the three different region and thus, summing the pre-2000 STDs of all three regions and the post-2000 STDs of all three regions, the resulting post- to pre-2000 STD ratio is 0.68. Thus, a further 14.3% of the adjusted WWV decline (from 0.75 to 0.68) is explained by summing the signals of the different latitudinal boxes in a given longitudinal region (Fig. 4.5). This latitudinal cancellation is clearly found in Region 1: the average signal of the Northern Hemisphere (NH) in Region 1 boxes (N1+N2) constructively interferes with the average signal of the SH boxes of Region 1 (S1+S2) during the pre-2000 period, which is supported by a correlation of 0.75 (Fig. 4.6a). However, the same correlation weakens during the post-2000 period (0.67, Fig. 4.6a). Similarly, the combined Region 2 signal displays a post-2000 reduction of interference between the signals of the NH and SH boxes' as indicated by a positive correlation of 0.34 during the pre-2000 period, and a correlation of -0.14 during the post-2000 period.

b) Longitudinal cancellations and differences

It follows that the final 34.7% of the post-2000 adjusted WWV STD decline (from 0.68 to 0.51) are explained by post-2000 cancellations of the regressed signals among the three longitudinal regions (Fig. 4.5). The sum of the regressed WWV signal of Region 1 and the regressed WWV signal of Region 2 has a post- to pre-2000 STD ratio of 0.57. Therefore, a further 22.4% of the adjusted WWV STD decline (from 0.68 to 0.57) is explained by the Region 1/Region 2 post-2000 signals cancellation (Fig. 4.5). This post-2000 cancellation is underpinned by a moderate positive interference (cor=0.46) of the signals of Region 1 and Region 2 during the pre-2000 period which changes to a weak cancellation (cor=-0.23) during the post-2000 period (Fig. 4.6d). Additionally, the signal of Region 3 is weakly positively correlated (cor=0.14) to the sum of the signals of Region 1 and Region 2 during the pre-2000 period, but this interference changes to a clear cancellation during the post-2000 period (cor=-0.56, Fig. 4.6d) which explains the remaining 12.3% of the adjusted

WWV STD decline (Fig. 4.5).

When summing all three regions' (Fig. 4.6a-c): (i) pre-2000 STDs, and (ii) post-2000 STDs the absolute decline is $2.69 \cdot 10^{13}\ m^3$. Note that this absolute STD decline explains the above shown post- to pre-2000 STD ratio of 0.68 which explains 65.3% of the total regressed adjusted WWV STD decline due to: (i) a wind stress curl decline; (ii) frequency changes; and (iii) latitudinal cancellations (Fig. 4.5). More than half (56.9%) of the 65.3% decline (in total 37.2% of the regressed adjusted WWV decline) is explained by the STD decline in Region 2 which shows a ratio of 0.51 and an absolute decline of $1.53 \cdot 10^{13}\ m^3$ (Fig. 4.6b, Fig. 4.5). The remaining 25.7%/17.4% of the 65.3% decline (in total 16.7%/11.4% of the regressed adjusted WWV decline) is explained by the STD decline of Region 1/Region 3 which has a post- to pre-2000 ratio of 0.84/0.53, and which shows an absolute decline of $0.69/0.47 \cdot 10^{13}\ m^3$ (Fig. 4.6a and c, Fig. 4.5).

In brief, although the STD of the regression model's signal is strongest in Region 1, the STD decline in this region only explains 16.7% of the total adjusted WWV decline (Fig. 4.5). In contrast, the STD decline of the regressed signal in Region 2 explains more than a third (37.2%) of the total adjusted WWV decline (Fig. 4.5). Consequently, the signal in Region 2 is the dominant driver in explaining the post-2000 adjusted WWV decline.

Similarly, the strong negative skewness of the regressed adjusted WWV (-0.81, Fig. 4.1b) is dominated by the strong negative skewness of the signal in Region 2 (-1.02 Fig. 4.6b). The skewness in Region 1/Region 3 (-0.27/-0.75) is clearly weaker.

4.4.3 Comparison to the Rossby wave projection model

We compare the main results of the regression model to the output of the RW projection model. The RW projection model is forced by monthly mean ERA-interim wind stress without considering a wave propagation to obtain a monthly mean estimate of the Rossby wave projections of the first 6 meridional modes. The first 6 meridional modes are sufficient to cover the latitudes of the boxes defined for the regression model (Fig. 4.2). We then sum the RW projections of the symmetric modes (m=1, 3 and 5) and the anti-symmetric modes (m=2, 4 and 6) for each longitudinal region. The time series of the symmetric and anti-symmetric RW projections is smoothed by an 8-month running average for each region (Fig. 4.7) to make comparisons to the regression model whose curls are also integrated by around 8 months (Equation 4.10, Fig. 4.3c). Note, that nearly only the symmetric modes add to WWV changes, as the signals of anti-symmetric modes in the NH and SH almost cancel each other out (Fig. 4.2).

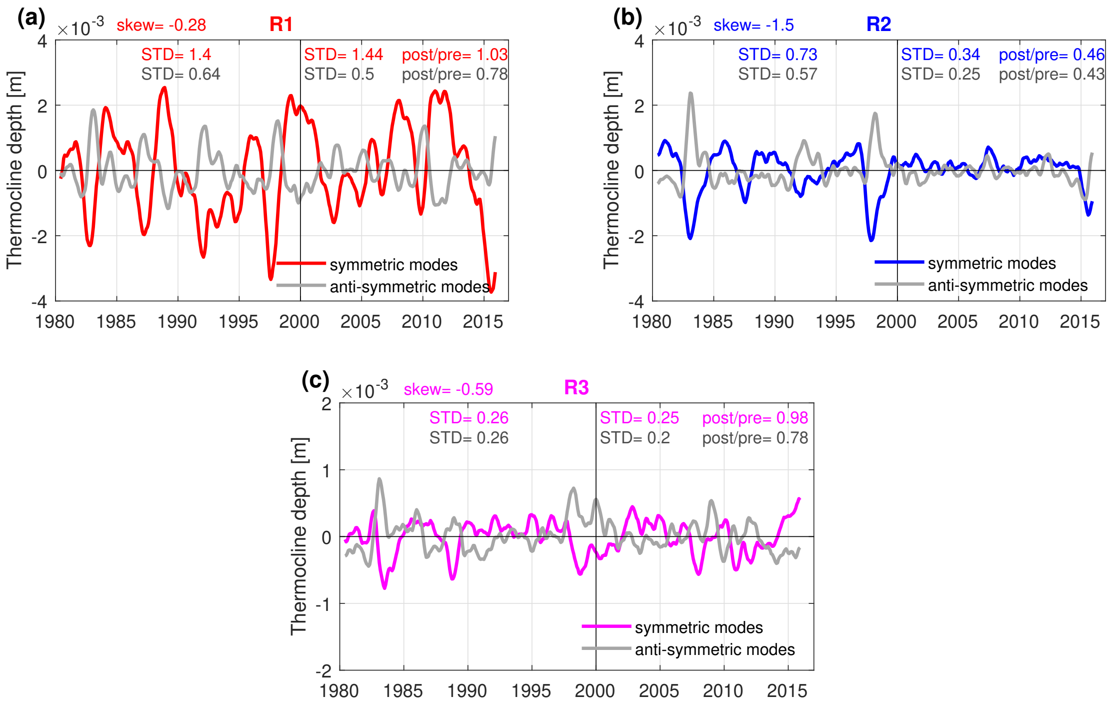

Figure 4.7: **(a)** Sum of the thermocline depths [m] of the first six symmetric (red line) and anti-symmetric (gray line) Rossby wave modes (see Fig. 4.2) averaged over Region 1 (R1). **(b)** same as in **(a)** but averaged over Region 2 (R2) and the blue lines gives the symmetric modes. **(c)** same as in **(a)** but averaged over Region 3 (R3) where the magenta line gives the symmetric modes. Note, that the y-axis scale here is a half of that in **(a)** and **(b)**. Skew stands for skewness and STD is the standard deviation with the unit 1000 m.

As with the regression model, the strongest (weakest) signal of the symmetric modes is found in Region 1 (Region 3) and the negative skewness of the symmetric mode signal is lowest (highest) in Region 1 (Region 2). Moreover, the strongest post-2000 STD decline of the symmetric modes can be found in Region 2, which is similar to that of the regression model (Fig. 4.7b and Fig. 4.6b). However, as the regression model shows a slight cancellation of signals from the NH and SH in Region 2, we would expect that the anti-symmetric mode signal would be more dominant in the pre-2000 period of Region 2, whereas this is not the case. Additionally, the decreased STD found in Region 3 of the regression model is not apparent in the symmetric RW projections of Region 3. This might be because the regression model only considers the SH in Region 3, while the projection model considers the whole range of latitudes from the first 6 projections (Fig. 4.2).

4.5 Is there any consistency between equatorial wind stress and its curl?

Chapter 3 demonstrated that the wind stress averaged over the WWV region is not a reliable proxy for the wind stress curl/Rossby wave signal because this wind stress does not show the pre- to post-2000 STD decline or the strong negative skewness of the adjusted contribution. To better understand the wind stress/wind stress curl relationship, this section aims to examine the consistency between the equatorial wind stress (between 5°N and 5°S) of the different longitudinal regions 1-3 and the curls of the different boxes for pre- and post-2000 periods.

On average the wind stress has the strongest STD in Region 1, and weakens eastward in Region 2 and 3 (Fig. 4.8a and c). This eastward weakening of wind stress is consistent with the strongest coupling between wind stress and ENSO SST being found in the western/central Pacific (e.g. Deser and Wallace, 1990).

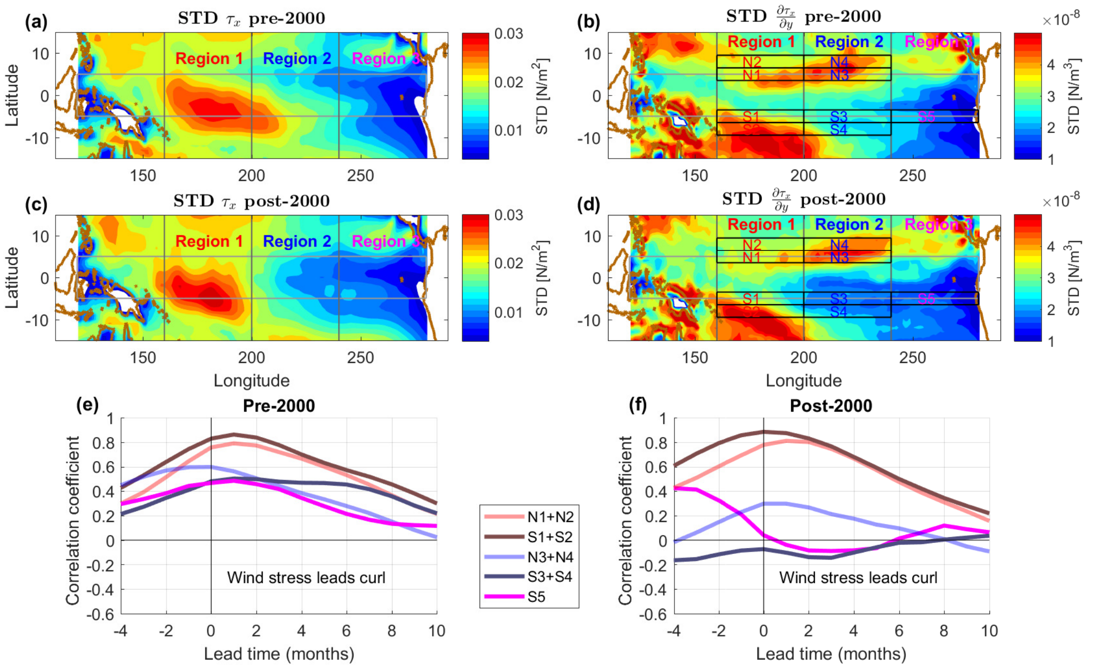

Figure 4.8: STD of **(a)** the zonal wind stress and **(b)** the curl of the zonal wind stress during the pre-2000 period. **(c)**/**(d)** same as **(a)**/**(b)** but for the post-2000 period. **(e)**/**(f)** Pre-2000/post-2000 lead lag correlations between the wind stress averaged over 5°N-5°S and over (i) Region 1 and the curl of the boxes N1+N2 (light red line) and S1+S2 (dark red line); (ii) Region 2 and the curl of the boxes N3+N4 (light blue line) and S3+S4 (dark blue line); and (iii) Region 3 and the curl of the box S5.

When comparing the pattern of the wind stress and its curl in Region 1, both show consistencies (Fig. 4.8a-d). During the pre-2000 period the wind stress is not symmetrical around the equator but is shifted by around 2° to the south. Similarly, the wind stress curl pattern is also shifted to the southward (Fig. 4.8b). During the post-2000 period the strongest wind stress of Region 1 is even further shifted to the south and its pattern is meridionally broader in the NH. As a result, the post-2000 wind stress curl is weaker in the NH boxes (N1+N2) and in the SH boxes (S1+S2) compared to the pre-2000 wind stress curl, but is stronger in the western end of the off-equatorial SH box (S2, Fig. 4.7d). Despite these changes in wind stress patterns, the wind stress STD in Region 1 has not changed from the pre- to post-2000 period (ratio post- to pre-2000 wind stress=1.02). The wind stress curl STD of the boxes in Region 1, however, has slightly declined by 6-17% from the pre- to post-2000 period (Fig. 4.4b and Fig. 4.8b and c). Nevertheless, as the wind stress curl is strong in both NH and SH boxes (Fig. 4.8b and c), the wind stress averaged over Region 1 is a good proxy for the wind stress curl/ Rossby wave signal in Region 1 for both time periods. This consistency between wind stress and its curl in Region 1 can be seen by their peak correlations in the NH and SH boxes ranging from 0.79-0.88 (Fig. 4.8e and f).

While the wind stress curl in Region 1 is similarly strong in NH and SH boxes, there is a clear discrepancy between the strong wind stress curl STD in the NH boxes of Region 2 compared to the weak wind stress curl STD of the SH boxes (Fig. 4.8b and d). This difference is apparent during the pre-2000 period, but is enhanced during the post-2000 period when the wind stress curl STD of the SH boxes strongly declines (Fig. 4.4b and 4.8d). This decline of the wind stress curl in the SH boxes is accompanied by a strong weakening of wind stress in the south equatorial Region 2 from pre- to post-2000 period (Fig. 4.8a and c, ratio post- to pre-2000 wind stress= 0.75). While the equatorial wind stress in Region 2 is a weak proxy for the wind stress curl during the pre-2000 period for the NH/SH boxes (cor=0.6/0.5, Fig. 4.8e), it fails to provide a good proxy for the wind stress curl during the post-2000 period (correlations below 0.29, Fig. 4.8f). This can be explained by the larger difference between NH and SH wind stress curls (i.e. one wind stress averaged over the equatorial Region 2, which cannot explain both the strong/weak curl north/south of the equator). Furthermore, it is assumed that off-equatorial winds have a larger impact on the curls of Region 2 than Region 1 due to the weaker equatorial wind stress being stronger influenceable in the overlaid pattern of off-equatorial winds. This is also consistent with the low accordance between the wind stress in Region 3 and the curl of box S5 (Fig. 4.8e and f).

4.6 Summary and Conclusion

The aim of this study was to understand the characteristics (i.e. the pre- to post-2000 STD decline and the strong negative skewness) of the adjusted WWV (Fig.

4.1b) which is mainly consistent with WWV changes driven by Rossby waves (Neske and McGregor, 2018, Section 2). The adjusted WWV is of particular importance for understanding ENSO dynamics as: (i) it dominates the characteristic (skewness and STD decline) of the whole WWV precursor (Section 4.4, Fig. 4.1b-d); and (ii) longer term predictable lead times of ENSO SSTs (>6 months) are due to the adjusted WWV only (Neske and McGregor, 2018). Additionally, it is thought that the adjusted WWV needs to overcome a certain threshold as a necessary condition in order to trigger a new ENSO event (Chapter 3).

Traditional ENSO theory (Suarez and Schopf, 1988, Jin, 1997) assumes that the adjusted WWV is driven by strong equatorial wind stress during ENSO events initiating strong Rossby wave signals. Previous studies (Chapter 3, Clarke, 2008), however, emphasize the importance of considering the wind stress curl for understanding (adjusted) WWV changes. In particular, we have shown in Chapter 3 that the majority of the strongest equatorial wind stress does not coincide with a strong wind stress curl initiating strong Rossby waves. Therefore, and in order to improve understanding of the adjusted WWV characteristics, we successfully reconstruct the adjusted WWV (cor=0.94, Fig. 4.1b) with a wind stress curl regression model (Equation 4.10, Fig. 4.3c). This wind stress curl regression model approximates the Rossby wave signal by the wind stress curl in different boxes (equatorial boxes between 3.5-6.5°latitude and off equatorial boxes between 6.5-9.5°latitude) around the equatorial Pacific (Fig. 4.3).

In line with Chapter 3, we find that the wind stress curl STD reduces from the pre- to post-2000 period for all the boxes around the tropical Pacific (Fig. 4.4a and b). Using the regression model (Equation 4.10, Fig. 4.3), we identified that this STD curl decline is responsible for around one quarter of the post-2000 adjusted WWV decline (Fig. 4.5). Another quarter of the post-2000 adjusted WWV decline is explained by the strong post-2000 peak in power spectral density at a period of 7 months (Fig. 4.4c), as the regression model integrates over 8 months (Fig. 4.3c, Equation 10). The remaining half of the post-2000 adjusted WWV decline is due to a post-2000 latitudinal and longitudinal cancellation of the regressed wind stress curl signals (14.3% and 34.7% respectively, Fig. 4.5 and 4.6).

To understand longitudinal forcing differences that play a role for the adjusted WWV decline and its strong negative skewness, we further sum the signals of the regression model of the boxes in three different longitudinal regions: (i) Region 1 between 160 and 200°E; (ii) Region 2 between 200 and 240°E; and (iii) Region 3 between 240 and 280°E. Thus, the summed regressed signal of each longitudinal region takes into account: (i) the STD curl changes; (ii) frequency changes; and (iii) latitudinal interferences of the boxes in this region. While the strongest WWV STD stems from Region 1 (averaging the regressed WWV signals of the boxes in Region 1, Fig. 4.3a), its pre- to post-2000 STD decline only explains 16.7% of the total adjusted WWV decline (Fig. 4.5 and 4.6). Additionally, the negative skewness of the regressed WWV signal of Region 1 (-0.27, Fig. 4.6a) is around 3 times smaller than that of the total regressed adjusted signal (total skewness=-0.81, Fig. 4.1b and Fig. 4.6a). Consequently, although the STD of the WWV signal in Region 2 (averaging the regressed WWV signals of the boxes in Region 2) is only around a half of the STD of the WWV signal in Region 1 (Fig. 4.6a and b), the WWV signal in Region 2 dominates the characteristics of the adjusted WWV. The STD decline of the regressed WWV signal in Region 2 explains 37.2% of the total adjusted WWV decline and the strong negative skewness (-1.02) of the signal in Region 2 is almost four times stronger than that of Region 1 (-0.27, Fig. 4.6a and b). The dominant weakening of the Rossby wave signal in Region 2 and its strong negative skewness are also consistent with the results of a Rossby wave projection model (Fig. 4.7).

These results indicate that the dominant longitudinal region to observe in order to better understand the total WWV characteristics lies between 200 and 240°E (i.e. Region 2). As such, despite Region 1 (160-200°E) having the strongest coupling between wind stress and ENSO SST (Deser and Wallace, 1990), this region plays a secondary role. While the wind stress is shown to be a good proxy for the wind stress curl/Rossby wave signal of Region 1, the wind stress fails to be a proxy for the wind stress curl/ Rossby waves signal for Region 2 (Fig. 4.8). This explains why the wind stress integrated over the WWV region is not a good proxy for understanding the details of the adjusted WWV (Chapter 3). As indicated in Chapter 3, the strongest wind stress curls extend towards Region 2 during Eastern Pacific (EP) ENSO events, but these are confined in Region 1 during Central Pacific (CP) ENSO events. Thus, the post-2000 dominance of CP ENSO events (e.g. McPhaden et al., 2011) is consistent with the post-2000 STD decline of wind stress curl in Region 2.

Therefore, our study suggests that the post-2000 decline in the predictability of ENSO has some physical origin, namely the post-2000 transition to CP type ENSO events, as these do not produce strong adjusted WWV changes. This finding is in agreement with Zhang et al. (2019) who relate the long/short WWV/ENSO SST lead times during different periods to the dominance of EP/CP ENSO events over CP/EP ENSO events. A number of other studies (e.g. Kumar et al., 2015, Zhao et al., 2016) emphasize that the post-2000 ENSO prediction skill decline is due to the decline of the ENSO SST's STD causing a lower signal-to-noise ratio. We suggest, however, that the post-2000 STD decline of ENSO SST and its lower predictive skill is at least partially driven by the post-2000 decline in adjusted WWV responsible for the whole post-2000 WWV decline. For instance, the predictive skill for La Niña events is stronger/weaker when initialized during stronger/weaker discharged conditions because the predicted signal is stronger/weaker and less/stronger influenced by noise (DiNezio et al., 2017).

Appendix Chapter 4

Text A4.1

Following the linear shallow water equations under the long wave approximations we obtain the following Rossby wave velocity:

$$c_{RW}(y) = \beta(y)(\frac{c_{KW}^2}{f(y)^2}); \tag{4.11}$$

where $\beta(y) = \frac{\partial f(y)}{\partial y}$, f is the Coriolis parameter, y the meridional distance and c_{KW} is the first meridional mode Kelvin wave velocity (2.8 m/s).

We then obtain the average Rossby wave travel time of a box (t_{box}) to the western boundaries defined at 120°E/150°E for the boxes in the Northern/Southern Hemisphere (green lines, Fig. 4.3a) with the following:

$$t_{box} = \frac{distance_{box}}{c_{RWbox}} \tag{4.12}$$

where $distance_{box}$ and c_{RWbox} are the box average zonal distance and the box average Rossby wave velocity to the western boundaries respectively.

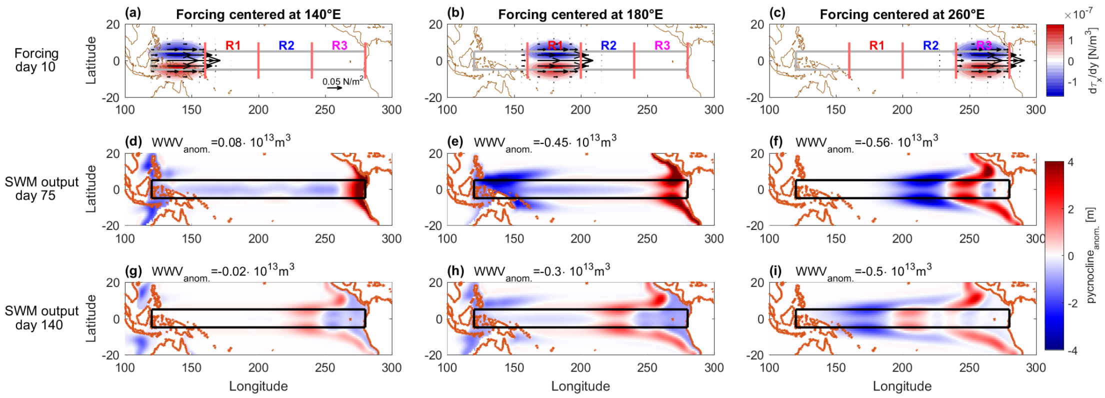

Figure A4.1: **(a)-(c)** wind stress forcing [N/m^2] (arrows) and its curl [N/m^3] (shading) created with the wind (U) which is Gaussian in time (t), longitude (x) and latitude (y): $U(t,x,y) = U_0 exp\left[-(\frac{x-X_0+t}{L_x})^2\right] exp\left[-(\frac{y-Y_0+t}{L_y})^2\right] exp\left[-(\frac{t-T_0}{T_e})^2\right]$, where U_0 is set to 21 m/s, X_0 and Y_0 mark the spatial center (0° latitude, and **(a)**: 140°E; **(b)**: 180°E; **(c)**: 260°E), L_x (=1.85·10^6 m) is the longitudinal, and L_y (=0.7·10^6 m) is the latitudinal e-folding scale, T_0(=10 days) gives the day of maximum wind and T_e (=3 days) is the e-folding time scale. U is converted to wind stress using the linear stress law. **(d)-(f)** gives the pycnocline depth at day 75 when a shallow water model (SWM) is forced by the wind stress in **(a)-(c)**. **(g)-(i)** same as **(d)-(f)** but at day 140.

Chapter 5

Concluding remarks

5.1 Summary and Conclusion

The aim of this thesis is to improve our understanding of ENSO dynamics and predictability. This thesis was largely motivated by the observed decline in WWV/ENSO SST lead time from around 2-3 seasons during the pre-2000 period (1980-1999) to only 1 season during the post-2000 period (McPhaden, 2012, Horii et al., 2012, Bunge and Clarke, 2014). The short WWV/ENSO lead time during the post-2000 period challenges the traditional view of ENSO being a self-sustained oscillation (Suarez and Schopf, 1988, Battisti and Hirst, 1989, Jin, 1997), as it demonstrates that the preconditioning of a new ENSO event is not solely due to the ocean WWV memory of a preceding event (McGregor et al., 2016). Moreover, this post-2000 decline of WWV/ESNO SST lead time coincides with a post-2000 decline in ENSO prediction skill of forecast models (Wang et al., 2010, Barnston et al., 2012, Kumar et al., 2015). Consequently, it is thought that improving our understanding of the post-2000 lead time shortening will lead to a better understanding of limits and possibilities of ENSO prediction. Thus, this thesis aims to deepen our knowledge of the dynamics driving the changes of the WWV precursor of ENSO events between 1980-2016. This section will provide a summary and conclusion of thesis Chapters 2-4 as well as it discusses some limitations. Finally, the thesis ends with the next section providing some future perspectives.

5.1.1 Chapter 2

In Chapter 2 (Neske and McGregor, 2018) we use SWM simulations to decompose the WWV changes between 1980-2016 into their instantaneous and adjusted wind responses. Hereby, the adjusted response is defined as the averaged third month WWV outcome of the wind-forced simulation that is left to evolve unforced for three months. Any wind-excited Kelvin wave has reached the eastern boundary during the three months of free evolution, and thus, the adjusted response is shown to be largely consistent with Rossby waves reflecting into the WWV region. Consequently, the adjusted contribution consists mainly of the ocean's memory which is referred to by the recharge discharge (Jin, 1997) and delayed oscillator theories (Suarez and Schopf, 1988) in order to explain ENSO as a self-sustained oscillation. The instantaneous response is the WWV outcome of the SWM forced by winds over the preceding three months only. Therefore, it is largely consistent with WWV changes dominated by wind forced Kelvin waves, and it shows a correlation of 0.9 to WWV changes driven by meridional Ekman transports. The sum of the adjusted and instantaneous WWV contributions gives the SWM's control WWV, which is shown to be highly consistent to observed WWV (cor=0.84). Some uncertainties of this study might arise due to: (i) the SWM only representing the first baroclinic mode (Izumo et al. (2019) estimate that the second and third baroclinic modes contribute by around 30% to the total WWV changes); and (ii) the signal of some Rossby waves that have not been reflected after three months (i.e. those excited in the eastern Pacific) and the reflection of wind forced Kelvin waves at the eastern boundary might influence the adjusted response.

We find that the adjusted contribution dominates the WWV changes during the pre-2000 period as it can be seen by a 30% larger standard deviation (STD) of the adjusted signal compared to the STD of the instantaneous signal. However, the instantaneous contribution's STD increases by 15% from pre- to post-2000 period while the adjusted contribution's STD declines by 44% in the post-2000 period. Consequently, the instantaneous contribution dominates the WWV changes during the post-2000 period (its STD is by 30% larger than that of the adjusted contribution). The strong post-2000 decline of the adjusted contribution and the post-2000 dominance of the instantaneous contribution is shown to explain the post-2000 shortening in WWV/ENSO SST lead time: During the pre-2000 period both contributions show strong correlations to ENSO SST at lead times of around: (i) 1 season for the instantaneous contribution; and (ii) 3-4 seasons for the adjusted contribution. Thus, both contributions are nearly equally important in explaining the pre-2000 WWV/ENSO SST lead time of around 6 months. However, during the post-2000 period the smaller adjusted contribution plays little role as a precursor for

ENSO SST (lead correlations to ENSO SST are insignificant) and as such, the whole WWV/ENSO SST lead correlation resembles that of the short (around 1 season) instantaneous contribution/ENSO SST alone.

Further to this, a clear ENSO asymmetry is found: the control WWV discharged phases are dominated by the adjusted contribution while the control WWV recharged phases are dominated by the instantaneous contribution during the whole study period. The latter is most remarkably found during the post-2000 period where the correlation between the recharged control WWV and: (i) the adjusted response is -0.05; and (ii) the instantaneous response is 0.79.

The existence of this large instantaneous contribution especially during the post-2000 period clearly challenges the dominance of the recharge-discharge (Jin, 1997) and delayed oscillator (Suarez and Schopf, 1988, Battisti and Hirst, 1989) theories. While the ENSO asymmetry reported in this study reveals that these theories are largely at work for the WWV discharge precursor of La Niña events, the results suggest that the build-up of WWV prior to El Niño events in the post-2000 period is largely associated with westerly wind bursts. These westerly wind bursts have been shown to trigger the El Niño events themselves (e.g. Harrison and Vecchi, 1997), which is consistent with the shorter WWV/ENSO lead time of only 3 months. It is important to note, however, that while our results raise questions over the dominance of the oscillatory view of ENSO in this post-2000 period and provides support for viewing ENSO as event like disturbance (e.g. Thompson and Battisti, 2001, Kessler, 2002, Zavala-Garay et al., 2004, Fedorov et al., 2015), it is clear that both the self-sustained cyclic and event-like views of ENSO are at work and what actually happens is that one dominates over the other during different periods.

5.1.2 Chapter 3

The study of Chapter 3 seeks to understand how the adjusted WWV contribution's STD could have declined by 44% from pre- to post-2000 period, while the instantaneous WWV contribution's STD has increased by 15% at the same time (Neske and McGregor, 2018, Chapter 2). Given that both WWV contributions are forced by the same winds, we would expect from the traditional ENSO view (e.g. Suarez and Schopf, 1988, Jin, 1997) that a decrease in the STD of the adjusted WWV is connected to a decrease in STD of the equatorial winds. As such, the instantaneous contribution's STD should have declined in line with the adjusted contribution. Thus, to untangle this conflicting evidence we examine the adjusted responses following the wind forcing of the 23 strongest instantaneous responses calculated over the region east of 200°E ($\mathrm{WWV}_{inst.east}$, it shows a high correlation (0.92) to equatorial wind stress) between 1980-2016. These adjusted responses are categorized as: (i) transitioning (i.e. strong equatorial westerly/easterly wind stress is followed by an adjusted discharge/recharge); (ii) neutral (i.e. strong equatorial wind stress is followed by a negligible adjusted response); and (iii) persistent adjusted responses (i.e. strong equatorial westerly/easterly wind stress is followed by an adjusted discharge/recharge).

We find that only 35% of strong anomalous equatorial winds are followed by the transitioning adjusted responses expected from theory, while of the remaining winds, 56% are followed by neutral adjusted responses and 9% are followed by persistent adjusted responses. Moreover, 75% of the winds with transitioning adjusted responses are found during the pre-2000 period in agreement with the post-2000 decline of the: (i) adjusted response (Neske and McGregor, 2018, Chapter 2), and (ii) ENSO prediction skill (Wang et al., 2010, Barnston et al., 2012, Kumar et al., 2015). Idealized SWM experiments reveal that the neutral adjusted WWV response is largely excited by anomalous wind stress forcing with weak off-equatorial curls (consistent with a meridionally broader wind stress pattern and a higher ratio of off-equatorial to equatorial wind events), which excites weaker Rossby waves when compared to events that display a transitioning adjusted response. The SWM experiments demonstrate high consistencies with the outcome of the global ocean sea ice model GFDL-MOM025 which incorporates the full ocean's density structure (the SWM only contains the first baroclinic mode). Additionally, it is shown that the average transitioning/neutral adjusted response is forced during Eastern/Central Pacific (EP/CP) ENSO SSTs.

Moreover, a prominent ENSO phase asymmetry where strong anomalous equatorial westerly winds (i.e., during El Niño events) are roughly twice as likely to generate a strong discharge of WWV than strong anomalous equatorial easterly winds (i.e., during La Niña events) are to generate a recharge of WWV. This is consistent with the finding that the delayed thermocline feedback that is from the traditional ENSO view thought to transition the ENSO phase (Suarez and Schopf, 1988, Battisti and Hirst, 1989, Jin, 1997) is stronger/weaker during El Niño/La Niña events (Guan et al., 2019) due to a non-linearity between event magnitude and the thermocline response during La Niña events (DiNezio and Deser, 2014). Additionally, the ENSO SST precursor skill is: (i) poor for the transitioning adjusted recharges following strong equatorial easterlies, and (ii) good for the transitioning adjusted discharges following the El Niño events. The good precursor skill of the transitioning adjusted discharges can be attributed to the strong adjusted and instantaneous discharges 8 months after the strongest equatorial westerlies which positively interfere to built a strong control WWV discharge. However, 8 months after the strongest transitioning equatorial easterlies, the adjusted recharge is counterbalanced by an instantaneous discharge leading to a negligible control WWV and the system remains in La Niña-like conditions. This ENSO phase asymmetry is consistent with El Niño events lasting a shorter period and having a stronger tendency to be followed by La Niña events than vice versa (Kessler, 2002, Larkin and Harrison, 2002, Okumura and Deser, 2010, Guan et al., 2019) and may be used to explain why long lead time forecasts of La Niña events may be possible (Luo et al., 2008, DiNezio et al., 2017).

While this study is valuable as it clearly highlights the importance of considering the wind stress curl rather than the equatorial wind stress for ENSO dynamics, some limitations of this study arise due to only considering the strongest wind stresses. Weak wind stresses with strong off-equatorial curls might lead to strong adjusted responses as well, influencing the pre- to post-2000 adjusted WWV decline. Additionally, while this study identifies the decline in the strength of the curls as important driver of the post-2000 adjusted WWV decline, it is not clear how other drivers (for instance, changes in the frequency of the curls signals or Rossby wave interferences/cancellations) might influence this decline as well.

5.1.3 Chapter 4

The aim of Chapter 4 is to systematically understand the different drivers that have contributed to the post-2000 adjusted WWV decline. The finding of Chapter 3 that the wind stress curl, rather than the equatorial wind stress, is crucial for understanding the adjusted WWV response is re-examined in this Chapter. This more complete examination is done by developing a wind stress curl regression model for the adjusted WWV response. This regression model approximates the Rossby wave signal of equatorial (3.5-6.5°lat) and off-equatorial (6.5-9.5°lat) boxes in three different longitudinal Regions around the tropical Pacific (Region 1 between 160 and 200°E; Region 2 between 200 and 240°E; and Region 3 between 240 and 280°E) using the wind stress curl. We consider: (i) the different Rossby wave travel times of the different boxes to the western boundary, and (ii) the stronger western boundary reflection efficiency of equatorial compared to off-equatorial Rossby waves. The resulting model produces an adjusted WWV response that is highly consistent with the adjusted WWV response of the SWM of Chapter 2 and 3 (cor=0.94).

Consistent with Chapter 3 the wind stress curl STD reduces from pre- to post-2000 period in all boxes around the tropical Pacific. The results of the regression model further show that this STD decline in wind stress curl alone is responsible for around 25% of the post-2000 adjusted WWV decline. Around another 25% of the post-2000 adjusted WWV decline is explained by a frequency increase of the wind stress curl signals from pre- to post-2000 period. The remaining 50% explaining the post-2000 adjusted WWV decline is found by latitudinal and longitudinal cancellations of the Rossby wave signals.

When considering the adjusted WWV STD decline from the contributions of the three different Regions (i.e. the curl STD, frequency and latitudinal cancellation is taken into account for the signal of each longitudinal region), it is shown that Region 2 has the dominant influence (explaining 37.2% of the total adjusted WWV decline). Although the STD of the signal in Region 1 is around twice as strong compared to the STD of the signal in Region 2, the signal in Region 1 contributes only to 16.7% of the total adjusted STD decline. The weak signal in Region 3 explains 11.4% of the total STD decline and the remaining 34.7% of the total adjusted WWV decline are explained by the cancellations of the signals among these three different longitudinal regions.

As shown in Chapter 3, the strongest wind stress curls extend towards Region 2 during EP ENSO events, but these are confined in Region 1 during CP ENSO events. Thus, the post-2000 dominance of CP ENSO events (e.g. McPhaden et al., 2011) is consistent with the large parts of the post-2000 STD decline of the adjusted WWV due to the post-2000 decline of wind stress curl in Region 2 during these CP ENSO events.

This study therefore suggests that the post-2000 decline in the predictability of ENSO has some physical origin, which is the post-2000 transition to CP type ENSO events as they only produce a weak adjusted WWV. This is in agreement with the study of Zhang et al. (2019) who relate the long/short WWV/ENSO SST lead times during different periods to the dominance of EP/CP ENSO events over CP/EP ENSO events. Other studies (e.g. Kumar et al., 2015, Zhao et al., 2016) connect the post-2000 decline in ENSO prediction skill to the post-2000 decline in ENSO SST variability producing a lower signal-to-noise ratio. We suggest, however, that this post-2000 lower variability of ENSO SST and thus the lower post-2000 ENSO predictive skill is at least partially driven by the post-2000 decline in adjusted WWV. Consistently, DiNezio et al. (2017) show that the predictive skill for La Niña events is stronger/weaker when initialized during stronger/weaker discharged conditions because the predicted signal is stronger/weaker and less/stronger influenced by the noise.

5.2 Future perspective

The three studies in this thesis have improved understanding of the WWV precursor of ENSO events. Particularly, we found that: (i) the instantaneous WWV contribution is responsible for the short WWV/ENSO SST lead time (around 1 season); and (ii) the adjusted contribution incorporates the long WWV/ENSO SST lead times (around 3-4 seasons). Additionally, the decline in the adjusted contribution STD is shown to cause the whole WWV/ENSO SST lead time to resemble the short lead time of the instantaneous contribution to ENSO SST; and the drivers for this adjusted WWV STD decline were identified. Future work aims to use this information about the WWV precursor acquired in this thesis to enhance the predictability of and precursor lead times to ENSO events. The above findings suggest that there are two potential future paths for enhancing ENSO predictability. The first path is to understand the predictability of the instantaneous signal itself. This means, if it is possible to predict the instantaneous contribution a couple of months in advance, this would extend its short lead time to ENSO SST, which is especially important during periods of a weak adjusted contribution (as shown for the post-2000 period). The second path is to understand the predictability of the adjusted signal itself, which means, if the adjusted contribution is predictable a couple of months in advance, this has the potential to make predictions of ENSO SST possible over a year in advance. However, as this thesis has shown, this is only useful during periods of strong adjusted WWV contributions (as shown for the pre-2000 period). As such, it also needs to be examined whether the results presented in this thesis can be used to predict which of the two WWV contributions is dominating in advance. This knowledge would reveal how the WWV/ENSO SST lead time can be improved

5.2.1 Understanding the predictability of the instantaneous WWV contribution

The instantaneous contribution is highly consistent with WWV changes due to meridional Ekman transports (Chapter 2). Experiments with the ACCESS-S1 forecast system (see Appendix Chapter 5, Text A5.1 for details) reveal that the precursor skill for the Ekman WWV from ERA-interim winds (same as calculated in Chapter 2, see Fig. A2.2) strongly decreases with lead month (Fig. 5.1). For instance, the correlation between the Ekman WWV from ERA-interim winds and the hindcasted Ekman WWV is below 0.6 for lead times >3 months (Fig. 5.1).

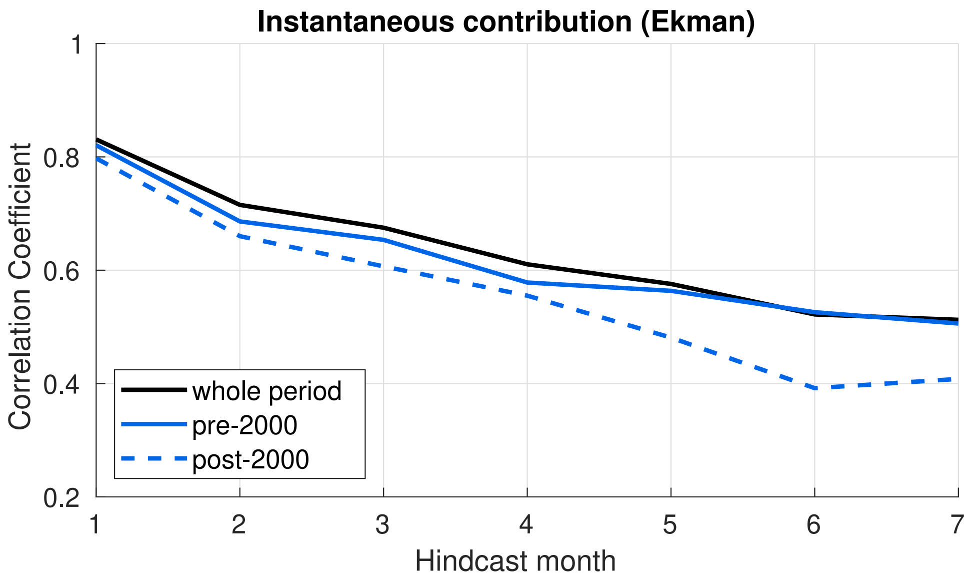

Figure 5.1: Correlation coefficient between WWV changes from Ekman calculated by ERA-interim winds (see Chapter 2, Fig. A2.2) and by the 1-7 month hindcasts of the ACCESS-S1 forecast system (see Appendix Chapter 5, Text A5.1) during the 1990-2013 (black line), the pre-2000 (blue line), and the post-2000 period (dashed blue line).

The instantaneous contribution is shown to be strongly influenced by equatorial easterly/westerly wind events (EWEs/WWEs, Chapter 3). Therefore, to improve the understanding of the predictability of the instantaneous (or Ekman) contribution as shown in Fig. 5.1, future work aims to improve the understanding of the potential of and limits to the predictability of such wind events. Hereby, the predictability of equatorial wind events in forecasts systems can be examined in more detail.

Additionally, we can improve our understanding of the physical drivers/precursors of wind events. While WWEs are often seen as "noise-like" forcing with individual WWEs being not predictable beyond weather prediction time scales (Barnston et al., 2012), some aspects of them are deterministic. For instance, characteristics of WWEs such as location and duration can be largely related to SSTs (e.g. Vecchi and Harrison, 2000, Yu et al., 2003, Vecchi, 2006, Gebbie and Tziperman, 2009), and it is shown that WWEs induce subsequent WWEs (Lengaigne et al., 2003). The question remaining is whether these deterministic aspects of equatorial wind events can be used to prolong the lead time of 1 season between the instantaneous contribution and ENSO SST presented here.

5.2.2 Understanding the predictability of the adjusted WWV contribution

The main focus of this thesis is on understanding the adjusted WWV contribution as this is the part of the WWV that contains the longer lead times to ENSO SST. When hindcasting the adjusted contribution with the ACCESS-S1 forecast system (see Text A5.1 for details) it is clear that the correlation between the hindcasted and observed signal during the post-2000 period is hardly better than seen for the forecast of the Ekman WWV (compare Fig. 5.1 and 5.2a). In contrast, the 1-7 month hindcasts during the pre-2000 period where the adjusted signal was strong, show correlations above 0.8 with the observed signal (Fig. 5.2a). While this stronger correlation is quite promising for prolonging the lead time to ENSO SSTs during periods of strong adjusted WWV contributions, the lead-lag correlations between the hindcasted signals and ENSO SST reveal that the lead time shortens for higher months hindcasts (Fig. 5.2b). This shortening of lead time to ENSO SSTs for higher months adjusted hindcasts suggests that the higher months hindcasts are only a decayed version of the actual signal. As such, we need to improve the understanding of the precursors of the adjusted contribution.

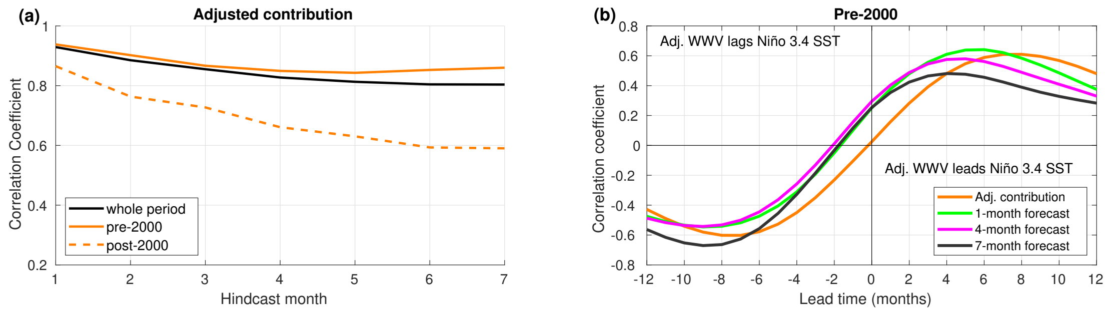

Figure 5.2: **(a)** Correlation coefficient between the adjusted contribution (see Chapter 2) and the 1-7 month hindcasts of adjusted contribution calculated by the ACCESS-S1 forecast system (see Appendix Chapter 5, Text A5.1) during the 1990-2013 (black line), the pre-2000 (orange line), and the post-2000 period (dashed orange line). **(b)** Lead-lag correlations between the Niño 3.4 SST (from the ERSST v5 data set) and the adjusted contribution (orange line), the 1- (green line), 4- (magenta line), and 7- (gray line) month hindcast of the adjusted contribution.

The thesis has shown that the adjusted contribution is determined by the following three drivers: (i) the wind stress curl strength in different regions around the tropical Pacific (which is largely related to the ratio of off-equatorial to equatorial wind events); (ii) the wind stress curl frequency; and (iii) by the interplay of Rossby waves excited in different regions. The question remaining is, whether changes in these three drivers rather happen by chance, or if they can be connected to other factors that can predict changes in these drivers on a longer time scale.

For instance, the pre- to post-2000 changes in the adjusted contribution happen alongside decadal changes in the Pacific basin such as the Pacific Decadal Oscillation (PDO, SST oscillation in the North Pacific, Mantua et al., 1997) and the Interdecadal Pacific Oscillation (IPO, a Pacific basin wide decadal SST mode, Power et al., 1999). Both the PDO and the IPO are in a positive phase during the 1980s and 1990s, and transition to a negative phase around the year 2000 (e.g. Newman et al., 2016, Henley et al., 2017). Additional research is needed to examine whether these changes can be linked to the changes of the three drivers determining the adjusted contribution.

Finally, it is clear that to understand how the changes of the three drivers arise, future work needs to broaden the view of ENSO from a climate variability determined by the (tropical) Pacific Ocean, to a climate variability being tightly interconnected to other ocean basins. For example, recent studies demonstrate that: (i) ENSO can excite other modes of climate variability in the Atlantic and Indian Oceans which can feed back onto the Pacific (Cai et al., 2019); and (ii) the adjustment of the tropical Atlantic and Indian Oceans to ENSO SSTs can influence the ENSO event evolution and wind anomalies in the Pacific Ocean (Wu et al., 2019). Therefore, experiments with global coupled ocean-atmosphere models are required to determine the influence and the interplay of remote ocean basins to changes in the drivers of the adjusted contribution.

Appendix Chapter 5

Text A5.1

The ACCESS-S1 forecast system

The ACCESS-S1 forecast system is developed from the UK Met Office's global coupled model seasonal forecast system GloSea5-GC2 (Global Seasonal forecast system version 5 using the Global Coupled model configuration 2, MacLachlan et al., 2015). The GC2 model of the GloSea5-GC2 consists of the UM Global Atmosphere 6.0, the Global Ocean 5.0, the Global Land 6.0 and the Global Sea Ice 6.0 model (Williams et al., 2015) which are coupled by the Ocean Atmosphere Sea Ice Soil coupler (OASIS3 Valcke, 2013). The atmospheric model consists of 85 vertical levels, a N216 horizontal resolution (0.8° in latitude and 0.5° in longitude) and the model is initialized from ERA-interim reanalyses (Dee et al., 2011). The ocean model has 75 vertical levels whose resolution ranges from 1 m near the surface to about 200 m close to the bottom which means that important ENSO processes are well resolved. Additionally, it has a horizontal resolution of 0.25°. The hindcasts of the ocean are initialized by the FOAM (Forecast Ocean Assimilation Model) analyses (Blockley et al., 2014).

Main differences between the ACCESS-S1 and the GloSea5-GC2 are the ensemble size, method of ensemble generation for multi-week predictions and the real time configuration which are detailed in Hudson et al. (2017).

Hindcast runs

The Ekman and adjusted WWV 1-7 months hindcasts run between 1990 and 2013. Each monthly hindcast run consist of 11 ensembles (10 perturbed members and 1 unperturbed member), which are initialized at the 1^{st} and 25^{th} day of the month. Consequently, there are 22 ensemble members per hindcast run.

The Ekman WWV hindcasts are obtained by integrating the meridional Ekman transport anomalies over 120°E-80°W at 5°N and over 150°E-80°W at 5°S. Hereby, the meridional Ekman transport anomalies (V_{ek}) are obtained as following: $V_{ek} =$

$\frac{-\tau^x}{\rho f}$, with τ^x being the zonal wind stress anomalies as hindcasted by the ACCESS-S1 forecast system, ρ is the upper ocean density taken as constant (1023 kg/m^3) and f is the Coriolis parameter.

The adjusted WWV hindcasts are calculated as the difference of the total WWV hindcasts and the Ekman WWV hindcasts. The total WWV hindcasts are obtained by integrating the hindcasts of the anomalous depth of the 20°C isotherm over the WWV region.

References

Balmaseda, M. A., Mogensen, K. and Weaver, A. T. (2013), 'Evaluation of the ecmwf ocean reanalysis system oras4', *Quarterly Journal of the Royal Meteorological Society* **139**(674), 1132–1161.

Barnston, A. G., Tippett, M. K., L'Heureux, M. L., Li, S. and DeWitt, D. G. (2012), 'Skill of real-time seasonal enso model predictions during 2002–11: Is our capability increasing?', *Bulletin of the American Meteorological Society* **93**(5), 631–651.

Battisti, D. S. and Hirst, A. C. (1989), 'Interannual variability in a tropical atmosphere–ocean model: Influence of the basic state, ocean geometry and nonlinearity', *Journal of the atmospheric sciences* **46**(12), 1687–1712.

Bjerknes, J. (1969), 'Atmospheric teleconnections from the equatorial pacific', *Monthly weather review* **97**(3), 163–172.

Blockley, E., Martin, M., McLaren, A., Ryan, A., Waters, J., Lea, D., Mirouze, I., Peterson, K., Sellar, A. and Storkey, D. (2014), 'Recent development of the met office operational ocean forecasting system: an overview and assessment of the new global foam forecasts', *Geoscientific Model Development* **7**(6), 2613–2638.

Bosc, C. and Delcroix, T. (2008), 'Observed equatorial rossby waves and enso-related warm water volume changes in the equatorial pacific ocean', *Journal of Geophysical Research: Oceans* **113**(C6).

Boulanger, J.-P., Cravatte, S. and Menkes, C. (2003), 'Reflected and locally wind-forced interannual equatorial kelvin waves in the western pacific ocean', *Journal of Geophysical Research: Oceans* **108**(C10).

Bunge, L. and Clarke, A. J. (2014), 'On the warm water volume and its changing relationship with enso', *Journal of Physical Oceanography* **44**(5), 1372–1385.

Cai, W., Santoso, A., Wang, G., Yeh, S.-W., An, S.-I., Cobb, K. M., Collins, M., Guilyardi, E., Jin, F.-F., Kug, J.-S. et al. (2015), 'Enso and greenhouse warming', *Nature Climate Change* **5**(9), 849.

Cai, W., Wu, L., Lengaigne, M., Li, T., Mcgregor, S., Kug, J.-S., Yu, J.-Y., Stuecker, M. F., Santoso, A., Li, X. et al. (2019), 'Pantropical climate interactions', *Science* **363**(6430), eaav4236.

Cane, M. A. and Zebiak, S. E. (1985), 'A theory for el niño and the southern oscillation', *Science* **228**, 1084–1087.

Capotondi, A., Wittenberg, A. T., Newman, M., Di Lorenzo, E., Yu, J.-Y., Braconnot, P., Cole, J., Dewitte, B., Giese, B., Guilyardi, E. et al. (2015), 'Understanding enso diversity', *Bulletin of the American Meteorological Society* **96**(6), 921–938.

Carrillo, C. N. (1893), 'Hidrografía oceánica', *Bol. Soc. Geogr. Lima* **1**, 72–110.

Chelton, D. B. and Risien, C. M. (2016), 'Zonal and meridional discontinuities and other issues with the hadisst1. 1 dataset'.

Chiodi, A. M. and Harrison, D. (2017), 'Simulating enso sstas from tao/triton winds: the impacts of 20 years of buoy observations in the pacific waveguide and comparison with reanalysis products', *Journal of Climate* **30**(3), 1041–1059.

Chung, C. and Power, S. (2017), 'The non-linear impact of el niño, la niña and the southern oscillation on seasonal and regional australian precipitation', *Journal of Southern Hemisphere Earth Systems Science* **67**(1), 25–45.

Clarke, A. J. (2008), *An introduction to the dynamics of El Niño and the Southern Oscillation*, Elsevier.

Clarke, A. J., Van Gorder, S. and Colantuono, G. (2007), 'Wind stress curl and enso discharge/recharge in the equatorial pacific', *Journal of Physical Oceanography* **37**(4), 1077–1091.

Clarke, A. J. and Zhang, X. (2019), 'On the physics of the warm water volume and el niño/la niña predictability', *Journal of Physical Oceanography* **49**(6), 1541–1560.

Dee, D. P. and Uppala, S. (2009), 'Variational bias correction of satellite radiance data in the era-interim reanalysis', *Quarterly Journal of the Royal Meteorological Society: A journal of the atmospheric sciences, applied meteorology and physical oceanography* **135**(644), 1830–1841.

Dee, D. P., Uppala, S., Simmons, A., Berrisford, P., Poli, P., Kobayashi, S., Andrae, U., Balmaseda, M., Balsamo, G., Bauer, d. P. et al. (2011), 'The era-interim reanalysis: Configuration and performance of the data assimilation system', *Quarterly Journal of the royal meteorological society* **137**(656), 553–597.

Deser, C. and Wallace, J. M. (1990), 'Large-scale atmospheric circulation features of warm and cold episodes in the tropical pacific', *Journal of Climate* **3**(11), 1254–1281.

Diaz, H. F., Hoerling, M. P. and Eischeid, J. K. (2001), 'Enso variability, teleconnections and climate change', *International Journal of Climatology* **21**(15), 1845–1862.

DiNezio, P. N. and Deser, C. (2014), 'Nonlinear controls on the persistence of la niña', *Journal of Climate* **27**(19), 7335–7355.

DiNezio, P. N., Deser, C., Okumura, Y. and Karspeck, A. (2017), 'Predictability of 2-year la niña events in a coupled general circulation model', *Climate dynamics* **49**(11-12), 4237–4261.

Dommenget, D., Bayr, T. and Frauen, C. (2013), 'Analysis of the non-linearity in the pattern and time evolution of el niño southern oscillation', *Climate dynamics* **40**(11-12), 2825–2847.

Ebisuzaki, W. (1997), 'A method to estimate the statistical significance of a correlation when the data are serially correlated', *Journal of Climate* **10**(9), 2147–2153.

Fedorov, A. V., Hu, S., Lengaigne, M. and Guilyardi, E. (2015), 'The impact of westerly wind bursts and ocean initial state on the development, and diversity of el niño events', *Climate Dynamics* **44**(5-6), 1381–1401.

Frauen, C. and Dommenget, D. (2010), 'El niño and la niña amplitude asymmetry caused by atmospheric feedbacks', *Geophysical Research Letters* **37**(18).

Gasparin, F., Roemmich, D., Gilson, J. and Cornuelle, B. (2015), 'Assessment of the upper-ocean observing system in the equatorial pacific: The role of argo in resolving intraseasonal to interannual variability', *Journal of Atmospheric and Oceanic Technology* **32**(9), 1668–1688.

Gebbie, G. and Tziperman, E. (2009), 'Predictability of sst-modulated westerly wind bursts', *Journal of Climate* **22**(14), 3894–3909.

Giese, B. S. and Harrison, D. (1990), 'Aspects of the kelvin wave response to episodic wind forcing', *Journal of Geophysical Research: Oceans* **95**(C5), 7289–7312.

Gil, A. I., Louis, V. R., Rivera, I. N., Lipp, E., Huq, A., Lanata, C. F., Taylor, D. N., Russek-Cohen, E., Choopun, N., Sack, R. B. et al. (2004), 'Occurrence and distribution of vibrio cholerae in the coastal environment of peru', *Environmental microbiology* **6**(7), 699–706.

Gill, A. E. (1980), 'Some simple solutions for heat-induced tropical circulation', *Quarterly Journal of the Royal Meteorological Society* **106**(449), 447–462.

Glantz, M. (2002), *La Niña and its impacts: facts and speculation*, United Nations University (UNU).

Glantz, M. H., Glantz, M. H. et al. (2001), *Currents of change: impacts of El Niño and La Niña on climate and society*, Cambridge University Press.

Guan, C., McPhaden, M. J., Wang, F. and Hu, S. (2019), 'Quantifying the role of oceanic feedbacks on enso asymmetry', *Geophysical Research Letters* **46**(4), 2140–2148.

Halpert, M. S. and Ropelewski, C. F. (1992), 'Surface temperature patterns associated with the southern oscillation', *Journal of Climate* **5**(6), 577–593.

Harrison, D. and Chiodi, A. (2009), 'Pre-and post-1997/98 westerly wind events and equatorial pacific cold tongue warming', *Journal of Climate* **22**(3), 568–581.

Harrison, D. and Vecchi, G. A. (1997), 'Westerly wind events in the tropical pacific, 1986–95', *Journal of climate* **10**(12), 3131–3156.

Henley, B. J., Meehl, G., Power, S. B., Folland, C. K., King, A. D., Brown, J. N., Karoly, D. J., Delage, F., Gallant, A. J., Freund, M. et al. (2017), 'Spatial and temporal agreement in climate model simulations of the interdecadal pacific oscillation', *Environmental Research Letters* **12**(4), 044011.

Hoerling, M. P. and Kumar, A. (1997), 'Why do north american climate anomalies differ from one el niño event to another?', *Geophysical Research Letters* **24**(9), 1059–1062.

Horii, T., Ueki, I. and Hanawa, K. (2012), 'Breakdown of enso predictors in the 2000s: Decadal changes of recharge/discharge-sst phase relation and atmospheric intraseasonal forcing', *Geophysical Research Letters* **39**(10).

Hu, S. and Fedorov, A. V. (2016), 'Exceptionally strong easterly wind burst stalling el niño of 2014', *Proceedings of the National Academy of Sciences* **113**(8), 2005–2010.

Hu, Z.-Z., Kumar, A., Zhu, J., Huang, B., Tseng, Y.-h. and Wang, X. (2017), 'On the shortening of the lead time of ocean warm water volume to enso sst since 2000', *Scientific reports* **7**(1), 4294.

Huang, B., Angel, W., Boyer, T., Cheng, L., Chepurin, G., Freeman, E., Liu, C. and Zhang, H.-M. (2018), 'Evaluating sst analyses with independent ocean profile observations', *Journal of Climate* **31**(13), 5015–5030.

Hudson, D., Alves, O., Hendon, H. H., Lim, E.-P., Liu, G., Luo, J.-J., MacLachlan, C., Marshall, A. G., Shi, L., Wang, G. et al. (2017), 'Access-s1: the new bureau of meteorology multi-week to seasonal prediction system', *Journal of Southern Hemisphere Earth Systems Science* **67**(3), 132–159.

Izumo, T., Lengaigne, M., Vialard, J., Suresh, I. and Planton, Y. (2019), 'On the physical interpretation of the lead relation between warm water volume and the el niño southern oscillation', *Climate Dynamics* **52**(5-6), 2923–2942.

Jin, F.-F. (1997), 'An equatorial ocean recharge paradigm for enso. part i: Conceptual model', *Journal of the atmospheric sciences* **54**(7), 811–829.

Kalnay, E., Kanamitsu, M., Kistler, R., Collins, W., Deaven, D., Gandin, L., Iredell, M., Saha, S., White, G., Woollen, J. et al. (1996), 'The ncep/ncar 40-year reanalysis project', *Bulletin of the American meteorological Society* **77**(3), 437–472.

Kanamitsu, M., Ebisuzaki, W., Woollen, J., Yang, S.-K., Hnilo, J., Fiorino, M. and Potter, G. (2002), 'Ncep–doe amip-ii reanalysis (r-2)', *Bulletin of the American Meteorological Society* **83**(11), 1631–1644.

Kao, H.-Y. and Yu, J.-Y. (2009), 'Contrasting eastern-pacific and central-pacific types of enso', *Journal of Climate* **22**(3), 615–632.

Kessler, W. S. (1991), 'Can reflected extra-equatorial rossby waves drive enso?', *Journal of physical oceanography* **21**(3), 444–452.

Kessler, W. S. (2002), 'Is enso a cycle or a series of events?', *Geophysical Research Letters* **29**(23), 40–1.

Kobayashi, S., Ota, Y., Harada, Y., Ebita, A., Moriya, M., Onoda, H., Onogi, K., Kamahori, H., Kobayashi, C., Endo, H. et al. (2015), 'The jra-55 reanalysis: General specifications and basic characteristics', *Journal of the Meteorological Society of Japan. Ser. II* **93**(1), 5–48.

Kumar, A., Chen, M., Xue, Y. and Behringer, D. (2015), 'An analysis of the temporal evolution of enso prediction skill in the context of the equatorial pacific ocean observing system', *Monthly Weather Review* **143**(8), 3204–3213.

Lama, J. R., Seas, C. R., León-Barúa, R., Gotuzzo, E. and Sack, R. B. (2004), 'Environmental temperature, cholera, and acute diarrhoea in adults in lima, peru', *Journal of Health, Population and Nutrition* pp. 399–403.

Larkin, N. K. and Harrison, D. (2002), 'Enso warm (el niño) and cold (la niña) event life cycles: Ocean surface anomaly patterns, their symmetries, asymmetries, and implications', *Journal of Climate* **15**(10), 1118–1140.

Lengaigne, M., Boulanger, J.-P., Menkes, C., Madec, G., Delecluse, P., Guilyardi, E. and Slingo, J. (2003), 'The march 1997 westerly wind event and the onset of the 1997/98 el nino: Understanding the role of the atmospheric response', *Journal of climate* **16**(20), 3330–3343.

Levine, A. F. and McPhaden, M. J. (2016), 'How the july 2014 easterly wind burst gave the 2015–2016 el niño a head start', *Geophysical research letters* **43**(12), 6503–6510.

Loughran, T. F., Perkins-Kirkpatrick, S. E. and Alexander, L. V. (2017), 'Understanding the spatio-temporal influence of climate variability on australian heatwaves', *International Journal of Climatology* **37**(10), 3963–3975.

Luo, J.-J., Masson, S., Behera, S. K. and Yamagata, T. (2008), 'Extended enso predictions using a fully coupled ocean–atmosphere model', *Journal of Climate* **21**(1), 84–93.

MacLachlan, C., Arribas, A., Peterson, K., Maidens, A., Fereday, D., Scaife, A., Gordon, M., Vellinga, M., Williams, A., Comer, R. et al. (2015), 'Global seasonal forecast system version 5 (glosea5): a high-resolution seasonal forecast system', *Quarterly Journal of the Royal Meteorological Society* **141**(689), 1072–1084.

Mantua, N. J., Hare, S. R., Zhang, Y., Wallace, J. M. and Francis, R. C. (1997), 'A pacific interdecadal climate oscillation with impacts on salmon production', *Bulletin of the american Meteorological Society* **78**(6), 1069–1080.

McGregor, S., Gupta, A. S. and England, M. H. (2012a), 'Constraining wind stress products with sea surface height observations and implications for pacific ocean sea level trend attribution', *Journal of Climate* **25**(23), 8164–8176.

McGregor, S., Ramesh, N., Spence, P., England, M. H., McPhaden, M. J. and Santoso, A. (2013), 'Meridional movement of wind anomalies during enso events and their role in event termination', *Geophysical Research Letters* **40**(4), 749–754.

McGregor, S., Timmermann, A., Jin, F.-F. and Kessler, W. S. (2016), 'Charging el niño with off-equatorial westerly wind events', *Climate dynamics* **47**(3-4), 1111–1125.

McGregor, S., Timmermann, A., Schneider, N., Stuecker, M. F. and England, M. H. (2012b), 'The effect of the south pacific convergence zone on the termination of el niño events and the meridional asymmetry of enso', *Journal of Climate* **25**(16), 5566–5586.

McPhaden, M. (2015), 'Playing hide and seek with el niño', *Nature Climate Change* **5**(9), 791.

McPhaden, M. J. (2003), 'Tropical pacific ocean heat content variations and enso persistence barriers', *Geophysical research letters* **30**(9).

McPhaden, M. J. (2012), 'A 21st century shift in the relationship between enso sst and warm water volume anomalies', *Geophysical research letters* **39**(9).

McPhaden, M. J., Ando, K., Bourles, B., Freitag, H., Lumpkin, R., Masumoto, Y., Murty, V., Nobre, P., Ravichandran, M., Vialard, J. et al. (2010), 'The global tropical moored buoy array', *Proceedings of OceanObs* **9**, 668–682.

McPhaden, M. J. and Yu, X. (1999), 'Equatorial waves and the 1997–98 el niño', *Geophysical Research Letters* **26**(19), 2961–2964.

McPhaden, M. J., Zebiak, S. E. and Glantz, M. H. (2006), 'Enso as an integrating concept in earth science', *science* **314**(5806), 1740–1745.

McPhaden, M., Lee, T. and McClurg, D. (2011), 'El niño and its relationship to changing background conditions in the tropical pacific ocean', *Geophysical Research Letters* **38**(15).

Meinen, C. S. (2005), 'Meridional extent and interannual variability of the pacific ocean tropical–subtropical warm water exchange', *Journal of physical oceanography* **35**(3), 323–335.

Meinen, C. S. and McPhaden, M. J. (2000), 'Observations of warm water volume changes in the equatorial pacific and their relationship to el niño and la niña', *Journal of Climate* **13**(20), 3551–3559.

Meinen, C. S. and McPhaden, M. J. (2001), 'Interannual variability in warm water volume transports in the equatorial pacific during 1993–99', *Journal of physical oceanography* **31**(5), 1324–1345.

Neske, S. and McGregor, S. (2018), 'Understanding the warm water volume precursor of enso events and its interdecadal variation', *Geophysical Research Letters* **45**(3), 1577–1585.

Newman, M., Alexander, M. A., Ault, T. R., Cobb, K. M., Deser, C., Di Lorenzo, E., Mantua, N. J., Miller, A. J., Minobe, S., Nakamura, H. et al. (2016), 'The pacific decadal oscillation, revisited', *Journal of Climate* **29**(12), 4399–4427.

Okumura, Y. M. and Deser, C. (2010), 'Asymmetry in the duration of el niño and la niña', *Journal of Climate* **23**(21), 5826–5843.

Ordinola, N. (2002), 'The consequences of cold events for peru', *La Niña and its impacts: facts and speculation. United Nations University Press, New York* pp. 146–150.

Perry, S. J., McGregor, S., Gupta, A. S. and England, M. H. (2017), 'Future changes to el niño–southern oscillation temperature and precipitation teleconnections', *Geophysical Research Letters* **44**(20), 10–608.

Philander, S. G. and Fedorov, A. (2003), 'Is el niño sporadic or cyclic?', *Annual Review of Earth and Planetary Sciences* **31**(1), 579–594.

Picaut, J., Masia, F. and Du Penhoat, Y. (1997), 'An advective-reflective conceptual model for the oscillatory nature of the enso', *Science* **277**(5326), 663–666.

Planton, Y., Vialard, J., Guilyardi, E., Lengaigne, M. and Izumo, T. (2018), 'Western pacific oceanic heat content: a better predictor of la niña than of el niño', *Geophysical Research Letters* **45**(18), 9824–9833.

Power, S. B. and Delage, F. P. (2018), 'El niño–southern oscillation and associated climatic conditions around the world during the latter half of the twenty-first century', *Journal of Climate* **31**(15), 6189–6207.

Power, S., Casey, T., Folland, C., Colman, A. and Mehta, V. (1999), 'Inter-decadal modulation of the impact of enso on australia', *Climate Dynamics* **15**(5), 319–324.

Power, S., Delage, F., Chung, C., Kociuba, G. and Keay, K. (2013), 'Robust twenty-first-century projections of el niño and related precipitation variability', *Nature* **502**(7472), 541.

Power, S., Haylock, M., Colman, R. and Wang, X. (2006), 'The predictability of interdecadal changes in enso activity and enso teleconnections', *Journal of Climate* **19**(19), 4755–4771.

Rasmusson, E. M. and Carpenter, T. H. (1982), 'Variations in tropical sea surface temperature and surface wind fields associated with the southern oscillation/el niño', *Monthly Weather Review* **110**(5), 354–384.

Rebert, J.-P., Donguy, J.-R., Eldin, G. and Wyrtki, K. (1985), 'Relations between sea level, thermocline depth, heat content, and dynamic height in the tropical pacific ocean', *Journal of Geophysical Research: Oceans* **90**(C6), 11719–11725.

Santoso, A., Hendon, H., Watkins, A., Power, S., Dommenget, D., England, M. H., Frankcombe, L., Holbrook, N. J., Holmes, R., Hope, P. et al. (2019), 'Dynamics and predictability of el niño–southern oscillation: An australian perspective on progress and challenges', *Bulletin of the American Meteorological Society* **100**(3), 403–420.

Sarachik, E. S. and Cane, M. A. (2010), *The El Nino-southern oscillation phenomenon*, Cambridge University Press.

Singh, A. and Delcroix, T. (2013), 'Eastern and central pacific enso and their relationships to the recharge/discharge oscillator paradigm', *Deep Sea Research Part I: Oceanographic Research Papers* **82**, 32–43.

Smith, N. R. (1995), 'An improved system for tropical ocean subsurface temperature analyses', *Journal of Atmospheric and Oceanic Technology* **12**(4), 850–870.

Smith, T. M., Reynolds, R. W., Peterson, T. C. and Lawrimore, J. (2008), 'Improvements to noaa's historical merged land–ocean surface temperature analysis (1880–2006)', *Journal of Climate* **21**(10), 2283–2296.

Suarez, M. J. and Schopf, P. S. (1988), 'A delayed action oscillator for enso', *Journal of the atmospheric Sciences* **45**(21), 3283–3287.

Thompson, C. and Battisti, D. (2001), 'A linear stochastic dynamical model of enso. part ii: Analysis', *Journal of Climate* **14**(4), 445–466.

Timmermann, A., An, S.-I., Kug, J.-S., Jin, F.-F., Cai, W., Capotondi, A., Cobb, K. M., Lengaigne, M., McPhaden, M. J., Stuecker, M. F. et al. (2018), 'El niño–southern oscillation complexity', *Nature* **559**(7715), 535.

Tomczak, M. and Godfrey, J. S. (2013), *Regional oceanography: an introduction*, Elsevier.

Trenberth, K. E., Branstator, G. W., Karoly, D., Kumar, A., Lau, N.-C. and Ropelewski, C. (1998), 'Progress during toga in understanding and modeling global teleconnections associated with tropical sea surface temperatures', *Journal of Geophysical Research: Oceans* **103**(C7), 14291–14324.

Valcke, S. (2013), 'The oasis3 coupler: a european climate modelling community software', *Geoscientific Model Development* **6**(2), 373–388.

Vecchi, G. A. (2006), 'The termination of the 1997–98 el niño. part ii: Mechanisms of atmospheric change', *Journal of climate* **19**(12), 2647–2664.

Vecchi, G. A. and Harrison, D. (2000), 'Tropical pacific sea surface temperature anomalies, el niño, and equatorial westerly wind events', *Journal of climate* **13**(11), 1814–1830.

Vicente-Serrano, S. M., López-Moreno, J. I., Gimeno, L., Nieto, R., Morán-Tejeda, E., Lorenzo-Lacruz, J., Beguería, S. and Azorin-Molina, C. (2011), 'A multiscalar global evaluation of the impact of enso on droughts', *Journal of Geophysical Research: Atmospheres* **116**(D20).

Walker, G. T. (1924), 'Correlations in seasonal variations of weather. i. a further study of world weather', *Mem. Indian Meteorol. Dep.* **24**, 275–332.

Wang, C. (2001), 'A unified oscillator model for the el niño–southern oscillation', *Journal of Climate* **14**(1), 98–115.

Wang, C. and Picaut, J. (2004), 'Understanding enso physics—a review', *Earth's Climate: The Ocean–Atmosphere Interaction, Geophys. Monogr* **147**, 21–48.

Wang, C., Weisberg, R. H. and Virmani, J. I. (1999), 'Western pacific interannual variability associated with the el niño-southern oscillation', *Journal of Geophysical Research: Oceans* **104**(C3), 5131–5149.

Wang, G. and Hendon, H. H. (2007), 'Sensitivity of australian rainfall to inter–el niño variations', *Journal of climate* **20**(16), 4211–4226.

Wang, W., Chen, M. and Kumar, A. (2010), 'An assessment of the cfs real-time seasonal forecasts', *Weather and forecasting* **25**(3), 950–969.

Weisberg, R. H. and Wang, C. (1997), 'A western pacific oscillator paradigm for the el niño-southern oscillation', *Geophysical research letters* **24**(7), 779–782.

Werner, A. and Holbrook, N. J. (2011), 'A bayesian forecast model of australian region tropical cyclone formation', *Journal of Climate* **24**(23), 6114–6131.

Williams, A. A. J. and Karoly, D. J. (1999), 'Extreme fire weather in australia and the impact of the el niño-southern oscillation', *Aust. Meteor. Mag.* **48**, 15–22.

Williams, K., Harris, C., Bodas-Salcedo, A., Camp, J., Comer, R., Copsey, D., Fereday, D., Graham, T., Hill, R., Hinton, T. et al. (2015), 'The met office global coupled model 2.0 (gc2) configuration', *Geoscientific Model Development* **8**(5), 1509–1524.

Wu, X., Okumura, Y. M. and DiNezio, P. N. (2019), 'What controls the duration of el niño and la niña events?', *Journal of Climate* **32**(18), 5941–5965.

Wyrtki, K. (1975), 'El niño—the dynamic response of the equatorial pacific ocean to atmospheric forcing', *Journal of Physical Oceanography* **5**(4), 572–584.

Wyrtki, K. (1985), 'Water displacements in the pacific and the genesis of el niño cycles', *Journal of Geophysical Research: Oceans* **90**(C4), 7129–7132.

Xavier, P. K., Marzin, C. and Goswami, B. N. (2007), 'An objective definition of the indian summer monsoon season and a new perspective on the enso–monsoon relationship', *Quarterly Journal of the Royal Meteorological Society: A journal of the atmospheric sciences, applied meteorology and physical oceanography* **133**(624), 749–764.

Xie, S. P., Hu, K., Hafner, J., Tokinaga, H., Du, Y., Huang, G. and Sampe, T. (2009), 'Indian ocean capacitor effect on indo–western pacific climate during the summer following el niño', *Journal of Climate* **22**(3), 730–747.

Yu, L., Weller, R. A. and Liu, W. T. (2003), 'Case analysis of a role of enso in regulating the generation of westerly wind bursts in the western equatorial pacific', *Journal of Geophysical Research: Oceans* **108**(C4).

Zavala-Garay, J., Moore, A. M. and Kleeman, R. (2004), 'Influence of stochastic forcing on enso prediction', *Journal of Geophysical Research: Oceans* **109**(C11).

Zeller, M., McGregor, S. and Spence, P. (2019), 'Hemispheric asymmetry of the pacific shallow meridional overturning circulation', *Journal of Geophysical Research: Oceans* **124**(8), 5765–5786.

Zhang, W., Li, S., Jin, F.-F., Xie, R., Liu, C., Stuecker, M. F. and Xue, A. (2019), 'Enso regime changes responsible for decadal phase relationship variations between enso sea surface temperature and warm water volume', *Geophysical Research Letters* .

Zhao, M., Hendon, H. H., Alves, O., Liu, G. and Wang, G. (2016), 'Weakened eastern pacific el niño predictability in the early twenty-first century', *Journal of Climate* **29**(18), 6805–6822.